Sunniva Skogheim

Low-Temperature Oxidation of Methane (CH$_4$) and Carbon Monoxide (CO) over Pd/Al$_2$O$_3$ and Pd-Ag/Al$_2$O$_3$ Catalysts

Master's thesis

NTNU
Norwegian University of
Science and Technology

Sunniva Skogheim

Low-Temperature Oxidation of Methane (CH$_4$) and Carbon Monoxide (CO) over Pd/Al$_2$O$_3$ and Pd-Ag/Al$_2$O$_3$ Catalysts

Master's thesis in Chemical Engineering and Biotechnology
Supervisor: Hilde Johnsen Venvik
Co-supervisor: Rune Lødeng
June 2021

Norwegian University of Science and Technology
Faculty of Natural Sciences
Department of Chemical Engineering

NTNU
Norwegian University of
Science and Technology

Preface

This master´s thesis is written for the Catalysis group at the Department of Chemical Engineering, NTNU, as a finalization of the master´s degree program in Chemical Engineering and Biotechnology.

First of all, I would like to thank my supervisor, Professor Hilde Johnsen Venvik, for excellent guidance and contribution of ideas during the whole research. I would also like to thank my co-supervisor, Senior Scientist at SINTEF, Rune Lødeng for his contribution. Moreover, I want to express my sincere gratitude and appreciation to Ph.D candidate Junbo Yu for training and guidance in how to handle and work in the reaction rig, and also for interpretation of experimental results. In addition, a big thank-you to Senior Engineer, Estelle Vanhaecke and Staff Engineer, Karin W. Dragsten for outstanding guidance and help whenever needed.

Finally, I want to thank all my friends and family for keeping me motivated. Especially I would like to thank Kristin Madsen and Sunniva Vold for a memorable and enjoyable ending of five years in Trondheim.

Declaration of Compliance

I, Sunniva Skogheim, declare that this is an independent work according to the exam regulations of the Norwegian University of Science and Technology (NTNU).

Trondheim, Norway 14.06.21

Sunniva Skogheim

Abstract

Catalytic oxidation of CH_4 and CO are promising solutions to meet the future demands of pollution abatement. The utilization of catalytic systems offers the opportunity to convert pollutants such as CO and NO_x, and possibilities for using more environmentally friendly benign fuels such as natural gas. There are, however, two main problems associated with the reaction conditions: 1) conversion of CO, an important step in automotive exhaust catalysis, is partially suppressed during the cold start period of the engine and 2) excess methane in the exhaust gas as a consequence of NO_x suppression requirements. Complete catalytic oxidation of CH_4 and CO into CO_2 and H_2O is one way of avoiding this. Palladium, within the PGM group, has shown specific activity towards these reactions but because of its price and availability, there is a need for further research of alternative materials.

This master´s thesis aims to investigate the influence of replacing 25% of Pd in Pd/Al_2O_3 with a cheaper element, Ag. The catalytic performance was tested in two reactions, CH_4 and CO oxidation. CH_4 oxidation was investigated for hysteresis effects, the influence of silver, the influence of water, and long-term stability. For CO oxidation, the activity dependence of CO concentration and maximum temperature were investigated with the aspect of examining the effect these parameters have on the hysteresis behavior. Both catalysts were synthesized with the incipient wetness impregnation method, whereby a co-impregnation was used for the bimetallic catalyst. The catalysts were characterized with XRF, XRD, N_2 physisorption, TEM, chemisorption, and TPR.

Both catalysts displayed catalytic activity at low temperatures in the reactions. It was found that the replacement of 25% palladium did not seem to affect the catalytic activity dramatically. For CH_4 oxidation, the catalysts displayed similar features with addition of water although the catalytic performance was significantly affected. However, based on realistic exhaust gas conditions, Pd/Al_2O_3 and $Pd\text{-}Ag/Al_2O_3$ exhibited sufficient catalytic activity. $Pd\text{-}Ag/Al_2O_3$ was found to deactivate after time on stream, suggesting a change in the catalyst surface.

Considering hysteresis behavior, normal, reversed and no hysteresis were all observed. For CH_4 oxidation, the hysteresis was of reversed nature, with lower conversions during extinction. Normal and no hysteresis was observed for CO oxidation over the catalysts and were found to be dependent on the inlet concentration of CO. In conclusion, $Pd\text{-}Ag/Al_2O_3$ is a promising candidate for low-temperature oxidation of CH_4 and CO. The replacement of 25% Pd with Ag yield appealing results with respect to catalytic performance.

Sammendrag

Oksidasjon av metan- og karbonmonoksid ved lave temperaturer blir sett på som lovende løsninger for å kunne møte fremtidens krav om utslippsredusering. Katalytiske systemer gjør det mulig, for eksempel, å omdanne forurensninger som karbonmonoksid (viktig steg i bilers eksosanlegg) og NO_x. I tillegg åpner det muligheter for å bruke mer miljøvennlige drivstoff, som naturgass. Det er derimot to vesentlige problemer knyttet til reaksjonsbetingelsene: 1) fare for utslipp av karbonmonoksid under kaldsstartsperioden og 2) "lean" forbrenning kan føre til metanlekkasje i eksosgassen. Fullstendig katalytisk forbrenning av metan og karbonmonoksid er en måte å unngå dette på og dermed er interessen stor for katalysatorer som fungerer effektivt under de gitte reaksjonsbetingelsene.

I denne masteroppgaven har effekten av å erstatte 25% av palladium i Pd/Al_2O_3 med sølv blitt undersøkt i katalytisk oksidasjon av metan- og karbonmonoksid. For metanoksidasjon, ble den katalytiske aktiviteten undersøkt for hysterese effekter, effekt av sølv, effekt av vann og langtids stabilitet. For katalytisk oksidasjon av karbonmonoksid, ble avhengigheten av fødekonsentrasjonen av karbonmonoksid og maksimal temperatur undersøkt med mål om å finne ut hvordan disse parameterne påvirker hysteresens oppførsel. Begge katalysatorene ble syntetisert med fuktimpregnering hvorav en samimpregnering ble brukt for den bimetalliske katalysatoren. Katalysatorene ble karakterisert med XRF, XRD, N_2 physisorption, TEM, kjemisorpsjon og TPR.

Generelt sett ble det funnet at begge katalysatorene viste høy aktivitet ved lave temperaturer i begge reaksjoner. Erstatningen av 25% palladium hadde ingen dramatisk effekt på den katalytiske aktiviteten. For oksidasjon av metan, viste det seg at tilførselen av vann til føden medførte seg en stor effekt på den katalytiske aktiviteten, men forskjellene mellom katalysatorene, var ikke store. Basert på realistiske eksosgass betingelser, var den katalytiske ytelsen god for begge katalysatorene. Videre ble det foreslått en forandring i sammensetning av katalysatorens overflate for Pd-Ag/Al_2O_3 under et langtidseksperiment.

Normal, reversert og ingen hysterese ble alle observert i de kinetiske undersøkelsene. For metanoksidasjon var hysteresen av reversert natur, det vil si med lavere omdannelse under nedkjølingsprosess. Normal og ingen hysterese ble observert for CO oksidasjon og ble funnet til å være betydelig avhengig av fødekonsentrasjon av karbonmonoksid. Pd-Ag/Al_2O_3 synes å være en lovende kandidat for oksidasjon av metan og karbonmonoksid ved lave temperaturer, og erstatningen av 25% av palladium demonstrerte optimistiske resultater i lys av katalytisk prestasjon.

Contents

Abbreviations

Abbreviation	Definition
ADF	Annular dark field
BET	Brunaer, Emmett and Teller
BJH	Barret-Joyner-Halenda
BF	Bright field
DF	Dark field
ECD	Electron capture Detector
EDS	Energy-dispersive X-ray spectroscopy
EELS	Electron energy loss spectroscopy
ER	Eley-Rideal
FFm	Float flow meter
FID	Flame ionization detector
GC	Gas chromatopraphy
GHSV	Gas hourly space velocity
GWP	Global warming potential
HAADF	High angle annular dark field
HFO	Heavy fuel oil
IWI	Incipient wetness impregnation
LFC	Liquid flow controller
LH	Langmuir Hinselwood
MFC	Mass flow controller
MS	Mass spectroscopy
MvK	Mars van Krevelen
NAP-XPS	Near ambient pressure XPS
NG	Natural gas
NGV	Natural gas vehicles
NTNU	Norwegian University of Science and Technology
PGM	Platinum group metal
SEM	Scanning electron microscopy
STEM	Scanning transmission electron microscopy
T_{ex}	Temperature at 50% conversion (heating curve)
T_{ig}	Temperature at 50% conversion (cooling curve)
T_{10}	Temperature at 10% conversion
T_{50}	Temperature at 50% conversion
T_{100}	Temperature at 100% conversion
TCD	Thermal conductivity detector
TEM	Transmission electron microscopy
TOF	Turnover frequency
TPR	Temperature-programmed reduction
WCOT	Wall of an open tube
WDXRF	Wavelength Dispersive XRF

XPS	X-ray photoelectron spectroscopy
XRD	X-ray Diffraction
XRF	X-ray Fluorescence
Ag	Silver
Ar	Argon
Al_2O_3	Aluminium oxide
CH_4	Methane
CO	Carbon monoxide
CO_2	Carbon dioxide
H_2	Hydrogen
H_3BO_3	Boric acid
N_2	Nitrogen
NOx	Nitrogen oxide
O_2	Oxygen
Pd	Palladium
PdO	Palladium oxide
Pt	Platinum
Rh	Rhodium
SiC	Silicon carbide
SOx	Sulphur oxide

List of Symbols

α	Constant, $\frac{\chi-1}{V_0\chi}$	mm^{-3}
β	Peak width	Å
χ	Ratio of desorption	-
ΔH	Heat of reaction	$kJ\,mol^{-1}$
η	Constant, $\frac{1}{\chi V_0}$	mm^{-3}
λ	X-ray wavelength	nm
ρ	Density	gcm^{-3}
σ	Surface tension	$N\,m^{-1}$
τ	Residence time	s
θ	Angle of diffraction	°
θ	Contact angle, Kelvin Equation	°
A	Specific metal surface area	m^2
A_0	Area occupied by one N_2-molecule	nm^2
A_T	Total surface area	nm^2
a_m	Atomic cross sectional area	nm^2
C_A	Concentration of component A	$mol\,L^{-1}$
C_{A0}	Initial concentration of component A	$mol\,L^{-1}$
D	Dispersion	%
d	Distance of lattice planes	Å
d_{va}	Mean particle size	nm
E_A	Activation energy	$kJ\,mol^{-1}$
E_C	Carbon balance	%
F_A	Flow of component A	$ml\,min^{-1}$
F_{tot}	Total flow	$ml\,min^{-1}$
GHSV	Gas hourly space velocity	$NmL\,h^{-1}\,g_{cat}$
K	Sherrer´s constant	-
k	Rate constant	s^{-1}
k_A	Response factor of component A	-
k_B	Boltzmann constant	$J\,K^{-1}$
Mm	Molar mass	$g\,mol^{-1}$
N	Number of molecules adsorbed	-
N_A	Avogadro number	mol^{-1}
N_S	Number of surface atoms	-
N_T	Total number of atoms	-
n	Order of reflection	-
P	Pressure	bar
P_0	Saturation pressure	bar
r	Reaction rate	$mol\,h^{-1}g_{cat}^{-1}$
r_p	Radius of pore	nm
S_A	Peak area of component A	nm^2

S_{BET}	Surface area	m^2g^{-1}
T	Temperature	K
T_c	Critical temperature	K
V	Volume	cm^3
V_0	Volume adsorbed in the first monolayer	mm^3
V_a	Total volume of adsorbed molecules	mm^3
V_M	Volume of chemisorbed gas	cm^3 g^{-1}(STP)
V_{molar}	Volume of ideal gas	cm^3(STP) mol^{-1}
V_{PT}	Pore volume of support	cm^3
V_R	Reactor volume	cm^3
ν	Pre-exponential factor	-
v_p	Pore volume	cm^3g^{-1}
X	Conversion	%
y_A	Mole fraction of component A in gas phase	%

List of Figures

List of Tables

Chapter 1

Introduction

1.1 Motivation

Low-temperature oxidation of methane (CH_4) and carbon monoxide (CO) are fundamental reactions in industry and for pollution abatement [1]. Stricter environmental regulations are introduced in all industries and must be faced by both stationary and mobile pollution sources [2]. Thus, the demand for research and development of greener solutions is constantly increasing. By using catalytic systems, pollutants such as carbon monoxide (CO) and nitric oxides (NOx) can be converted into non-pollutants. For example, CO oxidation is an important step in automotive exhaust catalysis. Additionally, the utilization of catalytic systems opens up opportunities for more environmentally friendly benign fuels, such as natural gas (NG). Methane, which dominates NG by 85-95%, is a clean and attractive fuel, but the advantages are partially outbalanced by methane slip in the exhaust gas [3]. By complete catalytic oxidation, both CH_4 and CO present in the exhaust gas can be efficiently converted into water and carbon dioxide.

Pd facilitates the oxidation of CH_4 and CO in automotive catalysis and displays high activity in low temperature conversion of these substances [2, 4, 5]. However, Pd is pricey and the worldwide resources are insufficient. Also, catalyst stability and sensitivity against poisoning are much scrutinized, being two main problems in the application of Pd catalyst in emission abatement technologies [4, 5]. One possible way to alter the catalyst properties is to alloy with a second metal in catalysts (bimetallic catalyst) [6]. By replacing a part of the Pd with another metal and still retain the overall properties, the effects of alloying can be either promoting concerning catalyst activity, stability and selectivity or cost-reducing if replaced with a cheaper element, for example, Ag.

Among bimetallic catalysts, research are mainly found for Pt-Pd cat-

alysts, where several studies have reported increased catalyst activity with the addition of Pt to Pd catalysts [6]. For example, Skoglundh *et al.* (1991, [7]) reported that relatively small amounts of Pt added promoted the complete oxidation of CO. Persson *et al.* (2005) [6] studied the influence of co-metals on bimetallic palladium catalysts for methane combustion. They reported high stability for the Pd-Ag catalyst, though it was slightly less active when compared with Pt-Pd. Although little research is found on Pd-Ag catalysts for low-temperature oxidation, it is an interesting alloying element because of its complex roles in oxidation reactions [8].

1.2   Objective

The objective of this research is to investigate the low-temperature catalytic oxidation of methane and carbon monoxide over Pd-based catalysts. The aim is to compare a monometallic catalyst, Pd/Al_2O_3 with a bimetallic catalyst, $Pd-Ag/Al_2O_3$ and to see how a replacement by 25% of Pd with a cheaper element, Ag, affect the catalytic performance in these reactions. The materials will be characterized with techniques such as XRF, XRD, N_2 physisorption, TEM, Chemisorption, and TPR. Further, the catalyst performance will be investigated in an adapted test rig for CH_4- and CO oxidation. The catalytic activity in methane oxidation will be investigated for hysteresis effects, the influence of silver, the presence of water, and long-term stability. For CO oxidation, the dependency of inlet CO concentration and maximum temperature on catalyst activity will be examined. The aim is to compare with already reported NAP-XPS data of Pd and Pd-Ag single crystal.

1.3   Method

This master´s thesis is a continuance of a specialization project completed in autumn of 2020 but with new research material and an additional reaction [9]. In total, four master´s thesis has focused on low-temperature oxidation of methane: two focusing on noble metals and two on metal oxide catalysts [10, 11, 12, 13]. The investigation of CO oxidation is, however, a new contribution to the research project. It was, thus, of interest to compare the results with those reported by Fernandes *et al.* (2016, [14]) and Strømsheim *et al.* (2021, [5]) who studied CO oxidation over Pd and Pd-Ag single crystal.

With the guidance of master supervisors, the scientific methods of the research were determined. The practical work was conducted independently, apart from TEM which was executed by Research Scientist Per Erik Vullum at SINTEF Industry, but with the author of this thesis

present throughout the analysis. Instrument training was provided by staff engineers working in the catalysis group.

The theoretical background of the thesis was established by literature searching. Mostly, this was conducted by exploring relevant scientific databases as well as earlier thesis produced on this research project. Literature of bimetallic Pd-Ag/Al_2O_3 in low-temperature oxidation reactions was, however, found to be limited.

Chapter 2

Theory

2.1 Catalytic Oxidation

The catalytic oxidation of methane (CH_4) and carbon monoxide (CO) are both important reactions in pollution control for industrial processes and automotives [1, 3]. By complete oxidation over catalysts, CH_4 and CO present in the exhaust gas from the engine can be converted into H_2O and CO_2.

2.1.1 Catalytic Oxidation of Methane (CH_4)

The research and development of more environmentally friendly benign fuels are increasing and natural gas (NG) as a fuel source has aroused interest in industrial countries all over the world [3]. NG is abundant available and the main component of NG is methane (85% - 95 %, [3]). Methane is the cleanest burning hydrocarbon and composed of a short hydrocarbon chain, resulting in a high H:C ratio and consequently lower CO_2-emissions. In addition, NG engines can operate under lean-burn conditions, making it possible to increase fuel efficiency in relation to stoichiometric conditions. Under such conditions the NO_x emissions are much reduced as the formation of thermal NO_x is favored at high temperatures (T > 1300 °C).

The advantages of using NG are to some extent balanced out by unconverted methane in the exhaust gas [3]. Methane is a potential greenhouse gas with global warming potential (GWP) 25 times larger than CO_2 over a time horizon of 100 years [15]. Therefore, the abatement of unconverted methane in the exhaust gas is crucial in the case of worldwide utilization of NG [16]. One way to facilitate the complete oxidation of methane is by catalytic after-treatment of the exhaust gas. The reaction of the complete oxidation of methane is illustrated in Equation (1) [17].

$$\text{CH}_4 + 2\text{O}_2 \xrightarrow{catalyst} \text{CO}_2 + 2\text{H}_2\text{O} \quad \Delta H = -803 kJ/mol \qquad (1)$$
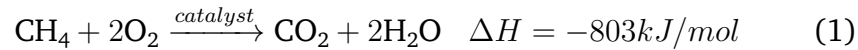
There are, however, challenges related to the reaction conditions. The catalyst must [3]:

- operate at low temperatures, i.e. < 500-550 °C.

- operate at low CH_4 concentrations (500-1000 ppm).

- have a tolerance to large amount of water vapour(10-15%), CO_2 (15%) and excess O_2.

- have a tolerance to low levels of SO_x(1 ppm)

- have a tolerance to NO_x. This is, however, dependent on under which conditions the engine can operate.

Under such lean-burn conditions, the thermal stability of the catalyst is out of concern [3], and the target properties of the catalyst are thus high activity at low temperatures and high resistance towards poisons in the exhaust gas. Both noble metals and transition metal oxides have been studied for catalytic combustion, whereby the first group has displayed superior activity.

2.1.2   Catalytic Oxidation of Carbon Monoxide (CO)

Carbon monoxide (CO) is a poisonous gas and in general, produced from incomplete oxidation of carbon-containing compounds [18]. CO is very hard to discover because of its non-existing taste, color, and odor, and it is therefore highly necessary to hinder or/and remove potential emissions of it [19]. The demand for catalytic CO oxidation is primarily largest in the industry and the transportation sector, being some of the largest contributors of CO emissions. Catalytic oxidation of CO (Equation (2)) is an important reaction and used in a wide range of applications. Especially it is known as a principal step in automotive exhaust catalysis [20]. The widely used three-way converter works ideally in a temperature region of 350 °C-650 °C. Consequently, the high operation temperatures suppress the conversion of CO during the cold start period leading to CO emissions. Thus, the development of catalysts working at low temperatures is of large interest.

$$\text{CO} + \frac{1}{2}\text{O}_2 \xrightarrow{catalyst} \text{CO}_2 \qquad (2)$$
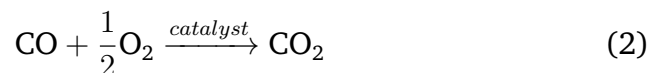
CO oxidation is also a widely studied reaction in fundamental studies. As an important model reaction, one can discover important adsorption/desorption and reaction mechanisms of catalysts, as well as catalyst structure [21]. In addition, it is an important probe reaction

for other oxidation reactions [19]. CO oxidation is in principal catalyzed by transition metals, whereby Pd, Pt, and Rh are extensively studied for this reaction [20, 19]. This will be further discussed in the upcoming section.

2.1.3 Catalysts for Methane and CO Oxidation

When designing catalytic materials for low temperature oxidation, the main objective is high activity at low temperatures and poison resistance [3].

Methane, which is a saturated hydrocarbon, is difficult to activate and normally requires high temperatures for complete oxidation [1]. The rate-determining step is assumed to be the activation of the primary C-H bond of the methane molecule [22]. In general, the platinum group metal (PGM) are extensively studied catalysts for complete oxidation of methane [3]. Within this group, Pd and Pt are the most studied and used, essentially because of their specific activity towards this reaction. When supported on a material with a high specific surface area, such as alumina (Al_2O_3) they can obtain a high degree of dispersion and thus higher catalytic activity. In an oxygen rich environment (O_2:CH_4 molar ratio > 2), Pd display higher activity than Pt [23, 24, 16]. Since both the metal, Pd, and the metal oxide, PdO are reported as active oxidation catalysts, the active state of Pd is much debated. Moreover, PdO is by now, identified as the most active phase of palladium [24].

However, some major drawbacks are related to sulphur poisoning [16], CO_2 poisoning [25], and water inhibition [26] in methane oxidation over palladium based catalysts. It is well known that Pd is poisoned by sulphur compounds. Sulphur compounds present in the reactant gas strongly adsorbs to the surface of the PdO and causes a loss of active sites. As NGV engine exhaust contain large amounts of water vapour (10-15%) and CO_2 (15%), the inhibitory effect of water and CO_2 is also extensively studied [27, 25, 26]. Van Giezen *et al.* (1999, [27]) reported a strong inhibition by water, but no significant influence by CO_2 on the reaction rate. Based on this, only the influence of water will be investigated in this work.

CO oxidation is also catalyzed by noble metals such as Pt and Pd [20]. Moreover, the key issue is that at low temperatures, the adsorption of CO on these metals is strong, causing CO inhibition and no active sites for adsorption of O_2 [21]. Thus, the activation takes place at higher temperatures (normally over 100°C, [21]). This results in potential CO emissions before this temperature is reached. After reaching higher temperatures, O_2 can adsorb onto the active sites, and the reaction rate increases.

The addition of a second metal to a catalyst, forming bimetallic catalysts, has appeared as an interesting solution towards improving the catalyst stability [6, 16]. For methane oxidation, most literature is found on bimetallic systems comprised of Pd-Pt. Compared with monometallic palladium catalysts, improved performance have been reported for Pt-Pd catalysts [28, 29, 30, 6]. However, Pd and Pt are expensive and scarce which lowers the interest for commercial application. In addition, it is a debated question whether the activity is higher or not for the bimetallic catalyst compared with the monometallic. Another interesting feature, is if a part of Pd could be replaced with a cheaper element, such as Ag, and still maintain the overall properties [5]. Persson *et al.* (2005,[6]) reported Pd-Ag as a promising candidate for methane oxidation, and beneficial effects have been reported for other applications as well [31, 32, 33, 34]. Little research is though found for Ag as a candidate for low temperature oxidation, but its complex role in oxidation catalysis is a motivating factor for further investigation [8, 5].

2.1.4 Phenomenon of Hysteresis

Hysteresis is an interesting and important phenomenon within heterogeneous catalysis [19]. Al Soubaihi *et al.* (2018, [19]), define a hysteresis as "the dependence of the state of a system on its history". The hysteresis provides useful information about catalytic activity and hysteresis effects have been reported for both methane and CO oxidation [35, 14, 19, 5].

There are several types of hysteresis but when testing a catalyst in a reaction, the temperature hysteresis is most often observed. The temperature hysteresis is a result of a mismatch between the heating and cooling curve of a complete cycle, forming a hysteresis loop [19]. In other terms, this means that, for example, the degree of conversion or reaction rate is different for the ignition and extinction processes in the cycle. A distinction is normally made between the normal hysteresis and the reversed hysteresis. As illustrated in Figure 2.1, the normal hysteresis exhibit higher conversions during the extinction. The opposite features are thus observed for the reversed hysteresis with lower conversion during the extinction.
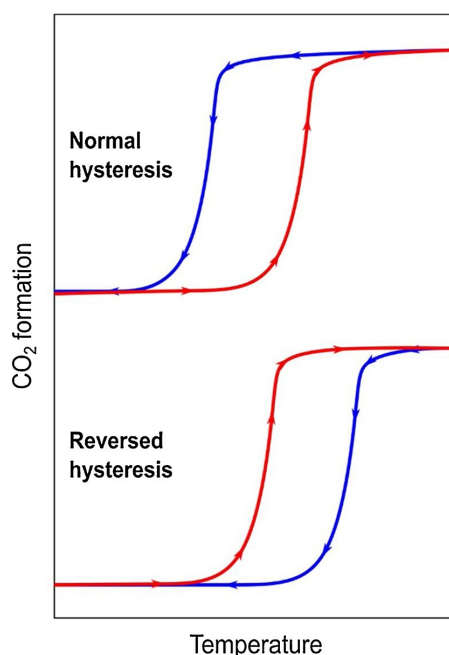
Figure 2.1: Illustration of normal hysteresis and reversed hysteresis. The figure is obtained from [5].

Several parameters affect the hysteresis behavior. For instance, temperature, particle size, inlet composition and concentration of reactants [19]. In most studies, the behavior of methane oxidation over palladium-based catalysts is reported to a reversed hysteresis with lower conversion during extinction. Carlsson and Skoglundh (2011, [1]) reported extinction at higher temperatures than ignition, i.e. reversed hysteresis for methane oxidation over a platinum-based catalyst. They attributed this to the reduction and oxidation of Pt sites, where the surface most likely was partially reduced by methane dissociation products during the extinction. For CO oxidation over the same catalyst, they reported a normal hysteresis caused by a more complete reduction of the Pt surface, which is more active for methane oxidation. Other authors, attribute lower activity during cooling curve to blocking of active sites by water and hydroxyl species as a consequence of water produced by the reaction (Equation (1)) or water present in the reactant mixture [36, 37].

A normal hysteresis is in most studies reported for CO oxidation [1, 14, 5]. The activity of CO oxidation is normally divided into three regions with low, high, and bi-stable activity respectively [19]. In the low-temperature region, the surface is, to a large extent, covered by CO, causing low activity. As the temperature rises, CO desorbs and oxygen adsorb onto the surface and a region with higher activity is reached. Finally, there is a region of bi-stability before the reaction lights off. Higher activity during the extinction is attributed to several

factors. Carlsson and Skoglundh (2011, [1]) presented the normal hysteresis as a consequence of three factors: inherent kinetic bistability, the interplay between reaction kinetics and diffusion phenomena, and heat generated by the exothermic reaction.

The reversed hysteresis is also observed for gas mixtures [19] and for unsupported Pd-Ag alloys [14, 5]. In the latter case, it has been reported that bimetallic catalyst has an important role where several parameters such as maximum temperature, initial conditions and, heating rate affect the formation of CO_2. Thus, it is clear that the nature of the hysteresis is highly dependent on the catalyst and the reaction conditions. It is therefore of large interest too to see how the hysteresis will be affected when applying different conditions in CH_4 and CO oxidation over Pd/Al_2O_3 and $Pd\text{-}Ag/Al_2O_3$ catalysts.

2.2   Catalyst Synthesis

2.2.1   Incipient Wetness Impregnation

Incipient Wetness Impregnation (IWI) is a commonly used method in the synthesis of heterogeneous catalysts. The method is based on dissolving salts containing the catalytic active element in water, also termed precursor solutions [20]. The support with pore volume,V_{PT}, is impregnated with a volume V = V_{PT} of the precursor solution [38]. The volume of the precursor is empirically determined and should be exactly enough to fill the pores and wet the outside of the particles of the support [39]. With a correctly performed impregnation, there will be no excess solution outside the pore space [40].

After impregnation, the material is dried to ensure that any solvent is removed [40]. Normally, this is done by heating the material to the boiling temperature of the solvent. Then, the precursor concentration will increase until saturation, resulting in crystallization. The final step of the catalyst synthesis is calcination where the catalyst precursor is exposed for further heat treatment [38]. This is where the salt is converted to a metal or metal oxide.

The preparation of a supported bimetallic catalyst by the incipient wetness impregnation can be done either by a co-impregnation or a sequential impregnation of the metals [41]. The co-impregnation is a single-step procedure where a solution of the precursors containing the metals is made [39]. A typically used solvent used for this is deionized water. Further, the support is impregnated with a volume that is equal to the total pore volume of the support [41]. Thus, the precursors will be deposited on the surface of the support simultaneously. Sequential impregnation involves separate deposition of the two elements, normally with drying or/and calcination in-between.

2.3   Catalyst Characterization

The principle of the characterization techniques used in this thesis
will in the following section be presented. This section is partially re-
produced but reformulated from the specialization project conducted
in autumn of 2020 under the same topic [9].

2.3.1   X-ray Fluorescence

X-ray Fluorescence (XRF) is an analytical technique giving both quan-
titative and qualitative analysis of materials [42]. This technique is
based on irradiation of a sample to produce ionization, where charac-
teristic fluorescent X-rays are generated by the elements present in the
sample [43]. When incident photons has larger energy than the bind-
ing energy of the electron in the inner orbital, the electron is ejected
and the atom is ionized [42]. As illustrated by Figure 2.2 the atom
is now in an unstable state. Returning to its initial state can happen
by two competitive effects, either by emitting an electron from the
atom orbital (the Auger effect) or filling the vacancy by transferring
an electron from the outer orbital. As a result of the energy differ-
ence between the initial and final state, an X-ray photon releases. The
probability of X-ray characteristic emission occurring is described by
a relative effectiveness between the effects within an atom. This ef-
fectiveness is called fluorescence yield which is determined by the
atomic number of the elements [42]. For instance, the sensitivity for
light elements is low.
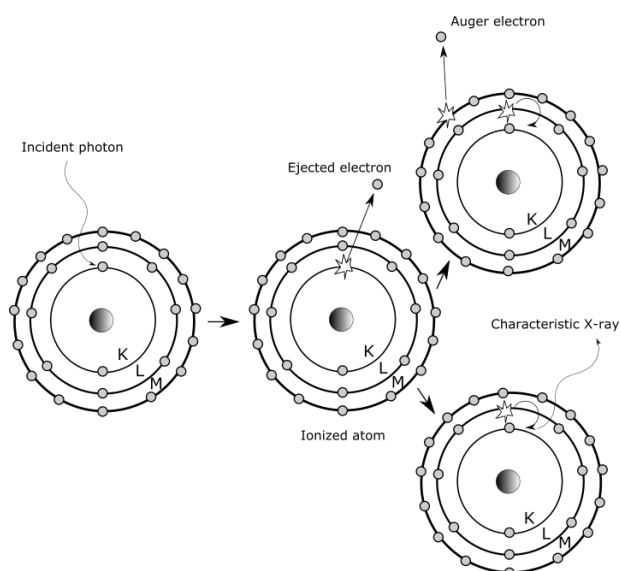
Figure 2.2: Pathways of atom ionization created in Inkscape and adapted from page 2 in
[42]. The ionized atom can return to its initial state by two different processes, by
Auger electron or by characteristic X-ray as an result energy difference between
the initial and final state.

Characteristic emissions energies make identification of the elements in the sample possible [42]. Additionally, by the intensity of the peaks it is possible to estimate the concentration of the elements.

The specimen presentation system, detection system, excitation source, and a system for data collection and signal processing are the basic components of an X-ray Fluorescence spectrometer [42]. The precision and accuracy of a quantitative XRF analysis are dependent on factors such as sample preparation, peak- and background intensities, corrections for matrix effects, and the calibration curve [44]. The first, which is represented by the precision of the analysis, is one of the most common error sources. The sample preparation should be as minimized as possible with a high degree of homogeneity and a flat surface. Systematic errors often occur as a result of the instrument accuracy which, for example, can arise from the calibration curve. A well-calibrated instrument is crucial for accurate results and, hence, it is necessary with regular process control of the calibration procedure. Typically, the intensity of the analyzed elements is measured from reference materials with known compositions. Accurate knowledge of the composition of the reference material is thus a requirement for good results.

2.3.2   X-ray Diffraction

X-ray Diffraction (XRD) is a commonly applied characterization technique for the identification of crystalline phases in a catalyst and crystallite size estimation [45, 20]. The principle behind XRD is scattering of X-ray photons by atoms in a periodic lattice. When the scattered X-ray photons are in phase, constructive interference occurs. From the diffraction of X-rays by crystal planes the lattice spacings can be derived by using the Bragg relation given in Equation (3).

$$n\lambda = 2dsin\theta; \quad n = 1, 2, ... \tag{3}$$

Where:

- λ is the X-rays wavelength.

- d is the distance between two lattice planes.

- θ is the angle between incoming X-rays and the normal to the reflecting lattice plane.

- n is the order of reflection.

The measured angles, 2θ, under which the X-rays are constructively interfering leaves the crystal, Bragg relation (Eq. (3)) give the corresponding lattice spacings that are characteristic for specific compound

[20]. The diffraction pattern is a result of a fraction of the sample being oriented in a manner that ensures a crystal plane at the right angle, θ, to the incident beam for constructive interference. For polycrystalline samples, only a small fraction of the sample particles will form the diffraction pattern. Hence, a way of increasing the contribution of sample particles to the diffraction pattern is to rotate the sample during the analysis.

The crystalline phases present are identified using the resulting diffraction patterns [20]. The diffraction patterns of perfect crystals, display narrow diffraction lines as a result of sufficient range order. In the case of samples with smaller crystallite sizes, these lines will be broader as a result of destructive interference in the scattering direction, indicating that the X-rays are not in phase. This relation is given by Scherrer formula, Equation Equation (4).

$$< L >= \frac{K\lambda}{\beta cos\theta} \tag{4}$$

Where:

- $< L >$ is the particles dimension.
- λ is the wavelength of the X-ray.
- β is the peak width.
- θ is the angle between the beam and the normal on the reflecting plane.
- K is a constant.

Undetected particles as a consequence of too small size or too amorphous material are one disadvantage by using this characterization technique [16]. Additionally, the XRD only gives information about the structure of the bulk [45]. Hence, no information about the surface of the catalyst, where the catalytic activity occurs is provided.

2.3.3 N$_2$ Physisorption

N$_2$ physisorption is used for determination of surface area and pore-size distribution of materials [20]. The technique is based on the physisorption of an inert gas, normally nitrogen, N$_2$. At liquid temperature, one N$_2$ molecule occupies 0.162 m^2, and thus, the number of N$_2$ molecules needed to form a complete monolayer allows for direct determination of the surface area.

The process of N$_2$ physisorption is described by adsorption isotherms of physisorbed species [20]. The Brunaer, Emmett and Teller (BET) isotherm is used for the calculation of the surface area and is presented in Equation (5). The BET isotherm describes the correlation

between the volume N_2 adsorbed at a given partial pressure and the volume adsorbed at monolayer coverage.

$$\frac{P}{V_a(P_0 - P)} = \frac{1}{V_0\chi} + \frac{(\chi - 1)}{V_0\chi}\frac{P}{P_0} \equiv \eta + \alpha\frac{P}{P_0} \tag{5}$$

Where [46, 20]:

- V_a is the total volume adsorbed molecules.
- V_0 is the volume adsorbed molecules in the first monolayer.
- P_0 is the saturation pressure of N_2 at experimental temperature.
- P is the partial pressure of N_2.
- χ is the ratio of desorption rate constants for the second and first layer.

Plotting $\frac{P}{V_a(P_0-P)}$ against $\frac{P}{P_0}$, yields a straight line where the intercept is equal to $\eta = \frac{1}{\chi V_0}$ and slope $\alpha = \frac{\chi-1}{V_0\chi}$ [20]. V_0, the volume adsorbed in the first monolayer can be calculated by $V_0 = \frac{1}{\alpha+\eta}$. The number of molecules adsorbed can be calculated according to Equation (6) [20]:

$$N_0 = \frac{PV_0}{k_B T} \tag{6}$$

where k_B is Boltzmann constant. With known area of the N_2 molecule, the total surface area can be calculated according to Equation (7) [20]:

$$A_T = N_0 A_0 \tag{7}$$

The BET-isotherm is valid under following assumptions [20]:

- The rate of adsorption and desorption is equal in any layer. I.e. dynamic equilibrium between adsorbate and adsorptive.
- Molecules adsorb on the same adsorption sites in the first layer.
- Adsorbed molecules constitute the adsorption site for the following layer.
- Interactions between adsorbate-adsorbate are ignored.
- Adsorption-desorption conditions are different for the first layer, but equal for all subsequent layers.
- The condensation energy is given by the adsorption energy for molecules in the second layer and higher.
- At saturation pressure ($P = P_0$), the multilayer grows to infinite thickness.

Figure 2.3 shows a typical BET isotherm for porous catalysts [20]. As illustrated, the gas gradually occupies the surface with increasing partial pressure. At point B, a monolayer is filled and the curve reaches a plateau. This part of the curve corresponds to the Langmuir Isotherm. A second layer starts to form when the pressure increases further and is followed by formation of multi-layers which causes capillary condensation. Then, a limit is set for the space of gas within the pore. As a consequence of lower equilibrium pressures when the gas is removed, a hysteresis effect occurs.
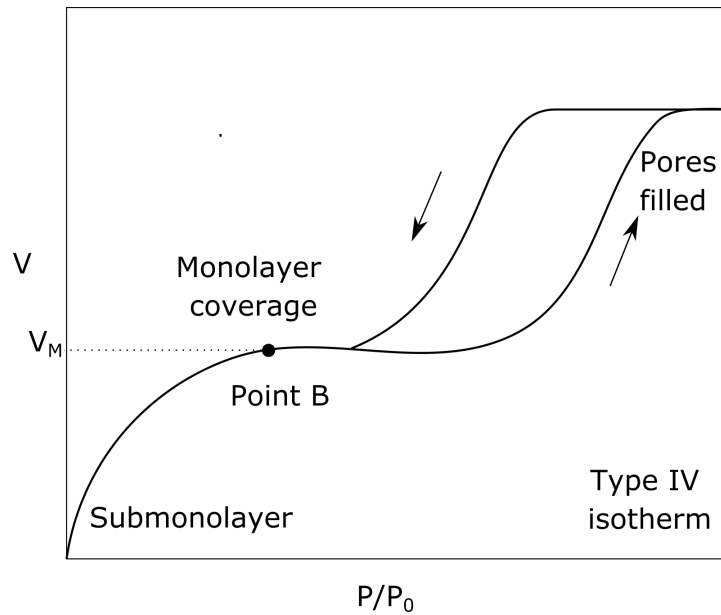
Figure 2.3: An illustration of a type IV BET isotherm. The figure is made in Inkscape and obtained from [20].

For determination of the pore-size distribution, the phenomena of capillary condensation is used [20]. Information about the pore volume and distribution is obtained by applying the Barret-Joyner-Halenda (BJH) model to the desorption isotherm branch. The BJH model is described by the Kelvin equation given in Equation (8).

$$ln(\frac{P}{P_0}) = -\frac{2\sigma V cos\theta}{r_p RT} \qquad (8)$$

Where:

- σ is the surface tension of liquid nitrogen.
- θ is the contact angle.
- V is the molar volume of liquid nitrogen.
- r_p is the radius of the pore.
- R is the gas constant.

- T is the absolute temperature.
- P is the measured pressure.
- P_0 is the saturation pressure.

2.3.4 Transmission Electron Microscopy

Transmission electron microscopy (TEM) is a widely used character-ization technique for the determination of particle size and distribu-tion in catalysts [20]. A schematic setup for TEM is illustrated in Fig-ure 2.4. In TEM, a high energy and intensity beam is passed through condensor lenses and further through a sample [47]. Sample density and thickness are two central factors that affect the attenuation of the beam. When the transmitted electrons are magnified by the elec-tron optics, bright-field (BF) images are obtained. Off-angle diffracted electron beams form dark-field (DF) images, i.e. the transmitted elec-trons form a two-dimensional projection [20]. For supported parti-cles, it is necessary with sufficient contrast between the particles and the support. Thus, this can hinder the detection of well-dispersed sup-ported particles.
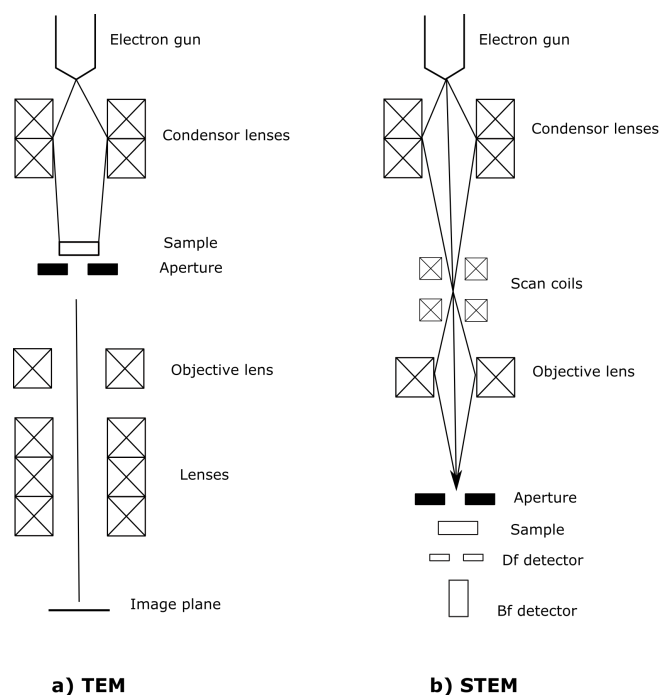
Figure 2.4: An illustration of the set-up of a **a)** transmission electron microscope (TEM) and **b)** scanning transmission electron microscope (STEM). The figure is made in Inkscape and obtained from [47] (p. 182).

In scanning electron microscopy (SEM), an electron beam is focused on the surface of the sample and secondary or backscattered electrons are detected [47]. Depending on energies of the electrons, contrast is made. The secondary electrons applies to the surface region of the sample (low energies) and backscattered electrons are typically scat-tered electrons from heavy elements (high energies). The latter one appears as brighter parts in the image. Scanning transmission electron microscopy (STEM) is a combination of TEM and SEM [47]. In STEM,

small regions of the sample are selected and illuminated, giving either dark- or bright-field images. For example, this is advantageous when analyzing supported catalyst particles. By collecting images in dark-field mode, it is possible to intensify the image contrast of supported metal particles. Diffracted electrons from the metal particles will then form an image. This is called annular dark-field measurements (ADF). It is also possible to carry out measurements at higher angles, high-angle annular dark field (HAADF). Then the image will be composed of scattered electrons by the heavy elements present in the analyzed sample region.

2.3.5 Chemisorption

Chemisorption is a technique for measuring the metal dispersion from the required amount of gas to form a monolayer on the metal surface [48, 46]. Further, chemisorption data can be used to estimate the crystallite size, metal surface area, and the number of active sites. Hence, it can reveal important chemical properties of a catalyst. For example, it can be used for kinetic purposes, such as determining the turnover frequency (TOF). Also, it can discover important matters regarding catalyst deactivation and be used for the optimization of the surface area during catalyst preparation.

CO, H_2 and O_2 are among the commonly used adsorption gases for chemisorption [49]. The choice of adsorption gas depends on the type of support and should have irreversible chemisorption on the metal [39]. For palladium-based catalysts, chemisorption of CO is often chosen over chemisorption of H_2 because of the potential dissolution of H_2 in the palladium metal.

The method of chemisorption requires knowledge of the adsorption stoichiometries [46]. Normally, this is evaluated by measuring the amount adsorbed onto a pure metal(without support) with known surface area. For CO chemisorption, the adsorption stoichiometries are not so consistent [48, 46]. CO can chemisorb onto supported palladium catalysts in linear form and bridge-bonded form, yielding different stoichiometries of 1:1 and 1:2 respectively [50]. Canton *et al.* (2002,[50]) studied the Pd/CO stoichiometry in highly dispersed Pd/γAl$_2$O$_3$ on an experimental basis and reported a Pd/CO average chemisorption stoichiometry close to 2. An assumption of stoichiometry of Pd/CO = 2 will also be used for chemisorption analysis in this thesis.

From the volume of chemisorbed gas, the dispersion can be calculated according to Equation (9), where N_S is the number of metal atoms exposed to the catalyst surface and N_T is the total number of metal atoms [39].

$$D = \frac{N_s}{N_t} \tag{9}$$

Further, the metal dispersion, D, can be expressed by Equation (10) [39]:

$$D = \frac{V_m \cdot n \cdot M_m}{wt\%_{metal} \cdot V_{molar} \cdot m} \cdot 100 \quad [\%] \tag{10}$$

V_m is the volume of chemisorbed gas, n is the stoichiometry factor, m is the sample mass, M_m is the molar mass of the metal, $wt\%_{metal}$ is the weight percentage of the metal in the catalyst and V_{molar} is the standard volume of adsorbate = 22414 cm^3 STP/mol.

The specific metal surface area, A, is given by Equation (11).

$$A = \frac{V_m}{22414} N_A n \frac{1}{m} a_m \frac{100}{wt} \quad [m^2 g^{-1} metal] \tag{11}$$

where V_M is the volume of chemisorbed gas, n is the stoichiometry factor, m is the sample mass, a_m is the atomic cross sectional area, which is 0.0787 nm^2 for palladium, N_A is Avogadro number (6.022· 10^{23} mol^{-1}) and $wt\%$ is the weight percentage of the metal in the catalyst [39].

Equation (12) gives the relationship between the dispersion, D, and the mean particle size, d_{va} with the assumption of spherical particles [39]:

$$d_{va} = \frac{6(v_m/a_m)}{D} \tag{12}$$

where v_m is the volume occupied by an atom in the metal bulk and a_m is the atomic cross-sectional area. v_m is given by

$$v_m = \frac{M_m}{\rho N_A} \tag{13}$$

where M_m is the molar mass of palladium, ρ, is the metal density and N_A is Avogadro number (6.022 · 10^{23} mol^{-1}) [39].

A clean catalyst surface is an important requirement for the method of CO chemisorption [48]. In a typical CO chemisorption analysis, this is fulfilled by the reduction of the metal by hydrogen before it is exposed to chemisorbing gas. At the reduction step, the temperature is still high enough such that the desorption of hydrogen is prompt.

The measured uptake is described by two isotherms, as illustrated in Figure 2.5, where the dispersion is calculated from the difference

between them. The first isotherm describes the total adsorbed gas (chemisorption and physical adsorption) and the second isotherm describes only the physical adsorption. Hence, the difference between the isotherms gives the amount of chemisorbed gas onto the metal surface [48, 46].
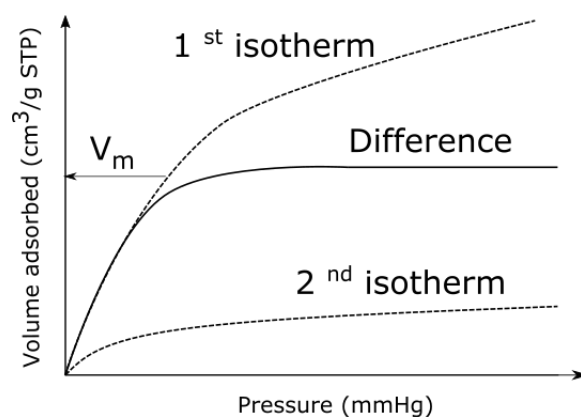
Figure 2.5: An illustration of the isotherms obtained from a chemisorption analysis. The difference between the isotherms represents the volume of gas chemisorbed (V_m). The figure is made in Inkscape and obtained from [49] (p. 51).

2.3.6   Temperature Programmed Reduction

Temperature programmed reduction (TPR) is a used method for characterization of temperatures needed for complete reduction of a catalyst [20]. A typical TPR experiment is described by two phases: pretreatment and adsorption/desorption [51]. The pretreatment is carried out to desorb weakly adsorbed species from the catalyst surface. Normally, this is done by increasing the temperature while keeping the pressure low. For the next phase, adsorption/desorption, the sample is heated linearly while flowing a reducing gas mixture such as H_2/Ar through the reactor where the catalyst sample is placed [39]. The amount of gas reacted is examined by a quantitative technique such as a thermal conductivity detector (TCD) or a mass spectrometer (MS) that measures the gas flow out of the reactor [20, 51]. Several parameters affect the resulting TPR-curve: concentration of reducing agent, the flowrate, sample weight, and temperature rate. Thus, standards for sensitivity and resolution are normally set.

Equation (14) represents the reaction of reduction with H_2. A complete reduction is only possible when n = y [51].

$$M_xO_{y(solid)} + nH_2 \longrightarrow \frac{y-n}{y}M_xO_{y(solid)} + \frac{nx}{y}M_{(solid)} + nH_2O \quad (14)$$
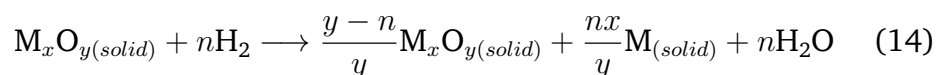
Thus, the reduction of palladium oxide, PdO can be described as Equation (15). The reduction of palladium is regarded as a special case [39]. At low temperatures, palladium hydride is formed and decomposes with further temperature increase.

$$PdO + H_2 \longrightarrow Pd + H_2O \qquad (15)$$
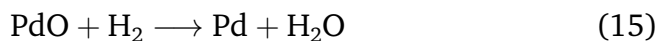
The effect of alloying palladium with silver on the hydrogen solubility is investigated by several authors and is often presented with pressure-composition (p-c) isotherms [52, 53, 54]. These p-c isotherms are described by three phases that occur below a critical temperature, T_c: α-phase, $\alpha+\beta$-phase, and β-phase. The α-phase is representative of a region with low hydrogen content in contradiction to the β-phase with high hydrogen content. The co-existence (plateau region) of the phases ($\alpha+\beta$) is presented by a miscibility gap and the extent of this miscibility gap is reported to vary with both temperature, type of alloy, and with the content of the alloying element. The phase transitions are a result of the arrangement of the adsorbed/desorbed hydrogen which occupies octahedral interstices of the lattice of palladium. When alloying with silver, the lattice size and d-band holes are affected and hence, the hydrogen solubility, plateau region, and miscibility gap is too [54].

The variation of hydrogen solubility in palladium and palladium-silver was studied by Fazle Kibria and Sakamoto (2000, [54]) using a gas phase method. They found that the lattice parameter of Pd-Ag expanded compared with pure Pd. From p-c isotherms, it was demonstrated that the miscibility gap value was decreased significantly upon addition of Ag. This was attributed to increased low pressure hydrogen solubilities as a concequence of extended lattice parameter of Pd-Ag.

2.4 Gas Chromatography

Gas Chromatography (GC) is an analytical separation technique used to obtain information about the quantity and composition of a mixture [55]. A typical gas chromatograph consists of an injector, carrier gas, detector, column, and a data system. The sample is injected into a preheated injection chamber where it evaporates and is transported to the column with a carrier gas (mobile phase) [56]. In the column, the sample is separated and further transported to a detector where the different components are detected and registered. The temperature of the column varies and depends on the components being separated. The components are normally separated after their boiling points, whereof the components with high boiling point pass through

the column slower than the components with lower boiling point. The detector gives a signal proportional to the concentration or amount of the components.

2.4.1 Mobile Phase

The mobile phase is a carrier gas that is inert and the functionality is to carry the sample through the column, without entering the chemistry of the process [57]. High purity is a critical requirement for the mobile phase and normal gases used for this phase is argon, nitrogen, helium or hydrogen. The choice of carrier gas is based on the detector used in the GC. For example for a thermal conductivity detector(TCD), the carrier gas is normally helium, or hydrogen because of their high thermal conductivity [57].

2.4.2 Stationary Phase

Selection of the stationary phase is the critical step in configuration of a method in the GC [57]. The stationary phase is normally a liquid with high boiling point, but it can also be a solid adsorption material [56]. The stationary liquid phase can be both coated on the wall of an open tube (WCOT) or coated on a solid material and packed into the column (packed-column GC).

2.4.3 Detector

The most common detectors are thermal conductivity detector (TCD), flame ionization detector (FID) and electron capture detector (ECD) [57].

TCD, which is utilized in this thesis, is a concentration detector [57]. A requirement for the carrier gas in a TCD is that the thermal conductivity should be considerably different from the sample that is analyzed. As previously mentioned, helium and hydrogen gases with high thermal conductivity make them suitable mobile phases for TCD. FID is based on the production of ions while burning a sample in an oxygen-hydrogen flame [57]. The produced ions are collected and comprise a small current. This current is intensified and transferred to a data system. The ECD is also an ionization detector, but in contrast to FID, it is concentration-based as the TCD and selective for electron-halogen- and nitrogen capturing compounds.

2.5   Catalytic Activity

Expressing the activity of a catalyst is complex and there are several ways of doing so. For instance, it can be expressed as turnover frequency (TOF), reaction rate, space velocity, or as the temperatures needed to reach different levels of conversion [20]. By the latter way, it should be noted that the temperature will affect the overall rate of a catalytic reaction in a more complicated matter.

2.5.1   Calculation of Methane and CO Conversion

The conversion of CH_4/CO can be calculated according to Equation (16). *A* denotes component A, being CH_4 or CO.

$$X_A = \frac{F_{A,in} - F_{A,out}}{F_{A,in}} \tag{16}$$

where X_A is the conversion of *A* given by the amount of *A* reacted.

The flow of component *A* is given by Equation (17) where y_i is the mole fraction of component *A* in the gas phase, $F_{tot,i}$ is the total gas flow and *i* is the inlet or outlet of the reactor.

$$F_{A,i} = y_i \cdot F_{\text{tot,i}} \quad [ml\ min^{-1}] \tag{17}$$

The mole fraction of component *A* in gas phase, y_A, is expressed by Equation (18). This is relevant for all species in gas phase of the system (H_2, O_2, N_2, CO_2, CH_4, CO). S_A is the peak area which is multiplied by the response factor, k_A.

$$y_A = S_A \cdot k_A \tag{18}$$

Insertion of Equation (17) to Equation (16), yields Equation (19) for the conversion of component *A*.

$$X_A = \frac{y_{A,in} \cdot F_{tot,in} - y_{A,out} \cdot F_{tot,out}}{y_{A,in} \cdot F_{tot,in}} \tag{19}$$

The system is in stoichiometric balance when all reactants are converted into the desired products and $F_{tot,in} = F_{tot,out}$. N_2 is used as inert gas for the system and does not enter the reaction. Thus, the concentration of nitrogen can be used to calculate the total flow in and out for the system, as expressed by Equation (20) and Equation (21).

$$F_{tot,in} = \frac{F_{N_2,in}}{y_{N_2,in}} \tag{20}$$

$$F_{tot,out} = \frac{F_{N_2,out}}{y_{N_2,out}} \tag{21}$$

The concentration of nitrogen is constant and independent of the reactor point. Thus is can be expressed as Equation (22). Using this relation, the final expression for the conversion of component A can be simplified to Equation (23).

$$F_{N_2,in} = F_{N_2,out} \tag{22}$$

$$X_A = 1 - \frac{y_{A,out}}{y_{A,in}} \cdot \frac{y_{N_2,in}}{y_{N_2,out}} \tag{23}$$

2.5.2 Carbon Balance

A mass balance over the carbon in the system was performed to check if all carbon from CH_4/CO was converted to CO_2. In that case, Equation (24) would be valid.

$$F_{A,in} = F_{A,out} + F_{CO_2,out} \tag{24}$$

Thus, the carbon balance of the system, E_C, can be checked according to Equation (25).

$$E_C = 100\% \cdot (1 - \frac{F_{A,in}}{F_{A,out} + F_{CO_2,out}}) \tag{25}$$

Inserting previous derived relations into Equation (26), the final expression for the carbon balance is given by Equation (26).

$$E_C = 100\% \cdot (1 - \frac{y_{A,in}}{y_{N_2,in}} \cdot \frac{y_{N_2,out}}{y_{A,out} + y_{CO_2,out}}) \tag{26}$$

2.5.3 Kinetics

The rate at which a catalytic reaction takes place is described by the kinetics of the reaction [20]. Furthermore, kinetics makes it possible to relate the rate to a reaction mechanism and to process parameters such as pressure, concentration, and temperature. Catalytic reactions are a set of several linked reactions making it advanced to describe

the kinetics. Today, several kinetic models are used to describe the kinetics of a catalytic reaction, e.g. Langmuir-Hinshelwood (LH), Mars-Van-Krevelen (MvK), and Eley-Rideal (ER).

The LH kinetics is based on an assumption that all species are adsorbed and in thermal equilibrium with the surface before any reaction takes place [20]. This means that the species are in a chemisorbed state on the surface when they react. MvK is a model normally used to describe reactions on oxide catalysts [58]. The model is based on a redox cycle where the surface is primarily reduced before it is re-oxidized with oxygen from the gas phase. For the ER mechanism, one of the reactants is not accommodated at the surface but reacts out of the gas phase. For CO oxidation, this corresponds to CO reacting with adsorbed oxygen without being adsorbed itself [59, 20].

Mars-van Krevelen mechanism and Langmuir-Hinshelwood mechanism are among the suggested mechanisms for complete oxidation of methane over Pd/Al_2O_3 [16, 22]. Both the reduced and oxidized forms of palladium seem to catalyze methane oxidation, but with PdO as the active phase, Hayes *et al.* (2001, [22]) reported that the complete oxidation of methane proceeds through a MvK mechanism. This implies that methane reacts with lattice oxygen of PdO and the rate-determining step is assumed to be the activation of the primary C-H bond of the methane molecule. The model of methane oxidation according to the LH mechanism is described by adsorbed methane molecules reacting with atomic oxygen atoms [60].

Although being a relatively simple reaction, the kinetics of low-temperature oxidation of CO are much scrutinized and the temperature dependence of the reaction rate is of large interest [20]. Langmuir-Hinselwood and Eley-Rideal are among the proposed mechanisms for complete oxidation of CO [59]. Assuming that the reaction proceeds through a LH mechanism, the rate-determining step is the recombination of CO and O into CO_2 (step 3):

1. CO + * $\rightleftharpoons$ CO*

2. O_2 + 2* $\rightleftharpoons$ 2O*

3. CO* + O* $\rightleftharpoons$ CO_2* + *

4. CO_2* $\rightleftharpoons$ CO_2 + *

The surface is mainly covered by CO in the low-temperature region of CO oxidation, i.e. CO is strongly adsorbed to the surface, giving no active sites for activation of O_2 [21]. This gives a rate expression for CO oxidation dominated by K_{CO}, yielding a negative reaction order for CO[20]:

$$r = \frac{k_3^+ \sqrt{K_2 p_{O_2}}}{K_1 p_{CO}} \tag{27}$$

Then, as observed by Equation (27), the reaction order is -1 for CO and $+\frac{1}{2}$ for O_2 [20]. At increasing temperatures, CO desorbs and O_2 are gradually activated. The order for CO becomes positive and the term $(K_2[O_2])^{\frac{1}{2}}$ in the rate expression is no longer insignificant:

$$r = k_3^+ K_1 \sqrt{K_2} p_{CO} \sqrt{p_{O2}} \tag{28}$$

For higher temperatures, the orders in CO and O_2 are then $+1$ and $+\frac{1}{2}$ for CO and O_2, respectively [20]. Hence, the interpretation of reaction orders of the overall reaction of CO oxidation is not straightforward and they will only be valid for a selection of reaction conditions.

For simplicity, first-order dependence for component A (CH_4/CO) and differential conditions will be assumed for the calculations in this study. This yields an expression for the reaction rate given in Equation (29).

$$r = \frac{GHSV \cdot X \cdot C_{A0}}{V_{molar}} \qquad [\frac{mol}{h \cdot g_{cat}}] \tag{29}$$

where r is the reaction rate, X is the conversion of methane/CO, V_{molar} is the standard volume of an ideal gas = 22414 ml/mol, $GHSV$ is the gas hourly space velocity given in Equation (30) and C_{A0} is the concentration of CH_4/CO in the feed.

$$GHSV = \frac{F_{tot}}{m_{cat}} \qquad [\frac{NmL}{h \cdot g_{cat}}] \tag{30}$$

where F_{tot} is the total feed flow and m_{cat} is the mass of catalyst.

When studying the intrinsic kinetic performance of a catalyst, transport limitations that influence the overall or apparent activation energy should be eliminated [20]. This is possible by, for example, using small catalyst particles, low conversion, and moderate temperature.

2.5.4   Activation Energy

The activation energy is defined as the energy needed for a reaction to happen [61]. A catalyst is able to increase the rate of reaction by decreasing the activation energy, as illustrated in Figure 2.6. The temperature dependency of the rate constant is given by Arrhenius Equation [20]:

$$k(T) = v e^{\frac{-E_a}{RT}} \tag{31}$$

where v is the pre-exponential factor, E_a is the activation energy, T is the temperature and R is the gas constant.
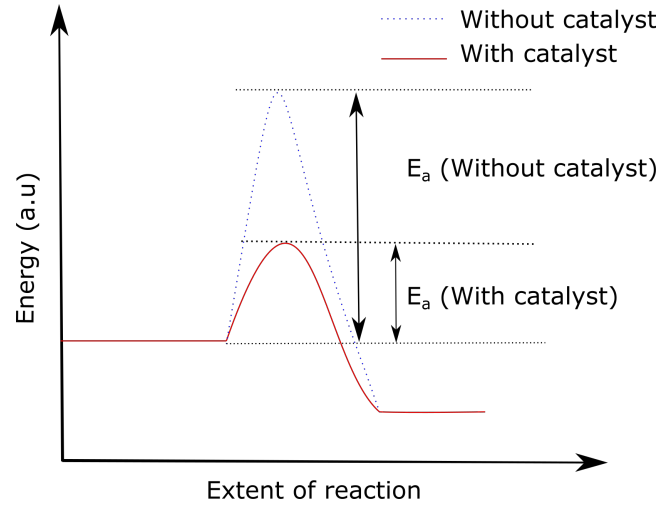
Figure 2.6: Illustration of an energy diagram describing the activation energy with (red) and without (blue) catalyst. The figure is made in Inkscape and obtained from [61].

For a reaction with first order with respect to component A, the reaction rate is given by Equation (32), [62].

$$- r = k \cdot C_A \tag{32}$$

where k is the reaction rate constant given in Equation (31), and C_A is the concentration of component A. C_A is given by

$$C_A = C_{A0}(1 - X_A) \quad [\frac{mol}{L}] \tag{33}$$

where C_{A0} is the entering concentration of component A and X_A is the conversion of component A.

The design equation for a packed bed reactor (PBR) is given in Equation (34) [62]. For a packed bed reactor, the rate is dependent on the weight of catalyst bed, W, and the molar flow rate of component A.

$$\frac{dF_A}{dW} = r_A \tag{34}$$

The molar flow rate of component A, F, is given by

$$F = C \cdot q \quad [\frac{mol}{min}] \tag{35}$$

The volumetric flowrate, q, is expressed as volume of the reactor, V_R, divided by the residence time, τ, represented in Equation (36).

$$q = \frac{V_R}{\tau} \quad [\frac{mL}{min}] \tag{36}$$

The reactor volume is given by the weight of the catalyst divided by the catalyst density [62].

$$V_R = \frac{W}{\rho} \quad [cm^3] \tag{37}$$

By the insertion of Equation (32) and (35) into Equation (34) and using the relations given in Equation (36) and Equation (37), Equation (34) can be expressed as Equation (38). The weight and density of the catalyst are constants.

$$\frac{dC_A}{d\tau} = -k \cdot C_A \tag{38}$$

Integration of Equation (38) gives Equation (39). By insertion of the expression given for the concentration of component A (Equation (33), yields Equation (40).

$$ln C_A = k\tau \tag{39}$$

$$- ln(1 - X_A) = k\tau \tag{40}$$

Linearization of Equation (38) gives Equation (41):

$$ln(-ln(1 - X_A)) = ln(A) - \frac{E_A}{R} \cdot \frac{1}{T} \tag{41}$$

where E_A is the activation energy and R is the gas constant. Plotting ln(-ln(1 - X_A)) against 1/T gives a straight line with slope $-E_A/R$. An estimation of the activation energy can therefore be made by multiplying the slope $-E_A/R$ with the negative gas constant, R.

The apparent activation energy is highly dependent on diffusion limitations, as illustrated in Figure 2.7 [20]. The figure shows that the reaction rate increases with increasing temperature until a certain point. At this point, the catalyst activity is so high that the transport of the reactants is slower than the rate of reaction. For catalyst testing, it is therefore advantageous to keep the temperature below the pore diffusion point. It is desirable to use the full efficiency of the

catalyst while keeping the reaction rate as high as possible. Oxidation reactions are fast reactions at higher temperatures and transport limitation may effect the catalytic activity. By investigating the apparent activation energy in an Arrhenius plot, pore diffusion or transport limitations can be revealed.
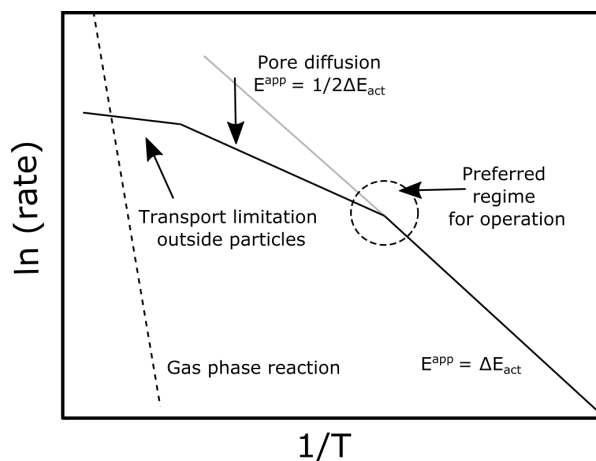
Figure 2.7: An Arrhenius plot illustrating the effect pore- and transport limitations has on the apparent activation energy. The figure is made in Inkscape and obtained from [20], (p. 222).

Chapter 3

Experimental

3.1 Risk Assessment

The safety measures and risk associated with this research was schematically entered in the NTNU Risk Assessment protocol with ID-number 40054. The risk assessment can be reviewed in Appendix E. Further, the after-hours agreement of the Norwegian University of Science and Technology was approved and followed.

The highest risk associated with this work was the utilization of combustible gas, CH_4 and the toxic gas, CO. After evaluation, the risk was considered acceptable. All experiments were performed in a closed rig provided with a ventilation system and gas sensors. Additionally, gas leakage tests were performed before every experiment.

For the catalyst synthesis, several corrosive materials were used: $AgNO_3$ and $Pd(NO_3)_2 \cdot 2H_2O$. When these materials were in use, suitable protective equipment was employed and the disposal regulations were followed carefully.

3.2 Catalyst Synthesis

Two palladium-based catalysts was synthesized during the research: 2.0 wt% Pd/Al_2O_3 and (1.5 wt%)Pd-(0.5 wt%)Ag/Al_2O_3, both with a total loading of 2 wt% active material. The objective was to investigate the effect of replacing a portion of a palladium-based catalyst with a cheaper element. $Pd(NO_3)_2 \cdot 2H_2O$ (Sigma Aldrich) and $AgNO_3$ (Thermo Fisher) were used as precursors for palladium and silver, respectively. The support was γ-Al_2O_3 (Puralox SCCa 5-200).

The catalysts were prepared according to the incipient wetness impregnation method presented in Section 2.2, whereby a co-impregnation was used for the bimetallic catalyst. The support, γ-Al_2O_3 was pretreated in a high-temperature furnace at 600 °C for 6 hours and with

a heating rate of 5 °C/min. Furthermore, the support was sieved to obtain a particle size of 75-100 μm.

The volume needed for saturation of the support material was determined by dripping water to the surface of the support. The weight of water needed to reach the saturation point was noted. The calculations of precursors, $Pd(NO_3)_2$·$2H_2O$ and $Ag(NO_3)$, needed to obtain 2wt% active material are presented in Appendix A. The precursors were dissolved in de-ionized water and dripped onto the support before it was dried at 120 °C for 3 hours with regularly mixing. The catalysts were calcined in a standard quartz calcination reactor with a maximum temperature of 500 °C and air as calcination gas. The heating rate was 5 °C/min and the maximum temperature was kept for 2 hours. An overview of the quantities of precursors and support can be viewed in Table 3.1.

Table 3.1: The amount of precursors and support needed for synthesis of 2wt% Pd/Al_2O_3 and 2wt% Pd(1.5 wt%)-Ag(0.5 wt%)/Al_2O_3.

Catalyst	Mass [g] $Pd(NO_3)_2$· $2H_2O$	Mass [g] $Ag(NO_3)$	Mass [g] γ-Al_2O_3
Pd/Al_2O_3	0.5074	-	10.003
Pd-Ag/Al_2O_3	0.3832	0.080	10.004

The catalyst particles were sieved with a size fraction 250-425 μm for the catalytic activity experiments. The particles smaller than 250 μm were pelletized, crushed, and re-sieved through suitable sieves.

3.3 Catalyst Characterization

3.3.1 X-ray Fluorescence

The composition of the catalysts was analyzed using X-ray Fluorescence. For the analysis, a Wavelength Dispersive X-ray Fluorescence (WDXRF) Supermini200 analyzer was used. A Pd-source was used for the generation of X-rays.

The preparation of the sample was conducted carefully to achieve good and reliable results. Approximately 0.2 g of sample was mixed and crushed with 2.0 g of boric acid, H_3BO_3, for 10 minutes to obtain a homogeneous mixture. The mixture was pelletized to a 40 mm diameter pellet, placed in a sample holder, and covered with 6 μm polypropylene film for analysis.

The amounts of catalysts and H_3BO_3 used for XRF analyses are presented in Table 3.2. Two pellets of Pd/Al_2O_3 was prepared and analyzed twice to examine the reliability and accuracy of the procedure. In addition, each pellet was analyzed twice.

Table 3.2: The amount of sample and sample binder, H_3BO_3 for analysis of catalyst composition using X-ray Fluorescence.

Sample	Catalyst	m_{sample}[g]	$m_{H_3BO_3}$ [g]
1	Pd/Al_2O_3	0.2032	2.8072
2	Pd/Al_2O_3	0.2094	2.8054
3	$Pd-Ag/Al_2O_3$	0.2030	2.8002

3.3.2 X-ray Diffraction

The XRD analysis was performed in a Bruker D8 A25 DaVinci X-ray diffractometer with CuKα radiation. DIFFRAC EVA was used to analyze the results. The analysis parameters are listed in Table 3.3.

Table 3.3: The parameters for X-ray Diffraction analysis of the samples.

2θ [°]	10-90
Step change [° $step^{-1}$]	0.044
Time [min]	60
Divergence slit	V6

3.3.3 N_2 Physisorption

N_2 physisorption was used to analyze the surface area and pore volume of the catalysts and the support material. The N_2 adsorption measurements were conducted with a Micromeritics TriStar II 3020 Surface Area and Porosity Analyzer.

Depending on the material, 150-200 mg of sample was weighed and transferred to a sample tube. The samples were evacuated for 1 hour at ambient temperature before they were transferred to a heating station and degassed overnight at 200 °C. The sample mass was corrected by weighing the sample tube after the degas step. Further, the apparatus dewar was filled with liquid nitrogen and the sample tubes were installed. The weights of the sample tubes, before and after degas, are presented in Table 3.4.

Table 3.4: The weight of the tubes, tubes+sample before and after degassing and the final sample mass for N_2 physisorption.

Catalyst	$m_{(T)}$[g]	$m_{(T+S)}$ [g]	$m_{(T+S)final}$ [g]	$m_{(S)}$ [g]
Al_2O_3	26.0706	26.2184	26.2137	0.1431
Pd/Al_2O_3	26.7049	26.8996	26.9082	0.2033
$Pd-Ag/Al_2O_3$	26.7026	26.9179	26.9077	0.2051

3.3.4 Transmission Electron Microscopy

Investigation of the particle size, distribution, and location of palladium and silver relative to each other, was performed with transmission Electron Microscopy (TEM) and scanning transmission electron

microscopy (STEM). The experimental procedure was conducted by Senior Research Scientist Per Erik Vullum at SINTEF Industry, Department of Materials and Nanotechnology. The author of this thesis was present throughout the analyses.

The powders were dispersed in isopropanol and ultrasonicated for 10–15 min to avoid agglomeration. A droplet was transferred to a lacey, amorphous carbon-coated Cu TEM grid. Before each of the samples was loaded into the TEM column, gentle plasma cleaning was performed (2 x 10s) to remove potential hydro-carbon contamination. During plasma cleaning, a 75% Ar – 25% O_2 gas mixture is ionized and flushed across the sample. The oxygen ions react with and remove weakly bonded carbon.

TEM was performed with a double Cs aberration-corrected cold FEG JEOL 200FC, operated at 200 kV. This instrument is equipped with a large solid angle (covering 0.98 sr solid angle) Centurio detector for energy-dispersive X-ray spectroscopy (EDS) and a GIF Quantum ER for electron energy loss spectroscopy (EELS). EDS and dual EELS mapping were performed simultaneously in scanning transmission electron microscopy (STEM) mode.

3.3.5 Chemisorption

The dispersion and particle size of the metals in the catalysts were analyzed using CO chemisorption. The analyses were performed in a Micrometrics ASAP 2020 instrument. A small layer of quartz wool was placed at the bottom of the glass reactor before filling it with approximately 150 mg of catalyst sample. An additional layer of quartz wool was put on top of the catalyst bed. To avoid possible leakage, the o-rings were cleaned with ethanol, and gloves were used. The outer part of the reactor was also washed with ethanol. The reactor was connected to the instrument and the sample was evacuated and kept under vacuum for approximately 1 hour. Before starting the analysis, a leakage test was conducted until the pressure change was less than 50 μmHg/min. The analysis conditions are listed in Table 3.6. After the analysis, the sample was reweighed and in the case where the weight was changed, the new weight was added to the sample information.

Table 3.5: Sample information for chemisorption analysis. $m_{sample,before}$ represents the mass before the analysis and $m_{sample,after}$ represent the mass after analysis used to update the software after analysis.

Catalyst	$m_{sample,before}$ [g]	$m_{sample,after}$ [g]
Pd/Al$_2$O$_3$	0.1540	0.0922
Pd-Ag/Al$_2$O$_3$	0.1543	0.1329

Table 3.6: The analysis conditions used for CO chemisorption.

Step	Task	Gas	Temperature [°C]	Rate [°/min]	Time [min]
1	Evacuation	He	200	10	10
2	Leak Test		200	10	
3	Evacuation	He	100	10	10
4	Flow	H$_2$	400	10	30
5	Evacuation		400	10	30
6	Evacuation		35	10	30
7	Leak Test		35	10	
8	Evacuation		35	10	10
9	Analysis	CO	35	10	

3.3.6 Temperature Programmed Reduction

The reducibility of the catalysts was investigated by temperature-programmed reduction (TPR). The analysis was performed with a BenchCAT Hybrid 100 HP and with analysis conditions presented in Table 3.7. As treatment gas, 7%H$_2$/Ar was used and the treatment was conducted over a temperature range of 50-800 °C.

Approximately 120-150 mg of sample was transferred to a quartz tube reactor and covered by quartz wool on the bottom and the top of the catalyst bed. Further, the reactor was attached to the instrument and subjected to two leakage tests to ensure no leaks. A flow of inert gas was first introduced to the system, and leakage was checked with foam. Further, a flow of hydrogen was introduced and checked for leakage by a CO detector. The temperature program consisted of three parts: pre-treatment, temperature-programmed reduction, and post-treatment. Two analyses were performed for Pd-Ag/Al$_2$O$_3$ to obtain a measure of reproducibility and error.

Table 3.7: Analysis parameters and amount of catalyst sample used for analyzing the reduction-profile of the different catalysts.

Material	m$_{sample}$ [g]	H$_2$/Ar [%]	Flow [ml min^{-1}]	Heating rate [° C min^{-1}]
Pd/Al$_2$O$_3$	0.1569	7	40	10
Pd-Ag/Al$_2$O$_3$[1]	0.1351	7	40	10
Pd-Ag/Al$_2$O$_3$[2]	0.1462	7	40	10

3.4   Activity Tests

The catalysts were tested in an adapted test rig for CH_4 oxidation and CO oxidation. The test rig was built by Ph.D candidate Junbo Yu and a simplified flow sheet over the rig is presented in Figure 3.1. The test rig was equipped with several mass flow controllers (MFCs) for control of the feed stream composition of CH_4/CO, N_2, H_2 and air. A μGC (Agilent 990 MicroGC) with three columns was used for analysis of the product stream composition. The reactor used for catalyst testing was a quartz reactor, illustrated in Figure 3.2.
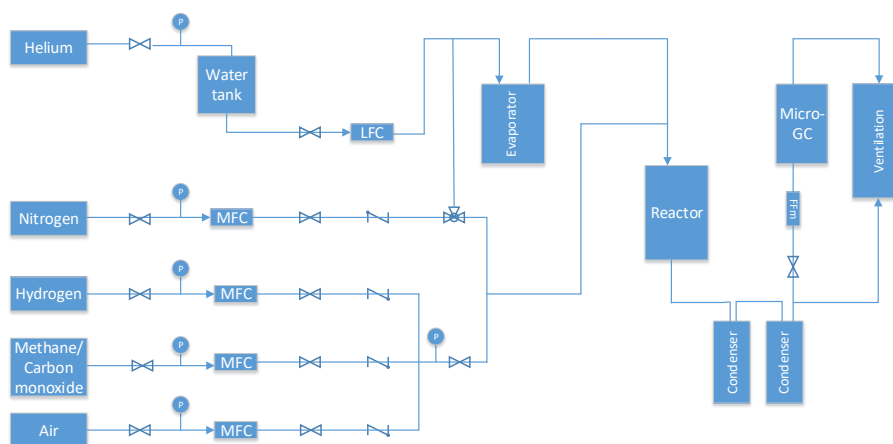
Figure 3.1: Simplified flowsheet illustrating the test rig for methane and CO oxidation experiments. MFC is an abbreviation for mass flow controller, LFC for liquid flow controller, Micro-GC for Micro Gas Chromatograph and FFm for Float Flow Meter. The figure is made in Visio 2016.

The catalyst bed consisted of approximately 200 mg of the catalyst with a size fraction 250-425 μm and approximately 2.0 g of silicon carbide (SiC) with particle size 270 μm. The choice of size fraction of the materials was based on findings during previous work on this project [12, 13]. SiC was used as a dilutant to hinder the formation of hot spots and to prevent bypass. The size fraction of catalyst and inert was chosen to avoid high pressure drop over the catalyst bed. Before every experiment, the height of the catalyst bed was measured.

After loading the catalyst bed, the reactor was installed in the reaction rig and covered by insulation material. A thermocouple was inserted in the T-pocket at the bottom of the reactor for temperature measurement in the catalytic bed. The thermocouple was placed approximately in the middle of the catalytic bed. Before running experiments, leakage tests with nitrogen and hydrogen were performed to ensure that the connections between the reactor and the feed- and product lines were tight. First, a flow of N_2 was fed to the reactor and

the connections was checked with leakage foam. If no bubbles were formed, 20 ml/min of H_2 in 100 ml/min N_2 was fed to the reactor and checked with a gas detector with sensitivity for H_2 and CO. Afterwards, the reactor was flushed with N_2 until all H_2 was removed from the lines.

In total, two catalysts, Pd/Al_2O_3 and $Pd\text{-}Ag/Al_2O_3$, were tested in low-temperature oxidation of CH_4 and CO. The conditions applied for the different reactions will be presented in the following sections.
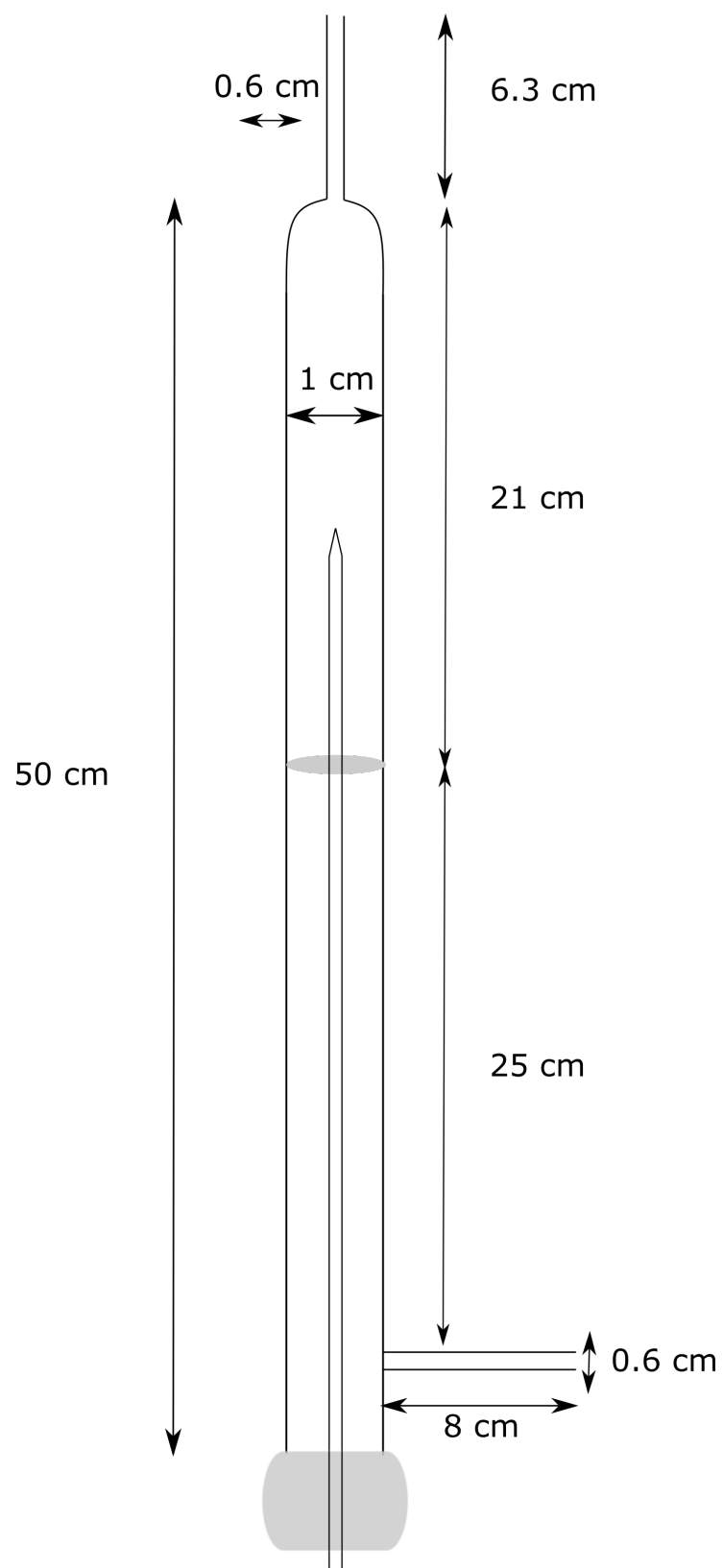
Figure 3.2: Illustration of the quartz reactor used for catalyst testing. The illustration is made in Inkscape.

3.4.1 Methane Oxidation

The conditions applied for methane oxidation were based on the reaction conditions specific to lean-burn NGV engine exhausts, presented in Section 2.1.1 [3]. With this as a basis, the methane concentration was kept low and the oxygen concentration high throughout all experiments. The methane- and oxygen concentration were both kept constant, with concentrations of 2% and 10% respectively. Two different feed gas compositions were performed over the catalysts, with and without water vapor. As the NGV engine exhaust contains large amounts of water vapor, it was decided to investigate the influence of water on the catalytic activity. Based on the theory presented in Section 2.1.1, the concentration of H_2O was set to 10 mol%.

The stability of the catalyst was tested by investigating the catalytic activity after time on stream. Then, the temperature was kept constant over a longer time period at three different temperatures, 350 °C (48 h), 300 °C (12 h) and 250 °C (48 h). The flow parameters for dry and wet experiments are listed in Table 3.8 and Table 3.9.

Gas	Flow [Nml min^{-1}]
CH_4	4
N_2	100.75
Air	95.25

Table 3.8: Feed gas composition and flow rate for the reactant feed mixture used for methane oxidation under dry conditions. Total flowrate = 200 ml min^{-1}.

Gas	Flow [Nml min^{-1}]
CH_4	4
N_2	80.75
Air	95.25
H_2O	20

Table 3.9: Feed gas composition and flow rate for the reactant feed mixture used for methane oxidation under wet conditions. Total flowrate = 200 ml min^{-1}.

The temperature program used for methane oxidation is illustrated in Figure 3.4. The maximum temperature was set to 550 °C and the temperature was increased and decreased systematically with a ramp rate of 5 °C min^{-1} and an increment of 25 °C for each step. At each temperature step, the temperature was held constant for 30 minutes. The decision of temperature program was made in accordance with previous work performed on this project [12, 13]. For wet experiments, steam was introduced at 200 °C. Before the wet experiments, the gas lines were heated to approximately 150 °C to avoid condensation in the lines. Steam was generated by introducing a mixture of nitrogen and water to an evaporator, as illustrated in Figure 3.1.
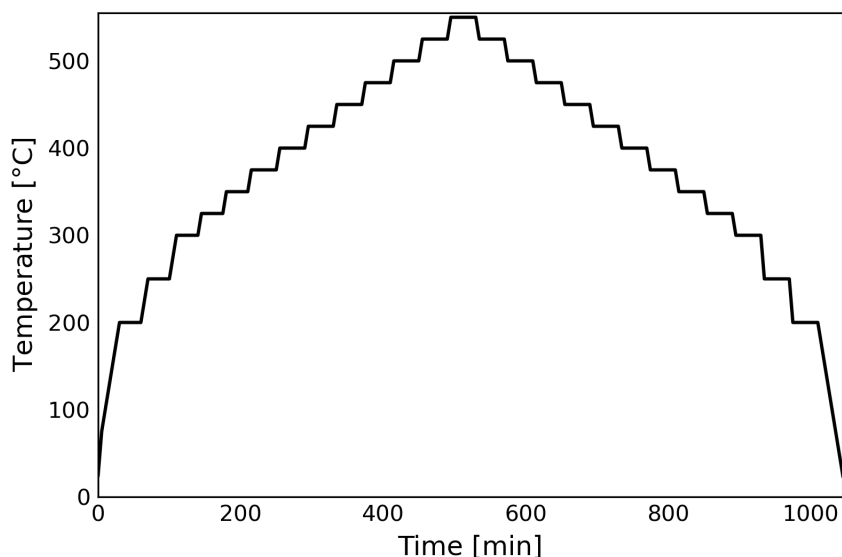
Figure 3.3: The temperature program used for catalyst testing. Each step was increments of
25 °C with heating rate of 5°C min^{-1}. The temperature was held constant for 30
minutes at each heating/cooling step.

The amount of catalyst and silicon carbide used for catalyst testing in
methane oxidation are listed in Table 3.10. Multiple reaction cycles
were performed to assess the catalytic activity after time on stream. It
should be noted that the long-term experiment was conducted after
the three reaction cycles. In addition, a dry experiment was conducted
both before and after the wet experiment to validate if the deactiva-
tion was reversible.

Table 3.10: The amount of catalyst, m$_{cat}$, inert, m$_{SiC}$ and the height of the catalyst bed used
in methane oxidation.

Catalyst	m$_{cat}$ [g]	m$_{SiC}$ [g]	Height of catalyst bed [mm]
Pd/Al$_2$O$_3$	0.2006	2.0159	22
Pd/Al$_2$O$_3$ $_{10\%_{H_2O}}$	0.2019	2.0109	22
Pd-Ag/Al$_2$O$_3$	0.2014	2.0037	22
Pd-Ag/Al$_2$O$_3$ $_{10\%_{H_2O}}$	0.2007	2.0041	22

3.4.2   CO Oxidation

CO oxidation was performed using the same reaction conditions as
methane oxidation to have a basis for comparison. In addition, the
dependency of CO concentration was investigated over two different
reactant feeds, 2 mol% and 5 mol% CO respectively. In total, three
CO oxidation cycles over each catalyst were performed, one with 2
mol% CO and maximum temperature of 550 °C and two with 2 mol%

CO and maximum temperature of 300 °C. For both temperature programs, a heating rate of 5 °C and an increment of 25 °C were used. The temperature program for the first cycle is illustrated in Figure 3.3 and for the two last in Figure 3.4. The different feed gas composition for CO oxidation are presented in Table 3.11 and 3.12.

Table 3.11: Feed gas composition and flow rate for the reactant feed mixture used for CO oxidation with 2 mol% CO in the reactant feed. Total flowrate = 200 ml min^{-1}.

Gas	Flow [Nml min^{-1}]
CO	4
N$_2$	100.75
Air	95.25

Table 3.12: Feed gas composition and flow rate for the reactant feed mixture used for CO oxidation with 5 mol% CO in the reactant feed. Total flowrate = 200 ml min^{-1}.

Gas	Flow [Nml min^{-1}]
CO	10
N$_2$	94.75
Air	95.25
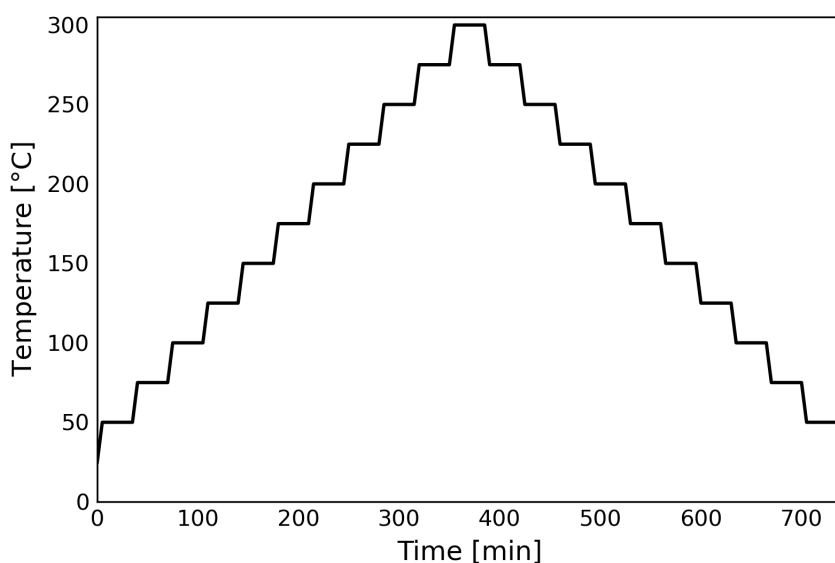
Figure 3.4: The temperature program used for catalyst testing with 5% CO. Each step was increments of 25 °C with heating rate of 5°C min^{-1}. The temperature was held constant for 30 minutes at each heating/cooling step.

In addition, a long-term experiment was performed to check potential deactivation after time on stream. This experiment was conducted without dilutant to enable post-reaction characterization. The catalytic activity was not investigated for this long-run, and it was only

used for characterization. The feed gas composition for this experiment is listed in Table 3.12.

The amount of catalyst, m_{cat}, inert, m_{SiC} and the height of the catalyst bed for CO oxidation are presented in Table 3.13.

Table 3.13: The amount of catalyst, m_{cat}, inert, m_{SiC} and the height of the catalyst bed used in CO oxidation.

Catalyst	m_{cat} [g]	m_{SiC} [g]	Height of catalyst bed [mm]
Pd/Al$_2$O$_3$	0.2012	2.003	22
Pd-Ag/Al$_2$O$_3$	0.2008	2.006	22
Pd-Ag/Al$_2$O$_3$ (TEM)	0.2013	-	4

Chapter 4

Results and Discussion

4.1 Catalyst Characterization

In the following sections, the results from the characterization of the materials will be presented and discussed. Repetitive analyses were performed for all characterization techniques to evaluate the accuracy of the instruments and procedures.

4.1.1 X-ray Fluorescence

The results from X-ray Fluorescence analyses are presented in Table 4.1, along with the nominal mass% calculated according to Equation (A.9) in Appendix A.2. The results were compared with the nominal mass percentage and smaller amounts of palladium and silver than the nominal mass percentage were found for both of the catalysts.

Table 4.1: The results from X-ray Fluorescence analysis of catalysts. The amount of the different elements are given as mass percentages and compared with the nominal mass percentages calculated according to Equation A.9 in Appendix A.2. The deviation from the nominal mass percentage is denoted as d, and calculated according to Equation B.1 in Appendix B.1.

Catalyst	Element	Mass%	Nominal mass%	d [%]
Pd/Al_2O_3	Pd	1.16	1.99	-42
$Pd-Ag/Al_2O_3$	Pd	0.80	1.50	-47
	Ag	0.28	0.50	-44

All analyses indicated presence of K in addition to the elements Fe, S, and Ca. Fe, S, and Ca was found to disappear in between analyses of the same pellet which suggested that this was a result of the instrument precision. Amounts of K occurred for all samples and were found to be more significant. However, the amount of K seem to be consistent throughout all analyses, independent of catalyst. Thus, there is a possibility that it emerges from instrument impurities or for example, from the binder, boric acid. The latter could be further investigated

by running a XRF analysis of the binder separately. Amounts of K can be viewed in Table B.1 in Appendix B.1, which is an extended table of all XRF analyses.

XRF analyses confirmed the presence of Pd in Pd/Al_2O_3 and Pd and Ag in $Pd-Ag/Al_2O_3$. However, significant deviations from the nominal mass percentages were obtained for both catalysts. The measured mass percentage of Pd deviated from the nominal mass percentage with -42% for Pd/Al_2O_3. For $Pd-Ag/Al_2O_3$, the measured amount of palladium and silver deviated by -47% and -44% respectively. In XRF analysis there can be several sources of error. First of all, the precision is highly dependent on the sample preparation where a high degree of homogeneity within the sample is necessary for accurate results. The reproducibility of the sample preparation procedure was thus investigated by making two pellets of Pd/Al_2O_3. Standard deviation was used as a measure of the accuracy of the sample preparation. The standard deviation presented in Table B.3 in Appendix B.1 indicates that the accuracy of the sample preparation procedure is acceptable. Another source of error can be attributed to the catalyst synthesis during the impregnation step. A non-homogeneously deposition of the metals may lead to an uneven distribution of palladium and silver within the catalysts. Consequently, the samples used for XRF analysis can retain different amounts of metals. For example, STEM images (Section 4.1.4) of $Pd-Ag/Al_2O_3$ showed that silver was enriched in regions with many small particles, but not found within regions of palladium clusters. As observed in Table B.3, there seem to be variations in the measured mass% of palladium. This might also be a result of systematic errors, which are highly dependent on accurate knowledge of the composition of the reference materials and correction of matrix effects [44]. In addition, it should be mentioned that XRF is not a quantitative technique with high precision, and is more suitable to find approximate levels of the metals.

The Ag/Pd ratio of 0.35 and 0.32 in Table B.1 seem to be in accordance with the expected Ag/Pd = 0.33, despite that the mass% of Pd and Ag deviates from the nominal mass%.

4.1.2   X-ray Diffraction

Figure 4.1 presents the X-ray diffractograms of the support material, γ-Al_2O_3 (green) and synthetized catalysts, Pd/Al_2O_3 (red) and $Pd-Ag/Al_2O_3$ (blue). In addition, analyses over spent catalysts with dilutant, SiC, was performed. As only the phases of SiC was detected, they are not taken into consideration, but can be viewed in Figure B.2 in Appendix B.2.

The diffraction peaks associated with phases in γ-Al_2O_3, PdO, Pd, AgO and Ag (s, ○, ☆, □, and ◯, respectively) in the X-ray diffractogram

are presented in Figure 4.1. The phases were found by the DIFFRAC EVA software database. The alumina was calcined at a maximum temperature of 600 °C, suggesting that the structure of alumina should be maintained as γ-Al$_2$O$_3$. This was confirmed by XRD as only the semi-amorphous, γ-Al$_2$O$_3$ phase, was detected. For the palladium-based catalysts, diffraction peaks are displayed for palladium in its oxide state at approximately $2\theta = 33$, 55, and 71. The TEM results showed that both crystalline and amorphous phases of PdO exist, where the latter one is likely not detected by XRD.

The XRD pattern of Pd-Ag/Al$_2$O$_3$ did not display any crystalline metal or oxide phases of silver that could correspond to the addition of silver to the catalyst. The same features were also observed by Persson et al. (2005, [6]) where no metal oxide phases for silver were displayed in the XRD pattern. However, silver was identified by XRF analysis, indicating that the phase of silver is in a state that is not detected in XRD. This result can demonstrate two things. First, the silver particles are too small. Second, the amount of silver is below the detection limit of XRD. STEM confirmed that silver and palladium were found in regions enriched by small particles. In addition, no single silver particles were found which is in contrast to palladium oxide that was found as single particles too. In addition, the amount of palladium in the catalyst is larger than of silver. This may explain why only phases of palladium oxide are detected.
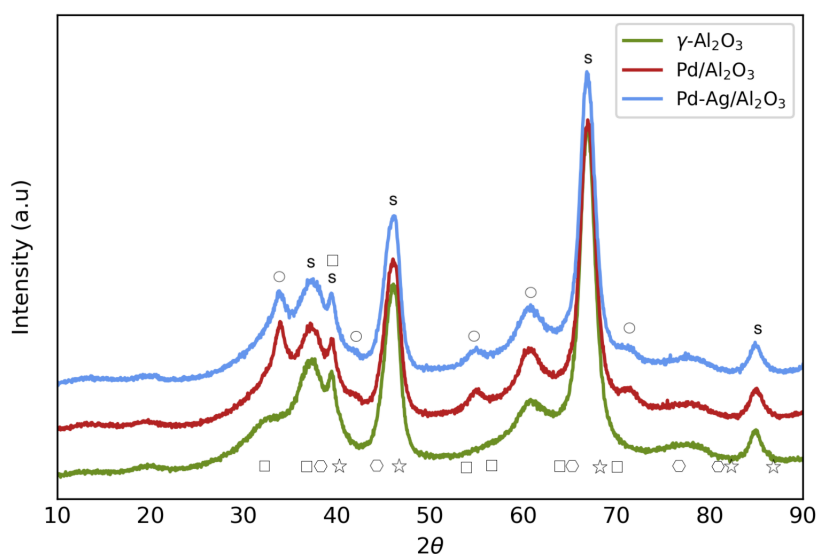
Figure 4.1: The X-ray diffractogram of γ-Al$_2$O$_3$ (green), Pd/Al$_2$O$_3$ (red) and Pd-Ag/Al$_2$O$_3$ (blue). The phases of γ-Al$_2$O$_3$, PdO, Pd, AgO and Ag are indicated by, $\bigcirc$, $\stackrel{\star}{\star}$, $\square$, and $\bigcirc$, respectively.

Crystallite sizes were estimated according to the Scherrer-equation (Equation (4)) by the DIFFRAC EVA software. The software uses K = 0.89 and an instrumental peak width, β = 0.05 Å. The crystallite sizes for the PdO phase are presented in Table 4.2. For Pd/Al$_2$O$_3$ the mean crystallite sizes for PdO-phase was found in the range of 6-12 nm and for Pd-Ag/Al$_2$O$_3$ in range of 6-9 nm. As observed in the X-ray diffractograms, the signals of γ-Al$_2$O$_3$ and PdO overlap which introduces uncertainty of these values.

Table 4.2: Crystallite sizes of PdO estimated by the DIFFRAC EVA software according to Scherrer equation given in Equation (4).

Material	2θ	Size of crystallite [nm]
Pd/Al$_2$O$_3$	33.681	7.6
	54.593	6.1
	71.303	12.4
Pd-Ag/Al$_2$O$_3$	33.777	6.5
	54.975	8.6

Figure 4.2 compares the X-ray diffractograms of fresh and spent Pd-Ag/Al$_2$O$_3$. In general, similar features are observed for both the fresh and spent catalysts, but with slightly larger crystallite sizes after time on stream. From STEM images, no signs of sintering or change in morphology is observed after time on stream. Thus, the increase in crystallite sizes might be a result of improved ordering. The crystallite sizes estimated by DIFFRAC EVA software are listed in Table 4.3.

Different sample holders were used for the XRD-analyses of fresh and spent Pd-Ag/Al$_2$O$_3$ due to the limited amount of spent speciment. Hence, the signal for fresh Pd-Ag/Al$_2$O$_3$ in Figure 4.1 and Figure 4.2 may deviate to some extent.
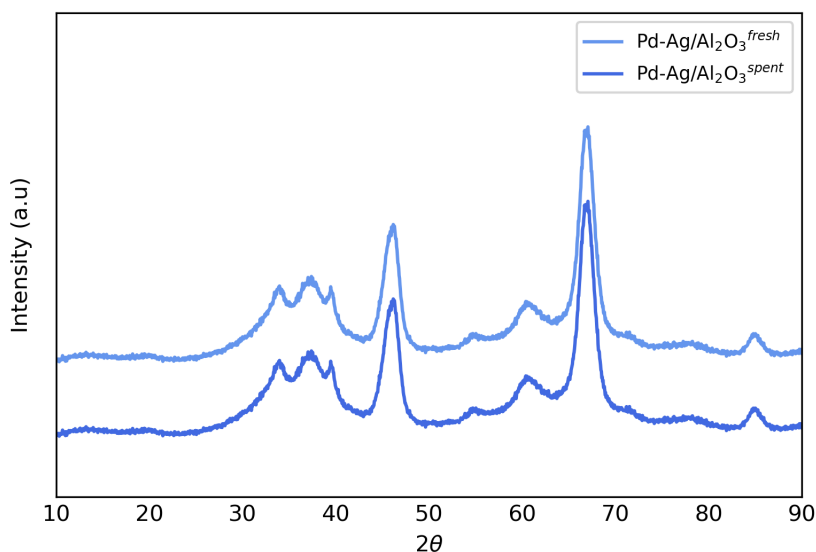
Figure 4.2: The X-ray diffractograms of fresh and spent Pd-Ag/Al$_2$O$_3$.

Table 4.3: Crystallite sizes estimated by the DIFFRAC EVA software according to Scherrer equation given in Equation (4).

Material	2θ	Size of crystallite [nm]
Pd-Ag/Al$_2$O$_3$^{fresh}	33.962	4.9
	54.601	8.3
Pd-Ag/Al$_2$O$_3$^{spent}	33.709	10.5
	54.911	11.6

4.1.3 N$_2$ Physisorption

The results from N$_2$ physisorption are listed in Table 4.4, where S$_{BET}$ is the computed specific surface area by application of the BET method, V$_p$ is the BJH Desorption cumulative pore volume and the average pore diameter is the BJH Desorption average pore diameter. The N$_2$ physisorption analysis was repeated for Pd-Ag/Al$_2$O$_3$.

Table 4.4: The results obtained from N$_2$ physisorption analysis of the materials. S$_{BET}$ is the specific surface area obtainted by the BET method, V$_p$ is the BJH Adsorption cumulative pore volume and the average pore diameter is the BJH Adsorption average pore diameter. [12] indicates first and second analysis, respectively.

Catalyst	S$_{BET}$ [m^2 g^{-1}]	V$_p$ [cm^3 g^{-1}]	Average pore diameter [nm]
Pd/Al$_2$O$_3$	182	0.54	10.3
Pd-Ag/Al$_2$O$_3$^{1}	180	0.54	10.3
Pd-Ag/Al$_2$O$_3$^{2}	180	0.53	10.3
γ-Al$_2$O$_3$	190	0.58	10.3

[1] first analysis.
[2] second analysis.

According to the results in Table 4.4, a slight decrease in surface area is observed when impregnating Pd and Ag on Al_2O_3. However, the difference in surface area between the catalysts is small and the addition of palladium and silver seems to have a minor effect on the pore volume and the surface area.

The average pore diameter of approximately 10 nm was reported for all analyses. Thus it is within the mesopore size range (2-50 nm, [20]). This is also confirmed by the N_2 adsorption-desorption isotherms, yielding a narrow distribution of mesopores. The N_2 adsorption-desorption isotherm and the pore size distribution of Pd-Ag/Al_2O_3 is shown in Figure 4.3. For the respective materials, see Figure B.3-B.5 in Appendix B.3.

(a) N_2 adsorption-desorption.   **(b)** Pore size distribution.
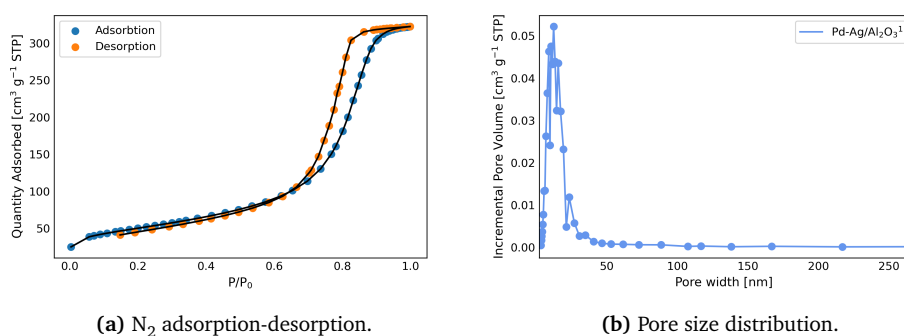
Figure 4.3: N_2 adsorption-desorption isotherm **(a)** and pore size distribution **(b)** of Pd-Ag/Al_2O_3.

4.1.4 Transmission Electron Microscopy

The morphological study of the catalysts by TEM and STEM is presented in Figures 4.4-4.7. Based on the obtained XRD results presented in Section 4.1.2, palladium is assumed to be in its oxide state, PdO, when presenting the results in the following section.

Figure 4.4 shows a fragment of the catalyst material of Pd/Al_2O_3. Overall, the palladium particles seem to be well distributed on the support. They were found as both single crystallites and as clusters of several palladium particles. In addition, amorphous palladium oxide particles are observed. From STEM images, shown in Figure 4.4, a widespread of particle sizes were found and ranging in particular from 2-5 nm. As shown in Figure 4.4(a), the palladium is surrounded by amorphous γ-Al_2O_3(light-grey matrix). γ-Al_2O_3 was found as long particles forming large agglomerates where white particles corresponding to palladium are observed.

(a) STEM HAADF image   (b) STEM HAADF image
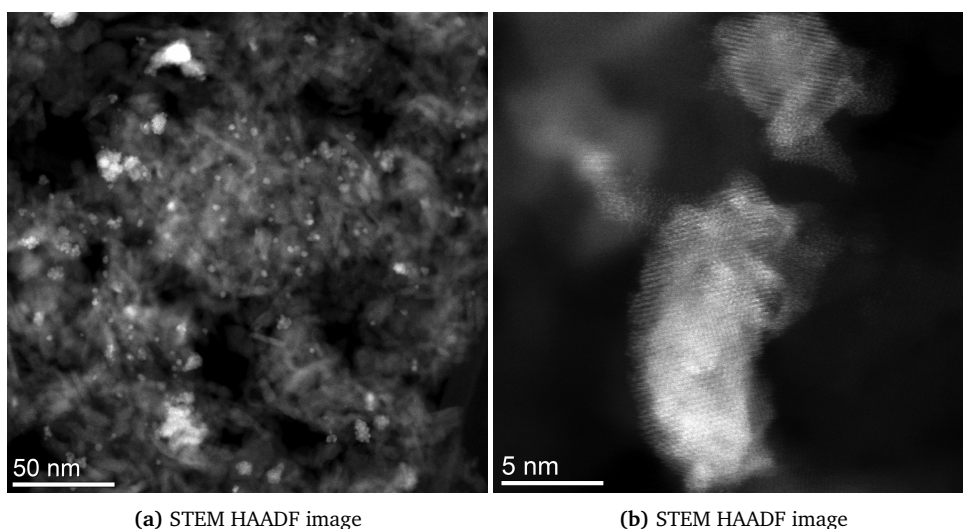
Figure 4.4: STEM HAADF image of fresh Pd/Al$_2$O$_3$

TEM images of Pd-Ag/Al$_2$O$_3$ are shown in Figure 4.5(**a**, **b**), where black spots of particles are observed. Also here, clusters of several particles are observed and with a large spread of particle sizes. Moreover, Figure 4.5(**c**, **d**) shows STEM images of fresh Pd-Ag/Al$_2$O$_3$. A majority of the particle sizes were found to range between 2-4 nm, with the largest ones up to 5 nm. Energy-dispersive spectroscopy (EDS) in STEM mode was used for elemental analysis of the bimetallic catalyst. Separating the elements turned out to be quite complicated because of overlapping EDS spectrums of palladium and silver. By using reference EDS spectrums of palladium- and silver, it was to some extent, possible to estimate the silver content by the symmetry of the spectrums. The reference spectrum is presented in Figure B.6 in Appendix B.4.

EDS indicated an enhancement of silver content within regions with many small particles (Figure 4.7(**b**)). For this spot measurement, the silver content was estimated to 18% and palladium to 82%, closer to the nominal mass% than the presented results of XRF analyses. Figure 4.6(**a**) shows a large cluster of particles, which by EDS was determined to consist predominantly of palladium. In addition, no single silver particles were found, which can indicate that silver forms alloys with palladium. This is contrary to the findings of Persson *et al.* (2005, [6]) which found silver enriched near the PdO particles and in addition as separate particles. As palladium particles were found separately, it is suggested that there is a co-existence of single palladium particles and alloyed palladium-silver particles.

(a) TEM BF image

(b) TEM BF image

(c) STEM HAADF image

(d) STEM HAADF image

(e) STEM HAADF image
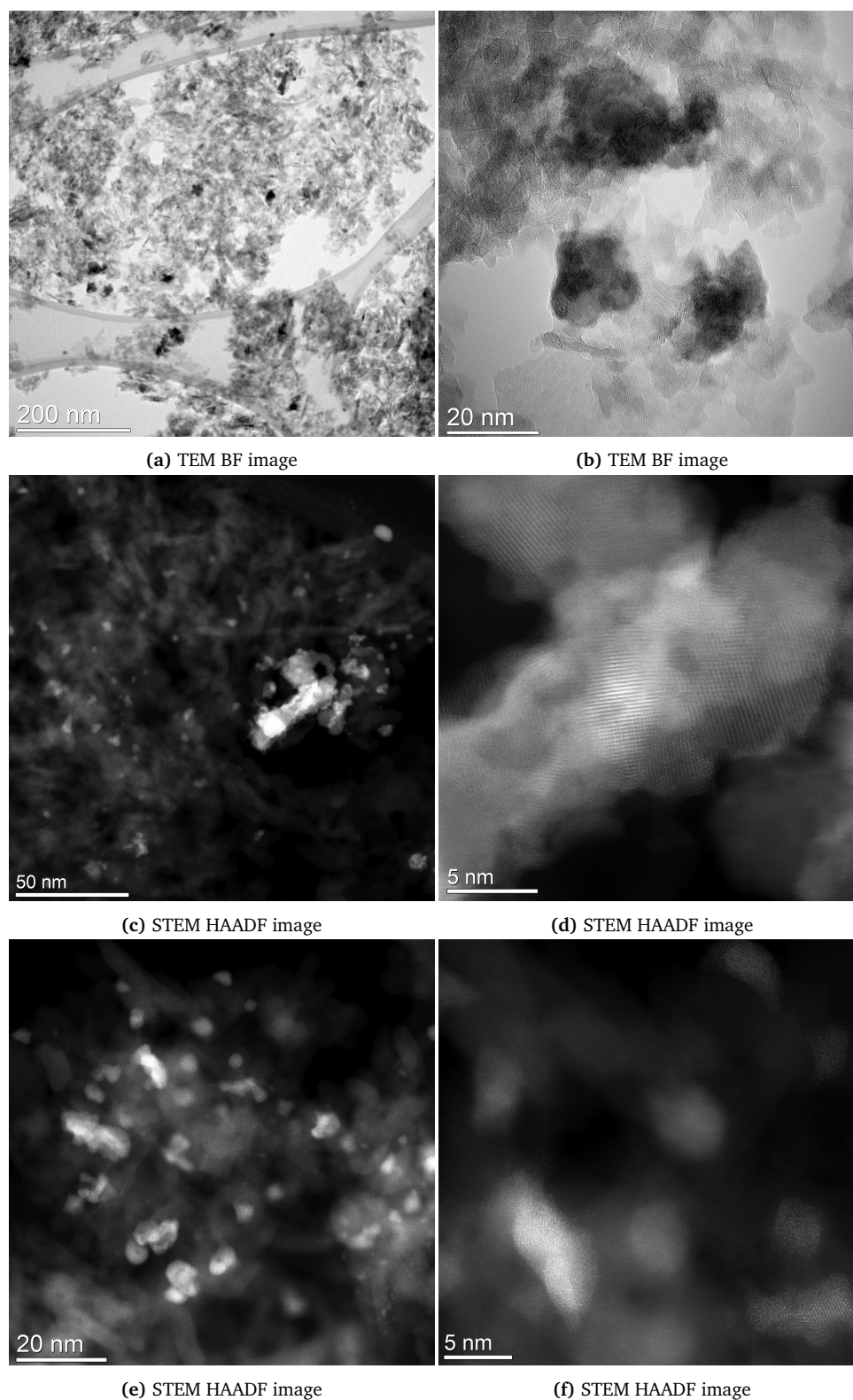
(f) STEM HAADF image

Figure 4.5: TEM images of fresh Pd-Ag/Al$_2$O$_3$ and STEM images of fresh (**c,d**) and spent (**e,f**) Pd-Ag/Al$_2$O$_3$.
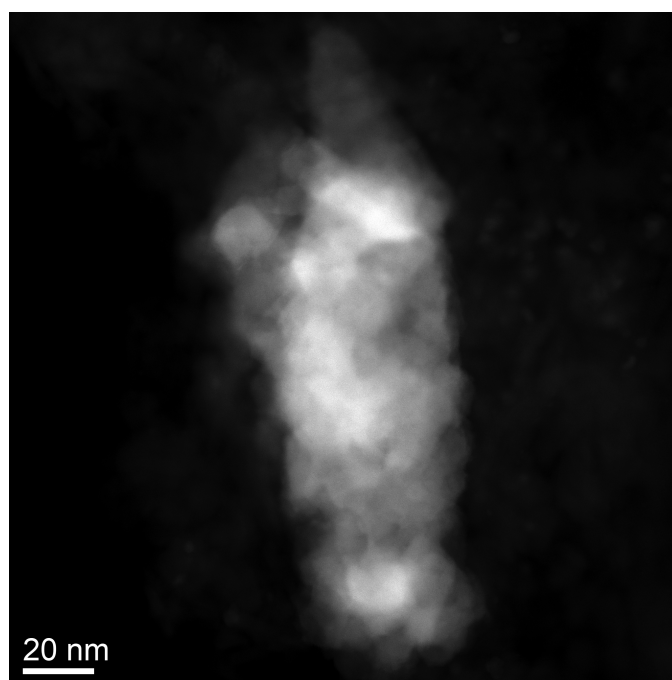
(a) STEM HAADF image of large cluster of particles
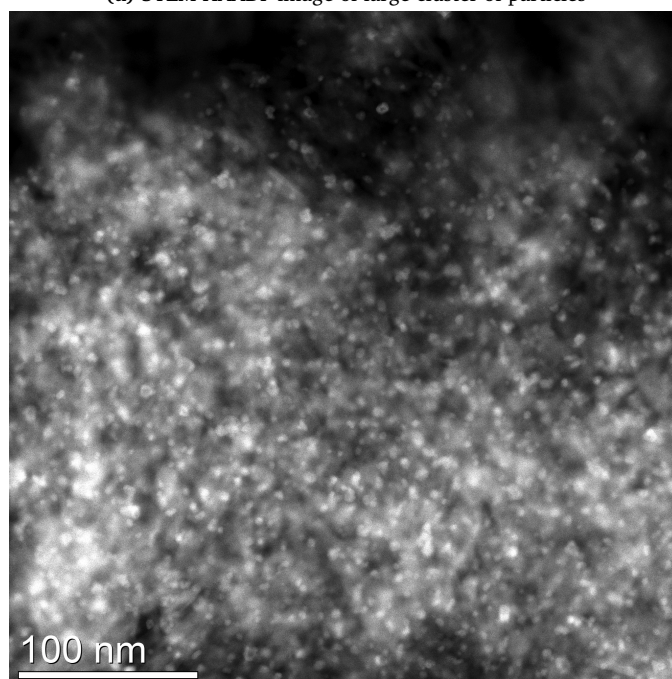
(b) STEM HAADF image of region enriched with small particles

Figure 4.6: STEM HAADF images of spent Pd-Ag/Al$_2$O$_3$.
Corresponding EDS spectrum are presented in Figure 4.7.

(a) EDS spectrum of cluster of particles

(b) EDS spectrum of region enriched with small particles
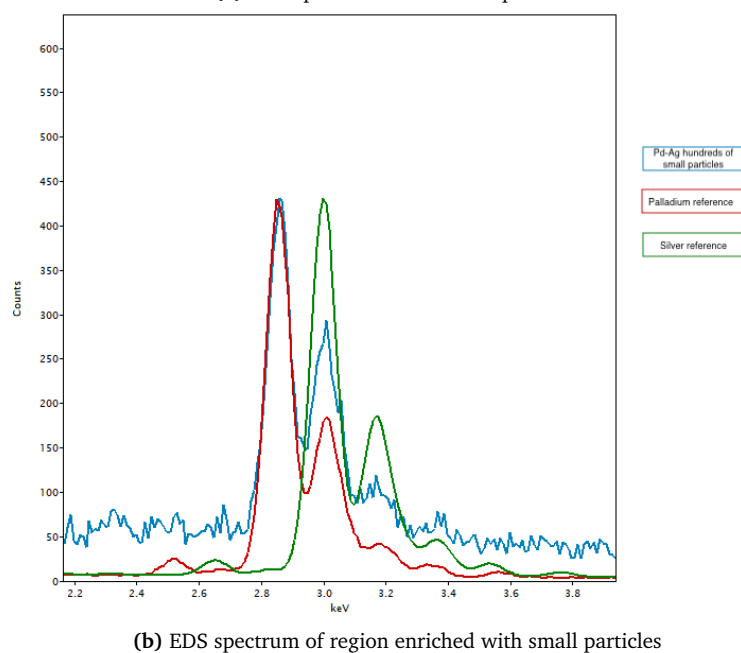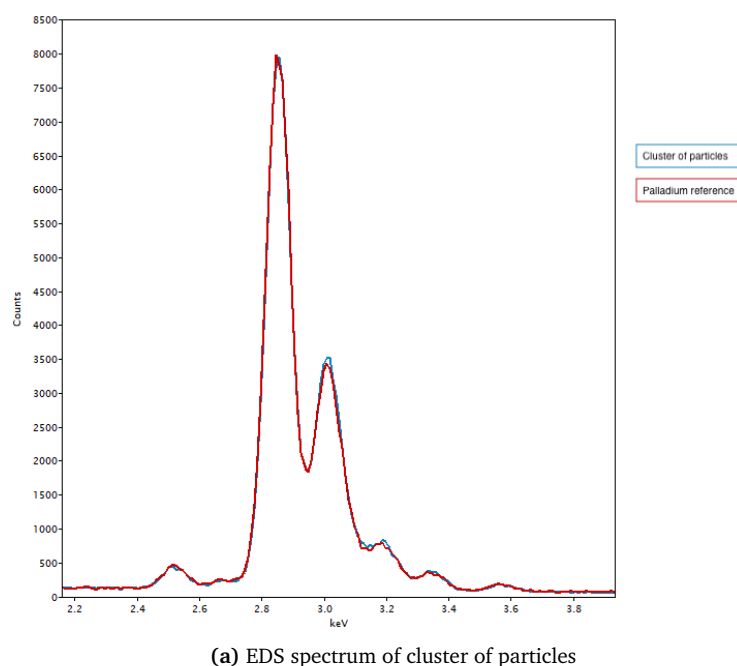
Figure 4.7: EDS spectrum of large cluster of particles (Figure 4.6(a)) and region enriched with small particles (Figure 4.6(b)).The red curve is representative of the palladium reference, the green of the silver reference and the blue is the spectrum obtained from from the images.

Figure 4.5 shows STEM images of fresh (**c,d**) and spent (**e,f**) Pd-Ag/Al_2O_3. The spent catalyst was tested in a long-term experiment of CO oxidation and with reaction conditions presented in Table 3.12 in Section 3.4.2. The images displayed similar features of the fresh and spent catalysts, and no indication of sintering after several hours

on stream (60 h). To summarize, both catalysts exhibit high dispersion with the majority of the particles in the size range of 2-5 nm. No single silver particles were found, but EDS revealed enrichment of silver in regions of many small particles. The clusters consisted predominantly of palladium particles.

4.1.5 Chemisorption

The results from CO chemisorption analysis of the catalysts are presented in Table 4.5. CO was chosen as adsorption gas was to avoid palladium hydride formation [39]. The quantity adsorbed CO was obtained by two isotherms, as explained in Section 2.3.5, where the difference between them represented the chemisorbed amount used for calculation of the dispersion. For the bimetallic system, the measured uptake was directly related to CO chemisorbed on Pd as CO is not chemisorbed by Ag [48]. The obtained instrument values are presented in Table B.5 in Appendix B.5. The quantity adsorbed was used to calculate the dispersion, specific metal surface area, and crystallite size according to Equation (9)-(12).

The general trend is high dispersion for both catalysts. From the results, it is observed that the CO uptake is reduced for the bimetallic catalyst. It is reported that the surface composition might change upon contact with adsorbate [63]. The segregation dynamics of Pd-Ag is studied by several authors [64, 65, 14, 5]. For example, Bouwman, Lippits, and Sachtler (1971, [64]) reported that the Pd-Ag alloy surface became enriched with Pd upon prolonged contact with CO. Since Pd has a higher surface energy [66] and smaller atomic radius than Ag, chemisorbed species will bind to Pd and can cause segregation of Pd to the surface [64, 67, 68, 63, 5]. On the other hand, Karski *et al.* (2005, [65]) reported a decrease amount of chemisorbed CO upon the addition of silver and attributed this to the enrichment of silver at the surface. Hence, depending on the conditions, the surface may be enriched by one of the components. For this thesis, the quantity of adsorbed CO is reduced by approximately 30%. Since the crystallite sizes are close in value and in agreement with TEM and STEM (Section 4.1.4), this can insinuate alloy formation of Pd and Ag, and that the reduction in uptake might be related to the lower loading of Pd in Pd-Ag/Al_2O_3.

Table 4.5: The dispersion, metal surface area, crystallite size and quantity adsorbed CO measured by CO chemisorption. The analysis conditions are listed in Table 3.6.

Catalyst	Dispersion [%]	Specific metal surface area [m2/g metal]	Crystallite Size [nm]	Quantity adsorbed [cm^3/g STP]
Pd/Al_2O_3	37	165	3.04	0.7777
Pd-Ag/Al_2O_3	34	153	3.26	0.5434

4.1.6 Temperature Programmed Reduction

Temperature-programmed reduction (TPR) was used to study the reducibility of the catalysts. The results are presented in Figure 4.8, and separate TPR profiles can be reviewed in Appendix B.6. For both catalysts, the presence of a negative peak is observed at approximately 82-94 ° C. This peak may be attributed to the desorption of weakly adsorbed hydrogen and decomposition of the β-PdH phase forming at low temperatures by the dissolution of hydrogen in Pd [69, 70]. The reduction of PdO is well studied and it is known to be reducible at low temperatures, even at room temperature. Aznárez *et al.* (2015, [70]) reported that the negative peak got more pronounced when increasing the metal loading of palladium. This also seem to be the trend in Figure 4.8, where the negative peak is more pronounced for Pd/Al$_2$O$_3$ containing 2 mass% palladium compared with Pd-Ag/Al$_2$O$_3$ containing 1.5 mass% palladium. No hydrogen adsorption peaks at increased temperature were observed for any of the catalysts, suggesting that the reduction of PdO and possible Pd-Ag mixed system took place at a lower temperature than 50 °C [65]. In addition, these findings provide evidence for that there is no silver in its oxide form, which is stable up to approximately 250 °C. This is consistent with the fact that the catalysts were calcined at 500 °C.
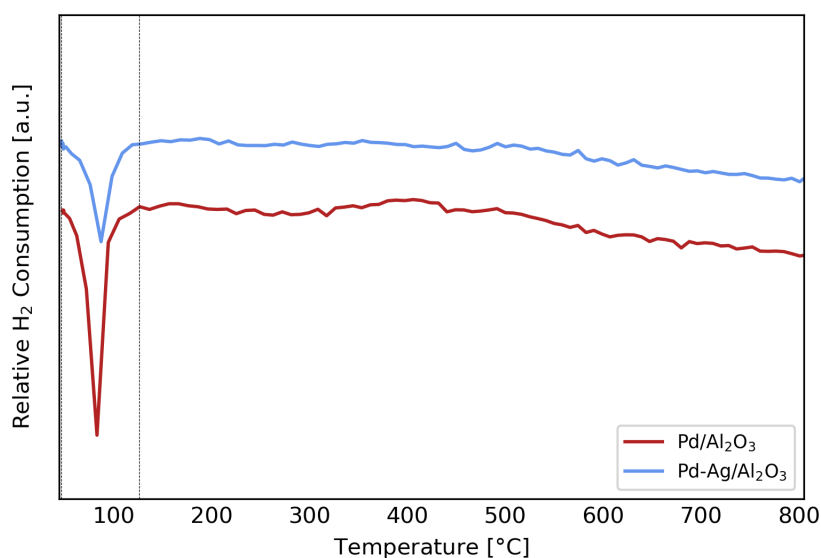
Figure 4.8: H$_2$-TPR profile of Pd/Al$_2$O$_3$ and Pd-Ag/Al$_2$O$_3$. The vertical line at approximately 125 °C indicates where the area of the negative peak was calculated.

An important question associated with this is whether the decomposition of the β-PdH phase is purely determined by the palladium content in the catalyst or if the addition of silver has an influence too.

This was investigated by calculating the area of the negative peaks for both catalysts. The area was found using a trapezoidal numerical integration in Python. The region of where the area was calculated is indicated by a vertical line in Figure 4.8. If the difference in the area was approximately 25%, a reasonable explanation for the smaller negative peak in the TPR analysis of Pd-Ag/Al_2O_3 could be attributed to the loss of palladium content. As presented in Figure 4.9, the area of the negative peak in Pd/Al_2O_3 is approximately 46 % larger than for Pd-Ag/Al_2O_3, indicating that the presence of silver may have an inhibiting effect on the β-PdH phase formation [65]. The same feature was observed by Karski *et al.* (2005, [65]) which reported a less intensive negative peak for a 5% Pd - 1% Ag/SiO_2 system compared with 5% Pd/SiO_2. As explained in Section 2.3.6, the hydrogen solubility increases for Pd-Ag alloy compared with pure Pd as a result of expanded lattice sizes. This implies that less hydrogen will be released at increased temperatures for the bimetallic catalyst, and, thus, a less intensive peak may be observed upon alloy formation.
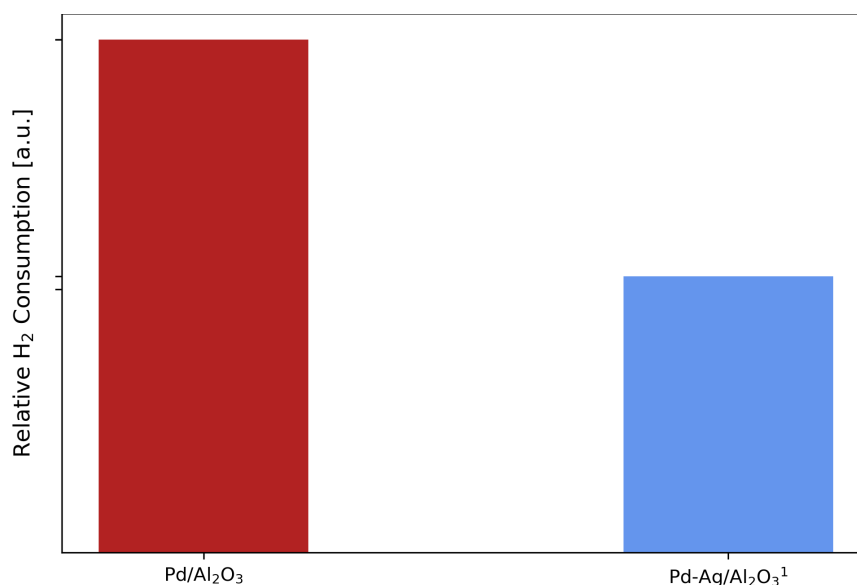
Figure 4.9: A comparison of the areas was calculated of the negative peaks in TPR analysis of Pd/Al_2O_3(red) and Pd-Ag/Al_2O_3(blue). The areas was found using trapezoidal numerical integration in Python.

Two TPR measurements was performed over Pd-Ag/Al_2O_3 and the area was found and compared for all analyses. This can be reviewed in Figure B.8 in Appendix B.6. The second analysis of Pd-Ag/Al_2O_3 had a slightly lower area than the first analysis, and with a deviation of 5%. For the second analysis of Pd-Ag/Al_2O_3, the area of the negative peak was approximately 49% smaller than of the negative peak in the TPR-profile of Pd/Al_2O_3.

4.2 Catalytic Activity

The obtained results from catalyst testing in CH_4 oxidation and CO oxidation will in the following sections be presented and discussed, with each of their subsections. They will be evaluated with different aspects and in correspondence with the investigated parameters. The experimental procedure for catalyst testing is described in Section 3.4.

An illustrative plot of CH_4 conversion as a function of temperature is shown in Figure 4.10. The conversion data is obtained from the μ-GC which carried out measurements every 6th minute. The conversion was calculated according to Equation (23). The temperature was measured from the thermocouple placed in the middle of the catalyst bed and coordinated with the log from the μ-GC. As earlier mentioned, the temperature was held constant for 30 minutes every 25 °C. The conversion was calculated at the last data point from the μ-GC of each temperature dwell, to ensure that the conversion was calculated at a stable temperature. The conversion was calculated according to Equation (23).
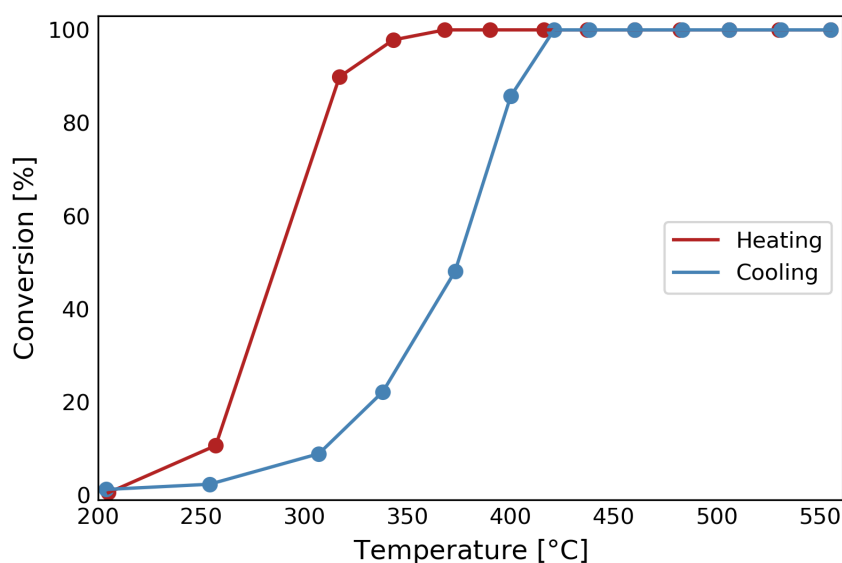
Figure 4.10: The first reaction cycle of Pd/Al_2O_3 in methane oxidation, where the conversion is plotted against the temperature. The reaction conditions was 4 ml min^{-1} CH_4, 95.25 ml min^{-1} O_2 and 100.75 ml min^{-1} N_2.

The reaction cycles were repeated several times for each of the catalysts in both reactions. For all reaction cycles, the carbon balance for the system was calculated. The carbon balance was calculated according to Equation (26) using data obtained from the μ-GC that detected the species CH_4, CO, CO_2 and N_2. For further investigation, the carbon

balance was plotted against the conversion of CH_4/CO. An example of this is illustrated in Figure 4.11. The general trend is that the carbon balance deviation is small for all runs compared with previous work [12, 13] and might be within acceptable limits. The standard deviation of the carbon balance is presented in Table C.2 and Table C.4 for CH_4 and CO oxidation, respectively. For CH_4 oxidation, no other carbon species than CH_4 and CO_2 was detected. The respective plots for all reaction cycles can be reviewed in Appendix C.2.2 and Appendix C.3.2 for CH_4 and CO oxidation, respectively.
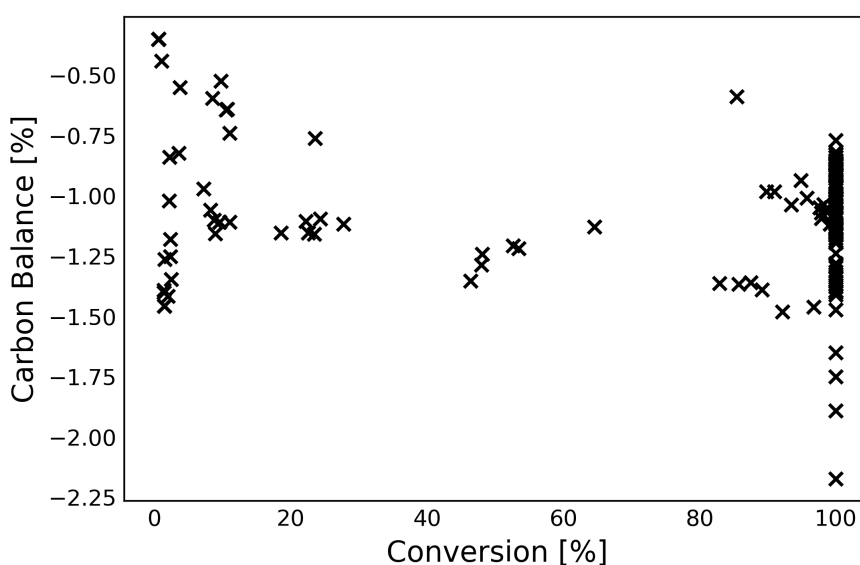
Figure 4.11: An illustration of the carbon balance deviation plotted against the conversion of methane in the first reaction cycle over Pd/Al_2O_3. The reaction conditions was 4 ml min^{-1} CH_4, 95.25 ml min^{-1} O_2 and 100.75 ml min^{-1} N_2.

Polynomial regression in Python was used to fit the conversion curve. The curve was modeled as a 5th-degree polynomial. From this, the temperatures needed to obtain 10-100% conversion of CH_4/CO could be found. The corresponding temperatures to these levels of conversion are listed in Table C.1 for CH_4 oxidation and Table C.3 for CO oxidation. The python script is presented in Appendix D.

Conversion levels of 10-50% and 20-50% for CH_4 and CO oxidation respectively were used for Arrhenius plots. The necessary temperatures for these levels of conversion were found using the python script. Further, the activation energy was found interpreting a trend line of the points in the Arrhenius plot. From the relation of the slope of the line being equal to -E_a/R, as presented in Section 2.5.4, the activation energy was found by multiplying this value with the negative gas constant, -R. The Arrhenius plot for the first reaction cycle

in CH_4 oxidation over Pd/Al_2O_3 is presented in Figure 2.7. Here, the activation energy was found to be 141 $kJmol^{-1}$. The respective plots for all reaction cycles can be viewed in Appendix C.2.1 and Appendix C.3.1.
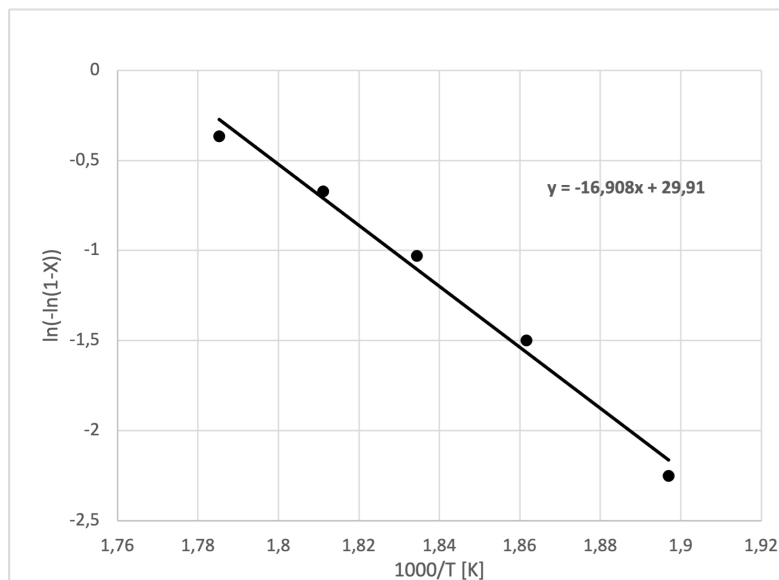
Figure 4.12: The Arrhenius plot used for computation of the activation energy of methane in the first reaction cycle over Pd/Al_2O_3. The slope of the line is euqal to $-E_a/R$ and is used to find the activation energy, E_a, by multiplying this value by the negative gas constant, $-R$. This yields an activation energy of 141 $kJ\,mol^{-1}$. The reaction conditions was 4 ml min^{-1} CH_4, 95.25 ml min^{-1} O_2 and 100.75 ml min^{-1} N_2.

4.2.1 Methane Oxidation

In the following sections, the catalytic activity measurements of Pd/Al_2O_3 and Pd-Ag/Al_2O_3 in CH_4 oxidation will be presented and discussed. Both materials were found to exhibit catalytic activity in low-temperature oxidation of methane.

An assumption of first-order in methane and zero-order in oxygen was assumed for calculations of reaction rates and apparent activation energies. This was considered valid when operating under lean conditions [3, 71].

The experiments were checked for reproducibility by comparing experiments under identical conditions. Figure 4.13 compares the first reaction cycle over fresh Pd/Al_2O_3 (Figure 4.10) with the reaction cycle performed before the wet experiment (Figure 4.18). For these two experiments the reaction conditions was the same: 4 ml min^{-1} CH_4, 95.25 ml min^{-1} O_2 and 100.75 ml min^{-1} N_2. The results suggest good reproducibility of the experimental procedure. In addition, a blank test for the reactor and inert was performed. The result from

the blank test is shown in Figure C.8 in Appendix C.4, with a maximum conversion of 2.5% at 550°C.
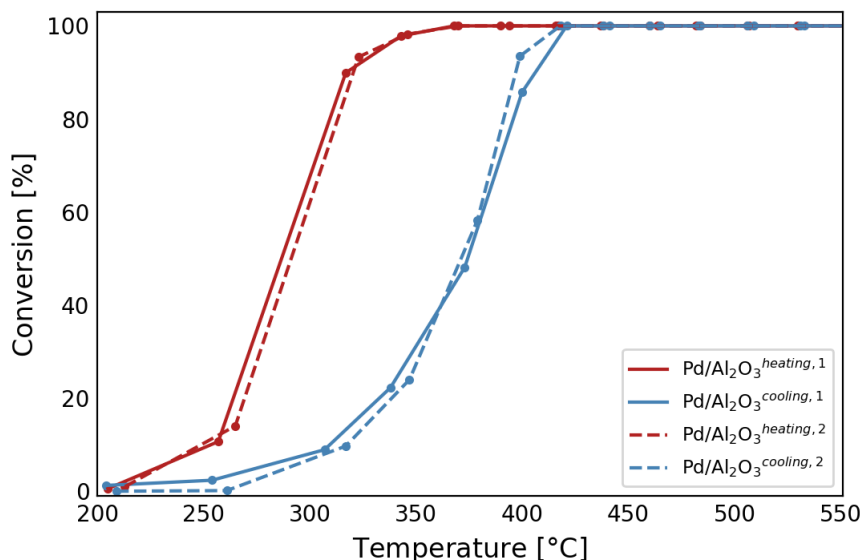
Figure 4.13: The conversion of methane over two samples of fresh Pd/Al_2O_3. The reaction conditions was 4 ml min^{-1} CH_4, 95.25 ml min^{-1} O_2 and 100.75 ml min^{-1} N_2.

Figure 4.14 shows the behavior of the ignition and extinction of CH_4 oxidation over Pd/Al_2O_3 during three reaction cycles. Pd/Al_2O_3 exhibits an ignition-extinction hysteresis of reversed nature, with lower conversions during the extinction curve. The decomposition of PdO to Pd at high temperatures is extensively studied and normally used to explain the hysteresis effect of the heating and cooling curve of methane oxidation [3]. However, since the maximum temperature of the experiments performed in this thesis is much lower than the decomposition temperature of PdO (approximately 800-850 °C, depending on the support, [3]) this can be ruled out as the explanation for the hysteresis effect. Also, Gélin *et al.* (2002, [3]) reported that PdO is in thermodynamically stable phase in the temperature range 300° C - 600 ° C, i.e. the same temperature range as for the experiments. An interesting feature was reported by Carlsson and Skoglundh (2011, [1]) who studied the low-temperature oxidation of methane and CO over platinum-based catalysts. They reported that the platinum surface was partially reduced by methane dissociation products. Assuming that this can be true for palladium-based catalyst also, this would mean that the PdO phase, which is regarded as the main active phase, is partially reduced during the cooling curve. Su, Carstens and Bell (1998, [72]) reported that CH_4 reduces PdO, and whether its surface PdO, subsurface PdO or bulk PdO that reduces, depends on the condi-

tions. There are, however, several parameters that will effect the catalytic behavior, some of them being metal dispersion, pre-treatment and reaction mixture [3]. But still, the nature of the active sites under such conditions remains somewhat unclear, and more experimental work is required to completely understand the mechanisms of the hysteresis.

Several assumptions and limitations should be accounted for in the upcoming sections. First of all, the temperatures needed for certain levels of conversion were found by a polynomial fitting. Therefore, they may not be fully representative of the real conversion curve but used as an estimation. Further, the presence of possible temperature gradients over the catalyst bed was not investigated. Slightly higher temperatures than the maximum set-point temperature were observed for all runs even though using the same feed concentrations and the same temperature program. This can be attributed to the exothermic behavior of the reaction which may cause a temperature gradient, either in the catalyst bed or inside the catalyst particles [20]. However, isothermal conditions are hard to achieve under such reaction conditions, even though certain standard measures were conducted before every round of catalyst testing. Even small temperature deviations can influence the catalytic activity strongly, and, thus, this must be taken into consideration upon evaluation of, for example, Arrhenius plots.

As presented in Table 4.6 the ignition and extinction processes are shifted towards higher temperatures after several reaction cycles. This suggests that the hysteresis also changes as a function of reaction cycle number, even when the reaction conditions remain the same. Hence, repetitive reaction cycles can reveal important matters regarding catalyst stability. From the 1st reaction cycle to 2nd and 3rd, the temperatures required to reach T_{10}-T_{100} increases in a systematic manner as shown in Table 4.6, where also the apparent activation energy and reaction rate at 300 ° C are presented. The 1st reaction cycle over Pd/Al$_2$O$_3$ displayed superior activity with 100% conversion reached at 368 ° C. The gap in activity between the 1st and 2nd reaction cycle is large and the reaction rate decreases by approximately 89%. The difference between the 2nd and 3rd reaction cycle is smaller but still significant, with a decrease of approximately 50%. This indicates that the catalyst undergoes some deactivation. Alternatively, it could mean that the atoms find more thermodynamically stable positions. An initial dip in activity is often observed when a catalyst is tested for the first time [39]. Since the loss of activity is smaller for the subsequent reaction cycles, this is not an unlikely explanation.

From the discussed assumption above of a reducing reactant mixture, this would imply that the initial state of the 2nd and 3rd reaction cycle is a partially reduced state of PdO, and consequently the ignition

and extinction processes are shifted towards higher temperatures. It should be noted that the reaction rate was calculated at the conversion at 300 ° C for all reaction cycles and with an intended conversion level less than 20%. With superior initial activity during the first reaction cycle, the catalyst exceeded this value with a conversion of 67%. Thus, the values of the reaction rate might be ambiguous. The feature of the lower activity of the cooling curve and subsequent reaction cycles were also reported by Mihai *et al.* (2017,[36]). They examined the influence of water under lean conditions and attributed the lower activity of the cooling curve and subsequent reaction cycles to water produced by the reaction. The deactivation mechanism of PdO is however much scrutinized, and will be discussed in further detail in Section 4.2.1.2 and Section 4.2.1.3.

Table 4.6: The temperatures at 10,50 and 100% conversion of methane over three reaction cycles over Pd/Al_2O_3, the calculated activation energy, E_A, and reaction rate, r, at 300 °C. T_X is from from the heating curve of the cycle, but a table representative of both heating- and cooling curves can be reviewed in Table C.1 in Appendix C.2.

Catalyst	Reaction Cycle	$T_{10\%}$ [°C]	$T_{50\%}$ [°C]	$T_{100\%}$ [°C]	E_A [kJ mol^{-1}]	r [mol h^{-1} g$_{cat}$$^{-1}$]
	1	254	287	368	141	0.036
Pd/Al_2O_3	2	311	374	443	95	0.004
	3	331	400	462	92	0.002

(a) 1$^{\text{st}}$ cycle over Pd/Al$_2$O$_3$.

(b) 2$^{\text{nd}}$ cycle over Pd/Al$_2$O$_3$.

(c) 3$^{\text{rd}}$ cycle over Pd/Al$_2$O$_3$

Figure 4.14: Conversion of methane over Pd/Al$_2$O$_3$ as a function of the temperature for three reaction cycles. The reaction parameters was 4 ml min^{-1} CH$_4$, 95.25 ml min^{-1} O$_2$ and 100.75 ml min^{-1} N$_2$. Red curves represent heating and the blue curves represent the subsequent cooling.

Three reaction cycles over fresh $Pd-Ag/Al_2O_3$ are illustrated in Figure 4.15. The reversed hysteresis is also observed for $Pd-Ag/Al_2O_3$, but the change as function of reaction cycles is not as pronounced as for Pd/Al_2O_3. As previously mentioned, hysteresis can be caused by several factors, such as the exothermicity of the reaction [71]. However, the fact that the oxidation state of $Pd-Ag/Al_2O_3$ is unknown, and few hysteresis studies are found for methane oxidation over this catalyst, makes it difficult to establish the mechanism.

Table 4.7 presents the temperatures needed for 10,50 and 100% level of conversion, the activation energy, and the reaction rate calculated at 300 ° C. As observed, the temperatures needed for 10,50 and 100% conversion increases in a systematic order, with increasing temperatures with increasing reaction cycles. In addition, the reaction rate at 300 ° C decreases. There is, however, no systematic trend for the apparent activation energy. As previously mentioned, a polynomial fitting of the conversion curve was used for the estimation, which may not be completely representative of the real conversion curve. E_A was found in the range of 10-50% conversion and as shown in Figure 4.15 there are few points in this region of the conversion curve. Hence, the experimental procedure should be optimized for more accurate values of the apparent activation energy.

Table 4.7: The temperatures at 10,50 and 100% conversion of methane over three reaction cycles over $Pd-Ag/Al_2O_3$, the calculated activation energy, E_A, and reaction rate, r, at 300 °C.

Catalyst	Reaction Cycle	$T_{10\%}$ [°C]	$T_{50\%}$ [°C]	$T_{100\%}$ [°C]	E_A [kJ mol^{-1}]	r [mol h^{-1} g$_{cat}$$^{-1}$]
	1	264	313	404	98	0.0208
$Pd-Ag/Al_2O_3$	2	271	350	455	66	0.0129
	3	276	365	472	97	0.0097

Figure C.1 and Figure C.2 in Appendix C.2 shows that some of the points diverges from the straight line. This may explain the variations of apparent activation energy during the reaction cycles. When comparing the results to those of other studies of methane oxidation in Table 4.8, it must be pointed out that variations of the apparent activation energy, E_A, is also observed here. For these studies, the apparent activation energy was found to range between 50 and 150 kJ/mol, depending on the reaction conditions and the catalyst.

Table 4.8: Comparison of previous studies of methane oxidation over palladium-based catalysts.

Catalyst	Reactant Mixture	T [°C]	E_A [kJ mol^{-1}]	Ref
7.3% Pd/Al$_2$O$_3$[a]	O$_2$/CH$_4$ = 4	200-320	86	[27]
7.3% Pd/Al$_2$O$_3$[a]	O$_2$/CH$_4$ = 4 + 2% H$_2$O	200-320	151	[27]
1% Pd/Al$_2$O$_3$[b]	O$_2$/CH$_4$ = 1	280-400	72.4	[71]
1% Pd/Al$_2$O$_3$[b]	O$_2$/CH$_4$ = 3	280-400	71.4	[71]
1% Pd/Al$_2$O$_3$ [b]	O$_2$/CH$_4$ = 6	280-400	65.7	[71]
1% Pd-0.34% Ag/Al$_2$O$_3$[b]	O$_2$/CH$_4$ = 1	280-400	69.7	[71]
1% Pd-0.34% Ag/Al$_2$O$_3$[b]	O$_2$/CH$_4$ = 3	280-400	66.3	[71]
1% Pd-0.34% Ag/Al$_2$O$_3$[b]	O$_2$/CH$_4$ = 6	280-400	49.5	[71]
8.5% Pd/Al$_2$O$_3$	2% CH$_4$/O$_2$	277 (550 K)	76	[73]
2.7% Pd/Al$_2$O$_3$	O$_2$/CH$_4$ = 0.6	227-527	84	[74]

[a] Stabilized in 1% CH$_4$ and 4% O$_2$ in He
[b] Pre-reduced
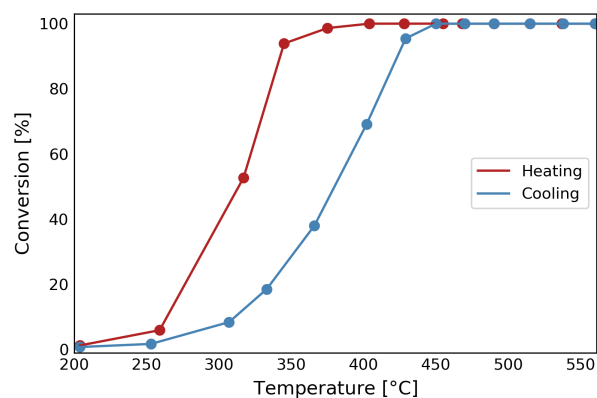
(a) 1st cycle over Pd-Ag/Al$_2$O$_3$.
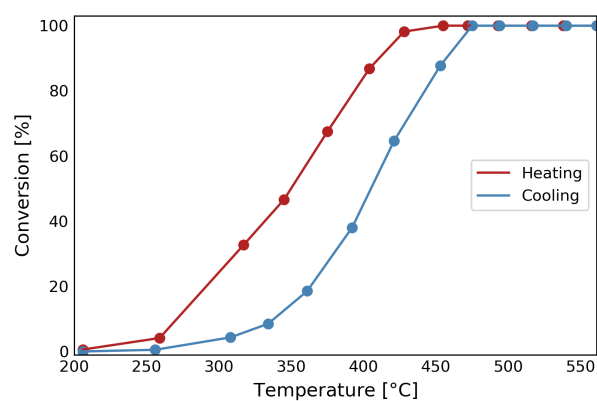
(b) 2nd cycle over Pd-Ag/Al$_2$O$_3$.
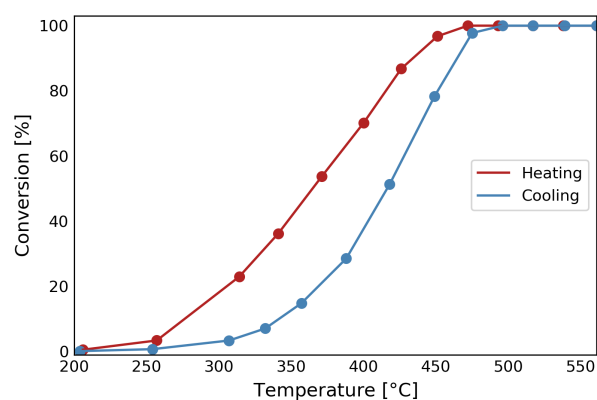
(c) 3rd cycle over Pd-Ag/Al$_2$O$_3$

Figure 4.15: Conversion of methane over Pd-Ag/Al$_2$O$_3$ as a function of the temperature for three reaction cycles. The reaction parameters was 4 ml min^{-1} CH$_4$, 95.25 ml min^{-1} O$_2$ and 100.75 ml min^{-1} N$_2$. Red curves represent heating and the blue curves represent the subsequent cooling.

4.2.1.1 Influence of Silver

This section specifically addresses the effect of replacing a portion (25%) of palladium with silver. The total amount of active material was the same for both catalysts. The conversion of methane as function of the catalyst bed temperature over the two catalysts are shown in Figure 4.16, where (a) is a comparison of the heating curves and (b) the cooling curves for the three reaction cycles.
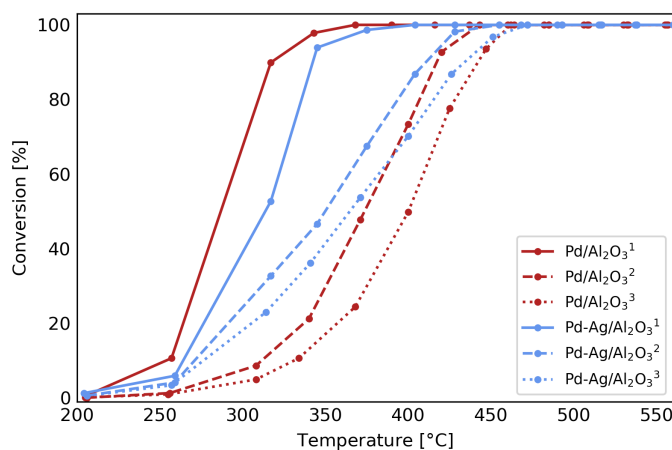
(a) Heating curves
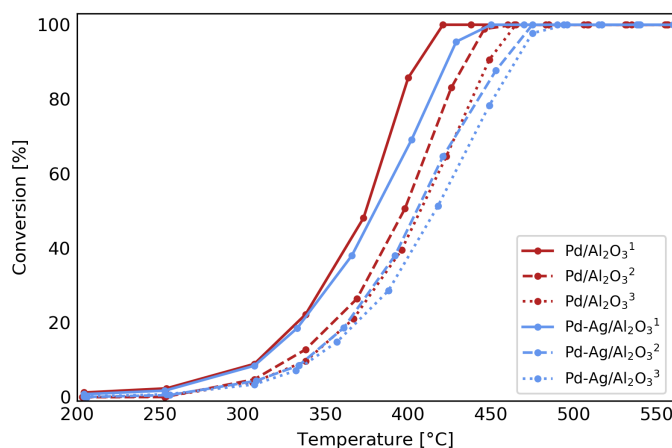
(b) Cooling curves

Figure 4.16: Conversion of methane over Pd/Al_2O_3 and $Pd\text{-}Ag/Al_2O_3$ as a function of the temperature for three reaction cycles. The reaction parameters was 4 ml min^{-1} CH_4, 95.25 ml min^{-1} O_2 and 100.75 ml min^{-1} N_2. Red curves represent the conversion curve over Pd/Al_2O_3 and the blue curves represent the conversion curve over $Pd\text{-}Ag/Al_2O_3$.

The 1st cycle of both catalysts show a distinct increase in CH_4 conversion upon the heating where a steeper slope is observed for Pd/Al_2O_3.

The light-off (temperature at 50% conversion, T_{50}, [3]) occurs at $\sim$ 287 °C for Pd/Al$_2$O$_3$ and $\sim$ 313 for °C Pd-Ag/Al$_2$O$_3$ (From Table 4.6 and Table 4.7). For the 2nd and 3rd cycle, a remarkable change in the conversion curves are observed. Here, the light-off occurs at lower temperatures for Pd-Ag/Al$_2$O$_3$ compared with Pd/Al$_2$O$_3$. In addition, the catalysts reached 100% conversion with a difference less then 10 °C. Figure 4.17 illustrates how the reaction rate at 300 °C changes for three reactions cycles over the catalysts. This demonstrates clearly that the trend is shifting after the 1st cycle, where the reaction rate over Pd-Ag/Al$_2$O$_3$ is larger in both of the subsequent cycles. This suggests that there are some changes in the surface composition and that the replacement of palladium with 25% silver do not affect the catalyst activity negatively, especially in the long run. $T_{10,50,100}$, the activation energy, E_A and the reaction rates at 300 °C are listed in Table 4.6 and Table 4.7 for Pd/Al$_2$O$_3$ and Pd-Ag/Al$_2$O$_3$, respectively.

Persson *et al.* (2005,[6]) reported that the activity and more specifically the catalyst stability is dependent on where the second metal, Ag, is found relative to the palladium particles. As confirmed by STEM, the amount of silver was enriched in regions with many small particles (approximately 82% Pd and 18% silver). No separate particles of silver were found on the support, suggesting that Pd and Ag form alloys that can reach high activity. The kinetics over alumina-supported Pd and Pd-Ag catalysts was also studied by Lee *et al.* (2019, [71]). They found that the activity of the catalysts relative to each other was highly dependent on the O$_2$/CH$_4$ ratio. According to their results, a mixed Pd-Ag oxide with better performance than PdO is formed under an oxidizing atmosphere. Yet, the oxidation state of Pd-Ag/Al$_2$O$_3$ is unknown. Based on results from XRD and knowing that silver easily loses oxygen over 250 °C, it appears to be case of mixed PdO and metallic silver particles [65].
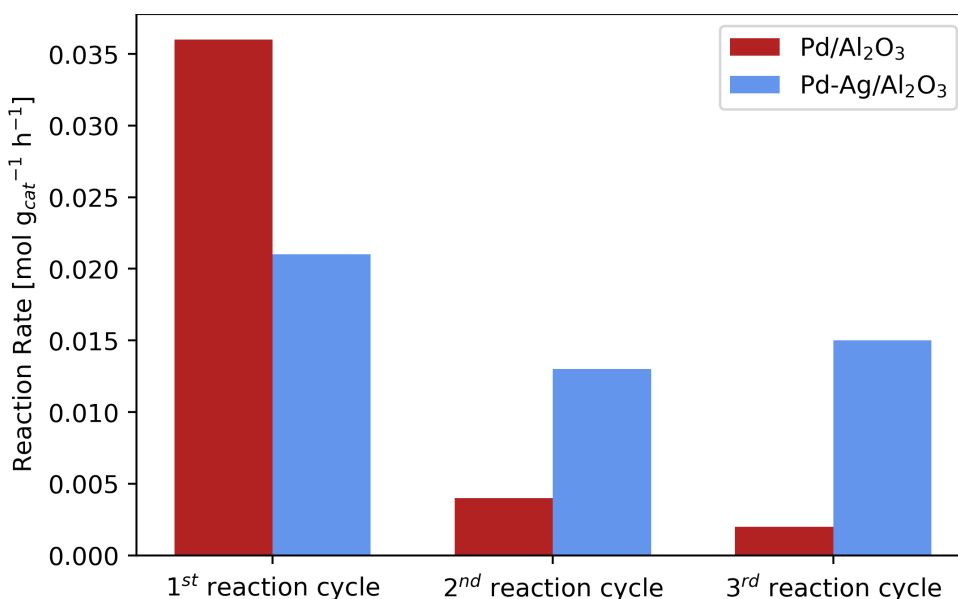
Figure 4.17: The reaction rate calculated at 300 °C for three reaction cycles over Pd/Al$_2$O$_3$(red) and Pd-Ag/Al$_2$O$_3$(blue).

Continuing to the cooling curves (Figure 4.16(b)), the trending feature is that the extinction occurs at lower temperatures for Pd/Al$_2$O$_3$ than for Pd-Ag/Al$_2$O$_3$. The cooling curves for Pd-Ag/Al$_2$O$_3$ compared to those of Pd/Al$_2$O$_3$ display lower slopes.

4.2.1.2   Influence of Water

Following the realistic exhaust conditions, the influence of water on the catalytic activity was investigated. Based on these conditions (presented in Section 2.1.1), the concentration of water was set to 10%. As already mentioned, water is found to have an inhibiting effect on catalytic activity, either by being present as a product of the reaction or when added to the reactant feed [3]. The influence of water was investigated over both of the catalysts, Pd/Al$_2$O$_3$ and Pd-Ag/Al$_2$O$_3$. Further examination of the deactivation mechanism was done by doing a cycle of dry and wet experiments.

At low temperatures the inhibitory effect of water may be more prominent as the coverage of water on active sites is favored in the low-temperature region [25]. This is also referred to as competitive adsorption of water, where methane and water compete for the active sites, leading to the formation of Pd(OH)$_2$ at PdO surface site and possibly permanent deactivation of Pd/Al$_2$O$_3$ [75, 27, 3]. Burch, Urbano and, Loader (1995, [76]) investigated the effect of water on the activity at different temperatures, where the formation of Pd(OH)$_2$ were suggested as the inactive state and PdO as the active phase. They, however, found that the deactivation was reversible and that the rate-

determining step could be loss of H_2O from $Pd(OH)_2$. For this thesis, it was found that the addition of H_2O to the feed affected the activity significantly. For Pd/Al_2O_3, shown in Figure 4.18, the curves are shifted towards higher temperatures upon the addition of water. After the second dry test (after one reaction cycle with H_2O) the activity is not recovered. For the wet reaction cycle and the 2nd dry reaction cycle, T_{100} is reached at 125 °C and 95 °C higher than for than for the 1st reaction cycle, respectively.
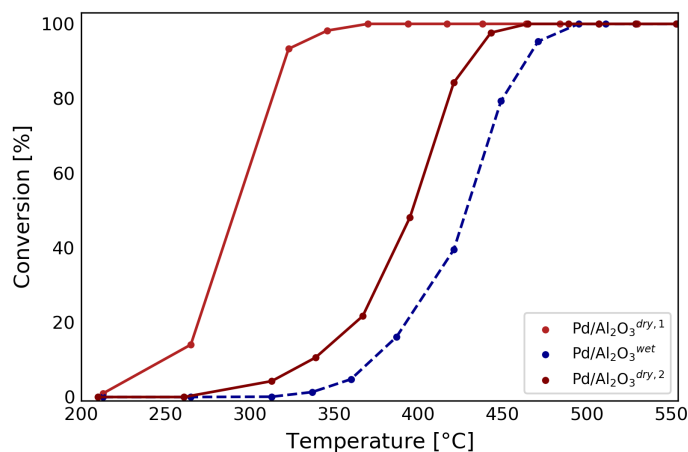
(a) Heating curve
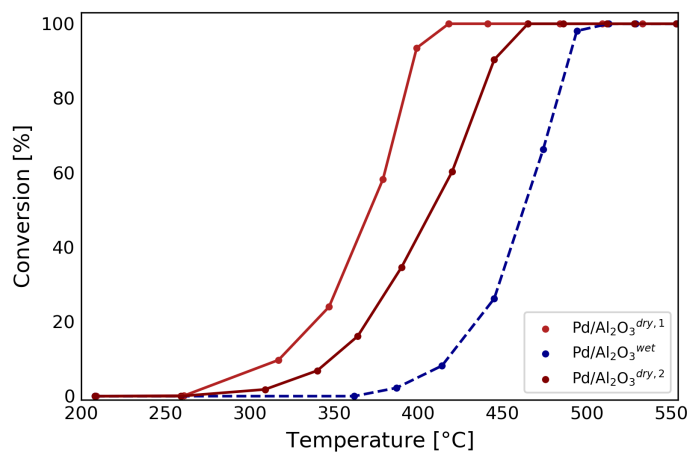
(b) Cooling curve

Figure 4.18: Conversion of methane over Pd/Al_2O_3 as a function of the catalyst bed temperature. The red curves represents the conversion curves for dry experiments performed prior (red) and after (dark red) the experiment with steam. The blue curve indicates the conversion curve when 10% H_2O was added to the feed. The reaction parameters was 4 ml min^{-1} CH_4, 95.25 ml min^{-1} O_2, 80.25 ml min^{-1} N_2 and 20 ml min^{-1} H_2O.

The same trends are displayed for Pd-Ag/Al_2O_3 in Figure 4.19. When adding water to the feed stream, the curves are shifted towards higher temperatures, including the during the cooling curve. Here, T_{100} is reached 143 °C and 95 °C higher compared with the 1st reaction cycle. It remains unclear to which degree the difference between the 1st and 3rd cycle is caused by water. As observed in Figure 4.14, Figure 4.15, and Table C.1, the catalysts display similar activity after three reaction cycles with dry and wet reactant feed. For Pd-Ag/Al_2O_3, the difference seem to be largest from $T_{10\%}$-$T_{50\%}$ (heating) but after this, the difference in activity is not prominent. $T_{100\%}$ is even reached at lower temperature compared with the third reaction cycle with dry reactant feed. According to Burch, Urbano and, Loader (1995, [76]), this can be explained by a more unstable Pd(OH)$_2$ at higher temperatures. Hence, it cannot be concluded that H_2O deactivates the catalyst permanently. The research found for the influence of water in methane oxidation over silver catalysts were found to be limited, but based on the obtained results, water seems to deactivate Pd-Ag/Al_2O_3 with the same mechanism as Pd/Al_2O_3.
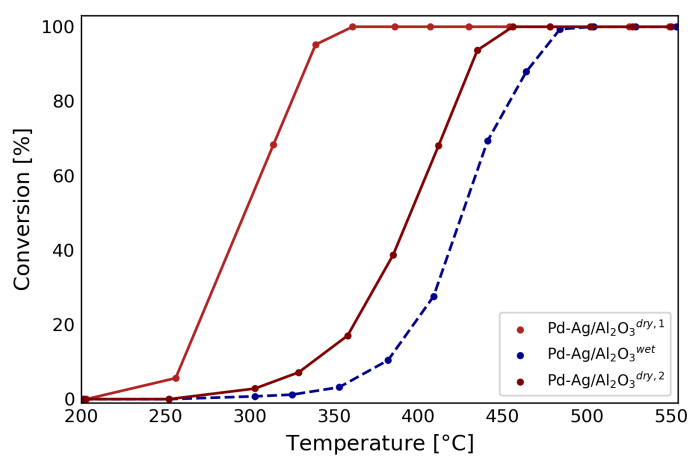
(a) Heating curve
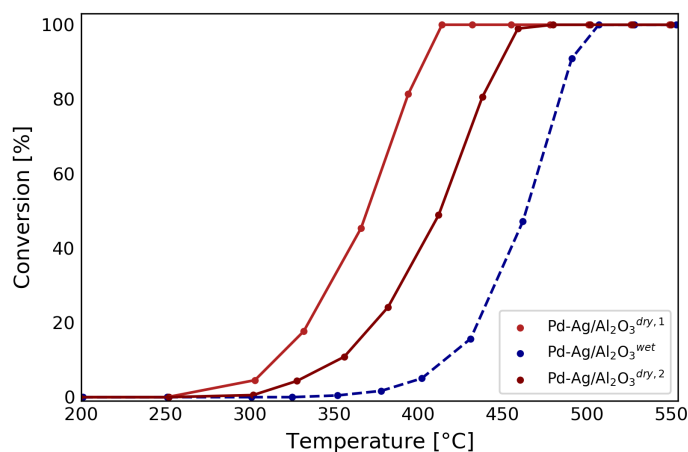
(b) Cooling curve

Figure 4.19: Conversion of methane over Pd-Ag/Al$_2$O$_3$ as a function of the catalyst bed temperature. The red curves represents the conversion curves for dry experiments performed prior (red) and after (dark red) the experiment with steam. The blue curve indicates the conversion curve when 10% H$_2$O was added to the feed. The reaction parameters was 4 ml min^{-1} CH$_4$, 95.25 ml min^{-1} O$_2$, 80.25 ml min^{-1} N$_2$ and 20 ml min^{-1} H$_2$O.

The temperatures at 10,50 and 100% conversion, T$_{10\%,50\%,100\%}$, the activation energies, E$_A$, and the reaction rate at 300° are presented in Table 4.9. Further comparison of the 2nd reaction cycle of the dry (Table 4.6) and wet experiment (Table 4.9) over Pd/Al$_2$O$_3$, shows that T$_{100}$ is reached 52 °C higher in the presence of water. These reaction cycles were regarded as a good basis for comparison since they both were conducted after one (dry) reaction cycle. The rate of reaction is also significantly decreased, from 0.004 mol/h g$_{cat}$ to 0.00003 mol/h g$_{cat}$ in presence of water. Same features are observed for Pd-Ag/Al$_2$O$_3$,

where T_{100} is reached 49 °C higher in the wet experiment (Table 4.9) compared with the 2nd dry experiment (Table 4.7). The reaction rate decreases from 0.0129 mol/h g_{cat} to 0.0003 mol/h g_{cat}. From these results, it is clear that water has an inhibiting effect on the catalytic activity, and despite variations in the apparent activation energies, E_A, of the reaction cycles, it increases consistently with presence of water for both catalysts.

Table 4.9: Temperatures at which 10,50,100% conversion levels are achieved, the apparent activation energy, E_A, and the reaction rate calculated at 300 °C for dry and wet experiments over Pd/Al$_2$O$_3$ and Pd-Ag/Al$_2$O$_3$. The reaction conditions was 4 ml min^{-1} CH$_4$, 95.25 ml min^{-1} O$_2$, 85.25 ml min^{-1} N$_2$, except for the run denoted 10% H$_2$O where 20 ml min^{-1} was added to the reactant mixture and the flow of N$_2$ was balanced to a total flow of 200 ml min^{-1}.

Catalyst	Reaction Cycle	$T_{10\%}$ [°C]	$T_{50\%}$ [°C]	$T_{100\%}$ [°C]	E_A [kJ mol^{-1}]	r [mol h^{-1} $g_{cat}$$^{-1}$]
	1	250	291	370	114	0.033
Pd/Al$_2$O$_3$	$2_{10\%H_2O}$	373	428	495	126	0.00003
	3	337	396	465	109	0.0038
	1	260	297	361	125	0.028
Pd-Ag/Al$_2$O$_3$	$2_{10\%H_2O}$	380	426	504	153	0.0003
	3	337	395	456	111	0.0014

Giezen *et al.* (1999,[27]) reported apparent activation energy of 151 ± 15 kJ/mol which was significantly higher when compared with the dry feed. This is in accordance with the obtained results for this thesis, where the activation energy increases upon the addition of water to the feed. They also reported orders of 1.0 ± 0.1 for methane, 0.1 ± 0.1 for oxygen and -0.8 ± 0.2 for water. This indicates that the addition of water to the feed may affect the originally assumed kinetic model (1 order in methane and 0 order in oxygen). However, the Arrhenius plot ((Figure C.1(e) and Figure C.2(e) in Appendix C.2.1)) shows linearity for the wet experiments.

A comparison of the results obtained over Pd/Al$_2$O$_3$ and Pd-Ag/Al$_2$O$_3$ in Figure 4.20, was however, found to be interesting. The curve for Pd-Ag/Al$_2$O$_3$ nearly fits the curve of Pd/Al$_2$O$_3$ completely, even when 25% of the palladium is replaced with silver. In the case of no interaction between water and silver, this suggests that the bimetallic catalyst is capable of retaining the activity when decreasing the palladium content. Once more, this suggests that the replacement does not affect the catalytic activity negatively, and in the case of alloy formation, the formation of Pd(OH)$_2$ might be minimized [6]. For this work, only normal reaction cycles with heating and subsequent cooling were performed with H$_2$O. It would though, be interesting to investigate the development after time on stream and if it is possible to retain this trend over a longer period. However, these results confirm that water deactivates the catalysts, most likely due to hydroxyl species on the catalyst surface that blocks the active sites [37].

The obstacles related to lean-burn NGV engine exhaust were summarized in Section 2.1.1. With 100% conversion at temperatures 495 °C (Pd/Al_2O_3) and 504 °C (Pd-Ag/Al_2O_3), both catalysts display convenient activity for low-temperature combustion application. It is interesting to note that Pd-Ag/Al_2O_3 appear as an promising candidate, especially in the aspect of catalyst stability.

(a) Heating curve

(b) Cooling curve

Figure 4.20: Conversion of methane over Pd/Al_2O_3 and Pd-Ag/Al_2O_3 as a function of the catalyst bed temperature. Red curves represent Pd/Al_2O_3 and the blue curves Pd-Ag/Al_2O_3. The reaction parameters was 4 ml min^{-1} CH_4, 95.25 ml min^{-1} O_2, 80.25 ml min^{-1} N_2 and 20 ml min^{-1} H_2O.

4.2.1.3 Catalytic Activity After Time on Stream

The long-term stability of the catalysts was investigated by keeping the temperature constant over a certain period. First, the temperature was kept constant at 350 °C for 48 h, then decreased to 300 °C for 12 h before it was decreased to 200 °C for another 48 h. Before the long-term experiment, three normal reaction cycles (with heating and subsequent cooling) were completed. The conversion of methane over Pd/Al_2O_3(red) and $Pd-Ag/Al_2O_3$(blue) as a function of time on stream is shown in Figure 4.21. Table 4.10 presents the reaction rate calculated regularly during the steps of the long-term experiments.

Figure 4.21: The conversion of methane as a function of time on stream over Pd/Al_2O_3 (red) and $Pd-Ag/Al_2O_3$ (blue). The experiment was performed over three sections: 48 hours at setpoint temperature 350 °C, 12 hours at 300 °C and 48 hours at 250 °C. The long-term experiment was conducted after 3 normal reaction cycles over the catalysts. The reaction parameters was 4 ml min^{-1} CH$_4$, 95.25 ml min^{-1} O$_2$ and 100.75 ml min^{-1} N$_2$.

As can be seen in Figure 4.21 and Table 4.10, Pd/Al_2O_3 does not seem to deactivate much with reaction time. The reaction rate at 350,300, and 250 °C was also estimated for the 3rd reaction cycle before the long-term experiment. The values of these are listed in Table 4.11 and will be used as a basis of comparison. The conversions are estimated by the polynomial fitting of the conversion curve.

The reaction rate is slightly higher at all temperature-steps after time on stream for Pd/Al_2O_3, when compared with the values in Table 4.11. The same features are reported in early studies by several authors [77, 78]. However, the catalytic activity of $Pd-Ag/Al_2O_3$ was

found to decrease significantly with time on stream. The deactivation is quite clear already after the first few hours on stream, with a decrease in conversion from 43% to approximately 20%. No catalytic activity is measured when decreasing the temperature to 250 °C. It should though be noted that the catalytic activity was initially low at this temperature (3% conversion, Table 4.11). Alternatively, it could mean that there are some dynamic changes in the surface composition after time on stream. For example, segregation of Ag from the bulk to the surface may be induced upon a change in temperature or pressure [14, 5]. However, it is difficult to explain such results without further investigation with, for example, X-ray photoelectron spectroscopy (XPS).

Slow deactivation after time on stream were reported by Roth *et al.* (2000, [79]). They showed that Pd/Al_2O_3 deactivated slowly with time on stream in the temperature range 350-450 °C. The suggested explanation for the deactivation was the formation of PdO active sites into less active sites or the inactive $Pd(OH)_2$ phase formed by water produced of the reaction. Partial restoration of the initial activity was obtained by installation of a dry carrier at 500 °C. This was attributed to the decomposition of the inactive $Pd(OH)_2$ to the active PdO phase. The inhibiting effect of water was thus investigated by adding it to the feed, resulting in a sudden dip in conversion before it continued to decrease in the same order as for the dry feed. Water inhibition has been studied in this thesis as well (Section 4.2.1.2), and was found to deactivate the catalysts.

The deactivation mechanism of Pd/Al_2O_3 is not clearly understood and less so for $Pd-Ag/Al_2O_3$. However, it is interesting how the conversion increases with time on stream at 350 °C over Pd/Al_2O_3. Most literature report this phenomenon to chlorine residual removal from the catalyst synthesis, either from the precursor or support impurities [79]. Thus, this is not representative of the trend observed in this thesis. It would be interesting to investigate the catalytic activity with time on stream upon addition of H_2O. As already reported (Section 4.2.1.2), the catalysts exhibit quite similar features upon addition of H_2O, which was found to deactivate the catalysts. If H_2O addition after time on stream exhibits the same trends as in Figure 4.21, this would suggest that morphological differences are explaining the phenomenon of increased conversion with time on stream for Pd/Al_2O_3.

Table 4.10: The catalytic activity of Pd/Al$_2$O$_3$ and Pd-Ag/Al$_2$O$_3$ after time on stream, (TOS), where T$_{bed}$ is the catalyst bed temperature and r is the reaction rate.

	Pd/Al$_2$O$_3$			Pd-Ag/Al$_2$O$_3$		
	TOS	T$_{bed}$	r	TOS	T$_{bed}$	r
	[h]	[°C]	[mol h^{-1}g$_{cat}$$^{-1}$]	[h]	[°C]	[mol h^{-1}g$_{cat}$$^{-1}$]
350 °C	12	375	0.01247	12	361	0.01097
	24	370	0.01288	24	362	0.01065
	36	371	0.01306	36	362	0.01020
	48	375	0.01423	48	360	0.01001
300 °C	50	308	0.00472	50	308	0.00234
	55	311	0.00481	55	308	0.00244
	60	315	0.00428	60	309	0.00215
250°C	72	258	0.00142	72	258	0
	84	254	0.00164	84	254	0
	96	254	0.00145	96	254	0
	108	255	0.00161	108	255	0

Table 4.11: The conversion, X, of methane over Pd/Al$_2$O$_3$ and Pd-Ag/Al$_2$O$_3$ and the reaction rate, r, calculated at temperatures 350,300 and 200 °C. The values are representative of the 3rd reaction cycle (Figure 4.14(**c**) and 4.15(**c**)).

Catalyst	Temperature	X	r
	[°C]	[%]	[mol h^{-1}g$_{cat}$$^{-1}$]
Pd/Al$_2$O$_3$	350	17	0.00916
	300	4.4	0.00233
	250	0.9	0.00048
Pd-Ag/Al$_2$O$_3$	350	42	0.02205
	300	18	0.00967
	250	3	0.00161

4.2.2 CO Oxidation

The catalytic activity measurements of Pd/Al_2O_3 and $Pd-Ag/Al_2O_3$ in CO oxidation will in the following section be presented. Three reaction cycles over each of the catalysts were performed, with different CO concentrations and maximum temperatures. The first cycle was performed with the same temperature program as in methane oxidation, i.e. with a heating rate of 5 °C/min, a maximum temperature of 550 °C, and, with subsequent cooling to room temperature. The temperature profile over the catalyst bed was not investigated. The temperature was measured at a fixed point in every reaction cycle, i.e. in the middle of the catalyst bed. The CO concentration was 2%. The 1st reaction cycle over both catalysts are shown in Figure 4.22. The light off (50% conversion) occurs at ~ 134 °C over Pd/Al_2O_3 and ~ 183 °C over $Pd-Ag/Al_2O_3$. With approximately the same conversion during ignition and extinction, no hysteresis is observed over Pd/Al_2O_3 in the 1st reaction cycle. For $Pd-Ag/Al_2O_3$, however, higher conversions during the extinction are observed, yielding a normal hysteresis.
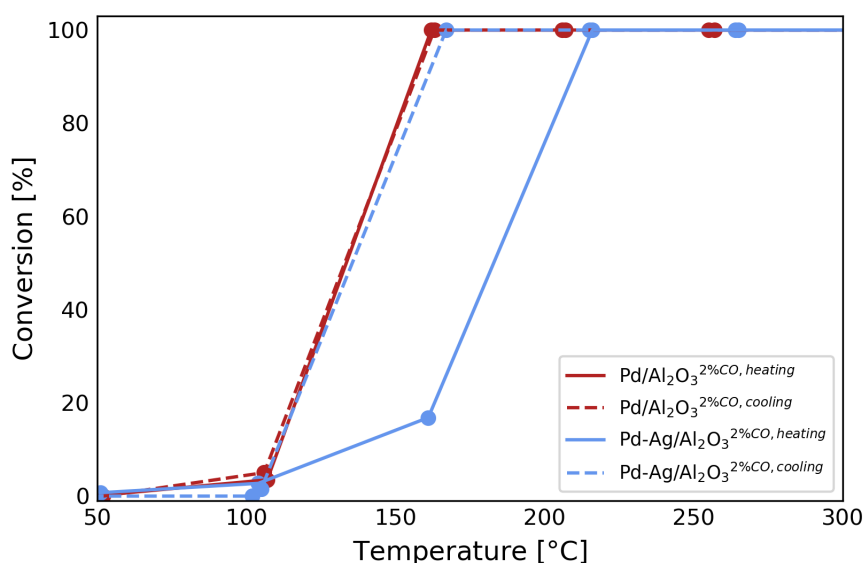
Figure 4.22: The conversion of CO as function of function of catalyst bed temperature over Pd/Al_2O_3(red) and $Pd-Ag/Al_2O_3$(blue). The reaction parameters was 4 ml min^{-1} CO, 95.25 ml min^{-1} O_2 and 100.75 ml min^{-1} N_2.

The two subsequent reaction cycles were performed with the same heating rate but with a maximum temperature of 300 °C. In addition, the CO concentration was increased to 5%. Due to technical issues, the temperature measurements of the catalyst bed were lost for the 2nd reaction cycle over Pd/Al_2O_3. Therefore, the set-point temperature will be used for this reaction cycle instead. It should though be noted

that the measured catalyst bed temperature was slightly higher for all previous experiments.
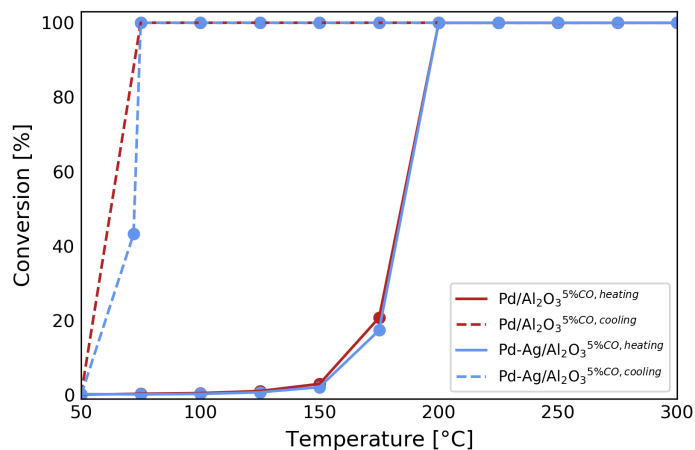
(a) 2nd reaction cycle over Pd/Al$_2$O$_3$(red) and Pd-Ag/Al$_2$O$_3$(blue).
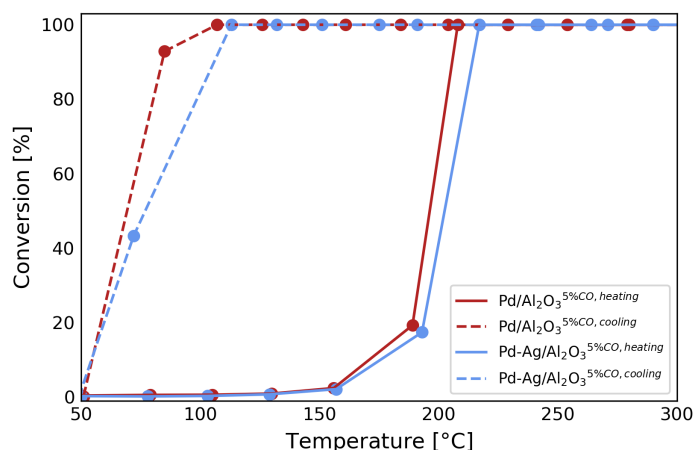
(b) 3rd reaction cycle over Pd/Al$_2$O$_3$(red) and Pd-Ag/Al$_2$O$_3$(blue).

Figure 4.23: The conversion of CO as function of catalyst bed temperature over Pd/Al$_2$O$_3$(red) and Pd-Ag/Al$_2$O$_3$(blue). The reaction parameters was 10 ml min^{-1} CO, 95.25 ml min^{-1} O$_2$ and 94.75 ml min^{-1} N$_2$.

The 2nd and 3rd cycles (Figure 4.23) display the normal hysteresis with lower conversion during ignition and a distinct increase in CO conversion during extinction. The behavior of the hysteresis CO oxidation over palladium-supported catalysts is extensively studied and is shown to be dependent on several parameters. For instance, the hysteresis behavior is proven to be dependent on inlet CO concentration, temperature, heating ramp, and surface contamination [19, 14, 5]. Therefore, the experimental conditions were monitored for the 2nd and 3rd cycles, by changing the CO concentration and maximum tem-

perature to investigate the influence on the hysteresis. For both catalysts, the width of the hysteresis increased significantly. Especially for Pd/Al$_2$O$_3$, with no hysteresis at CO concentration of 2% to a broad hysteresis with CO concentration of 5%.

As described in Section 2.1.4, a three-region activity is normally reported as the cause of the hysteresis. Low CO conversion in the first region is attributed to CO inhibition, i.e. competitive adsorption of CO and O$_2$ [1]. During this region, the surface is mainly covered by CO. As the temperature increases (beyond the light-off), the activity increases, and a subsequent region of bi-stability before extinction is observed [19]. Hence, it seems like CO oxidation of Pd/Al$_2$O$_3$ and Pd-Ag/Al$_2$O$_3$ follows a typical ignition-extinction curve at 5% CO concentration and maximum temperature of 300 °C. According to Carlsson *et al.* (2011, [1]) this hysteresis behavior can be attributed to kinetic bistability, reaction kinetics and diffusion phenomena, and heat effects. The latter cause is a consequence of heat generation by the exothermic reaction which heats the catalyst. For this thesis, the catalysts were diluted in SiC to some extent prevent this.

Table 4.12: Summary of the light-off temperatures, T$_{ig}$ (50% conversion) and subsequent extinction, T$_{ex}$, apparent activation energy, E$_A$, and the reaction rate calculated at 150 °C.

Feed mol% CO	Catalyst	Reaction Cycle	T$_{ig}$ [°C]	T$_{ex}$ [°C]	T$_{100\%}$ [°C]	E_A [kJ mol^{-1}]	r [mol h^{-1}g$_{cat}$$^{-1}$]
2%	Pd/Al$_2$O$_3$	1	134	133	162	83	0.04201
2%	Pd-Ag/Al$_2$O$_3$	1	183	136	216	94	0.00752
5%	Pd/Al$_2$O$_3$	2	184	61	200	194	0.00403
5%	Pd-Ag/Al$_2$O$_3$	2	185	72	200	215	0.00287
5%	Pd-Ag/Al$_2$O$_3$^{bed}	2	203	77	217	232	0.00241
5%	Pd/Al$_2$O$_3$	3	196	65	208	294	0.00281
5%	Pd-Ag/Al$_2$O$_3$	3	202	85	218	231	0.00167

It is well-known that the apparent activation energy, reaction orders, and reaction rate as a function of temperature vary strongly with temperature for CO oxidation [20]. Hence, the interpretation of these is not straightforward. Table 4.12 shows an estimation of the light-off temperature, T_{ig}, and subsequent extinction, T_{ex}, the apparent activation energy, E_A, and the reaction rate, r, at 150 °C. The apparent activation energy, E$_A$, was found for conversion levels of 20-50% and the representative Arrhenius plots are shown in Figure C.5 and Figure C.6 in Appendix C.3. It should, again, be noted that this is an estimation. These values will strongly vary depending on where in the reaction cycle they are calculated. Moreover, the experimental setup should be optimized and monitored for more reasonable data for these values but will be used as a basis of comparison in this thesis. Orders with respect to O$_2$ and CO, was reported zero and one by Matsushima *et al.* (1975, [80]). This was argued valid for temperatures below 473 K and p$_{O2}$ > p$_{CO}$. Based on this, orders of zero and one in O$_2$ and CO, respectively, were assumed in this thesis as well.

From Figure 4.22 and 4.23, and Table 4.12, it is clear that the largest difference between the ignition and extinction temperatures is at 2% CO concentration. Here, the ignition are shifted towards higher temperatures for Pd-Ag/Al$_2$O$_3$, but extinction occur at similar temperatures for both catalysts. This suggests that the inhibiting effect of CO is largest for Pd-Ag/Al$_2$O$_3$. With a palladium rich surface, this would mean that a concentration of 2% CO is not large enough to cover the surface completely, resulting in a lower light-off temperature for Pd/Al$_2$O$_3$ compared with Pd-Ag/Al$_2$O$_3$.

When switching to 5% CO concentration, the catalysts exhibit similar hysteresis behaviors. The ignition and extinction temperatures are slightly shifted towards higher temperatures for Pd-Ag/Al$_2$O$_3$ and being especially prominent for the 3rd reaction cycle. However, as mentioned, this might arise from the difference between the set-point temperature and measured catalyst bed temperature, where the latter one was lost for the 2nd reaction cycle over Pd/Al$_2$O$_3$. Thus, it cannot be excluded that the difference between the reaction cycles with 5% CO would be smaller if the catalyst bed temperature was used. Furthermore, a comparison of the two reaction cycles over Pd-Ag/Al$_2$O$_3$ with 5% CO and with conversion as function of catalyst bed temperature, shows that the activity is similar for the two cycles. Based on this observation, it is assumed that Pd/Al$_2$O$_3$ would display similar activity during both reaction cycles with 5% CO concentration if the catalyst bed temperature was used.

The reaction rates presented in Table 4.12 decrease as a function of reaction cycles, with larger reaction rates over Pd/Al$_2$O$_3$ in all reaction cycles. The discussed assumption of a stronger CO inhibition during ignition for Pd-Ag/Al$_2$O$_3$ seems to apply for all reaction cycles. Both catalysts display positive apparent activation energies and seem to increase with increasing CO concentration. When comparing the E$_A$ of the 2nd and 3rd reaction cycle of Pd-Ag/Al$_2$O$_3$, similar apparent activation energies are observed with 232 and 231 kJ/mol, respectively. This is in accordance with observations in STEM images, revealing no significant signs of deactivation of spent catalyst.

It is suggested that the difference in apparent activation energy of Pd/Al$_2$O$_3$ between reaction cycle 2 and 3 is not representable of the catalytic behavior during reaction cycles. This is grounded with the fact that the apparent activation energy is strongly depended on temperature and that they are calculated with different basis of temperature (set-point temperature for the 2nd cycle and catalyst bed temperature for the 3rd cycle).

Chapter 5

Conclusion and Future Work

5.1 Conclusions

In this master´s thesis, the catalytic activity of monometallic Pd/Al_2O_3 and bimetallic $Pd-Ag/Al_2O_3$ have been investigated for low-temperature oxidation of methane and carbon monoxide, with promising results considering pollution abatement.

In total, two catalysts were prepared according to the incipient wetness impregnation method, whereby a co-impregnation of the metals was used for the bimetallic catalyst. The catalysts were characterized with XRF, XRD, N_2 physisorption, TEM, Chemisorption, and TPR. The catalytic activities were investigated in a reaction rig adapted for CH_4 oxidation and CO oxidation. In low-temperature oxidation of methane, the catalytic activity was investigated following realistic exhaust gas conditions, i.e. at low temperatures, excess oxygen, low CH_4 concentration, and in presence of water vapor. Further, CO oxidation was investigated for the dependency of CO concentration and maximum temperature.

The characterization of the materials leads to the following conclusions: By XRD, palladium appeared only in its oxide state, PdO. No single metal or oxide phases of silver were detected by XRD. This was in line with the results from STEM. EDS in STEM mode found silver and palladium enriched in regions with many small particles. No single silver particles were found. In contrast, PdO, was found as single particles and clusters. This suggests a mixed distribution of single PdO particles, PdO clusters, and Pd-Ag alloys. Further examination with TPR provided a basis for Pd-Ag alloy formation. A much less intensive negative peak was observed for $Pd-Ag/Al_2O_3$. This was attributed to the increased hydrogen solubility of the alloy, a phenomenon that is well-documented in the literature. With large surface area and high dispersion, both Pd/Al_2O_3 and $Pd-Ag/Al_2O_3$ may be considered promising candidates for low-temperature oxidation.

In low-temperature oxidation of methane, hysteresis effects were observed for both catalysts. The hysteresis was suggested to be dependent on: 1) ignition and extinction behavior and 2) the number of reaction cycles. The hysteresis in both cases was of reversed nature, i.e. lower conversions during extinction. Three possible explanations were suggested for the hysteresis behavior: 1) Partially reduction of the surface by methane dissociation products, 2) deactivation, for example, by water produced by the reaction and 3) a more thermodynamically stable state of the atoms after subsequent cycles. The latter one was attributed to a change observed for the hysteresis width. This effect was especially prominent for Pd/Al_2O_3.

The replacement of 25% palladium with silver did not seem to affect the catalytic activity dramatically. Especially after reaction cycling, where the rate of reaction was higher for $Pd-Ag/Al_2O_3$ than for Pd/Al_2O_3 in a reactant feed comprised of 2% CH_4, 10% O_2 and 88% N_2. In presence of water, the catalysts displayed similar features, even when 25% of the palladium was replaced with silver. These findings suggested that the formation of inactive $Pd(OH)_2$ by water could be minimized upon alloy formation of Pd and Ag. Overall, in a reactant feed comprised of 2% CH_4, 10% O_2, 10% H_2O and balance N_2 (realistic exhaust gas conditions), the results demonstrated that there was a strong effect of water on the catalytic activity for both catalyst. However, the catalysts exhibited convenient catalytic performance for low-temperature combustion application, with T_{100} reached at 495 °C and 505 °C for Pd/Al_2O_3 and $Pd-Ag/Al_2O_3$, respectively. Moreover, the catalytic activity of $Pd-Ag/Al_2O_3$ was found to decrease significantly with time on stream. This result provided a basis for a potential dynamic change in the catalyst surface composition, for example by segregation of silver to the catalyst surface. Further research with for example NAP-XPS, is, however, needed to confirm this.

Hysteresis effects were also observed for CO oxidation over Pd/Al_2O_3 and $Pd-Ag/Al_2O_3$. In contrast to CH_4 oxidation, the hysteresis was of normal nature, i.e. higher conversion during extinction. Especially, the hysteresis was found to change strongly when changing the inlet concentration of CO from 2%-5%. In general, these findings are consistent with research showing that the hysteresis is dependent on inlet CO concentration. This effect was most prominent for Pd/Al_2O_3 but changes in hysteresis width was observed for both catalysts. At 5% CO concentration, the catalysts display similar temperature dependency during heating and cooling, with slightly better catalytic performance of Pd/Al_2O_3.

The main conclusion that can be drawn is that both catalysts display sufficient catalytic activity in methane- and CO oxidation.

5.2   Future Work

Based on the results achieved in this research, Pd-Ag/Al$_2$O$_3$ should be further investigated for the application of low temperature oxidation of methane and carbon monoxide. First, the dependency of synthesis procedure was not covered by this thesis. For example, it would be interesting to perform a sequential impregnation of the metals rather than co-impregnation and explore how this will affect the catalytic properties.

Future research should consider the potential effects of water after time on stream. This research considered only normal reaction cycles, with heating and subsequent cooling. Based on the obtained results, water was found to strongly inhibit the catalytic activity of both catalysts. Since the catalysts displayed very similar features upon addition of water, it would be of interest to see if this is maintained after time on stream. Moreover, since only the presence of water in the reactant feed was investigated, future research should be conducted in more realistic settings to the proper exhaust gas, for example by adding CO$_2$ to the reactant mixture. Water is, however, reported as the most crucial challenge related to the reaction conditions. Thus, the catalytic activity in presence of larger H$_2$O concentrations, for example 15% is also important for examining the catalyst stability. Nevertheless, the effect of water in CO oxidation over the catalysts are also of interest.

In addition, further examination of the hysteresis effects in CH$_4$ and CO oxidation is an interesting topic for future work. For example, future research could examine this strategically by monitoring the catalyst amount, changing the heating rate, running several reaction cycles, or changing the maximum temperature. This would provide a good starting point for discussion of the surface dynamics of Pd/Al$_2$O$_3$ and Pd-Ag/Al$_2$O$_3$ and for comparison with NAP-XPS data obtained over Pd and Pd-Ag single crystal [14, 5]. Investigating this further might prove important mechanisms related to the performance of the catalysts towards low-temperature oxidation.

Bibliography

[1] Carlsson, P.A. and Skoglundh, M. Low-temperature oxidation of carbon monoxide and methane over alumina and ceria supported platinum catalysts. *Applied Catalysis B: Environmental*, 101(3-4):669–675, jan 2011.

[2] Heck, R.M., Farrauto, R.J., and Gulati, S.T. *Catalytic Air Pollution Control: Commercial Technology*. John Wiley and Sons, New York, second edition, 2002.

[3] Gélin, P. and Primet, M. Complete oxidation of methane at low temperature over noble metal based catalysts: A review. *Applied Catalysis B: Environmental*, 39(1):1–37, nov 2002.

[4] Centi, G. Supported palladium catalysts in environmental catalytic technologies for gaseous emissions. *Journal of Molecular Catalysis A: Chemical*, 173(1-2):287–312, sep 2001.

[5] Strømsheim, M.D., Svenum, I.-H., Mahmoodinia, M., Boix, V., Knudsen, J., and Venvik, H.J. Segregation dynamics of a Pd-Ag surface during CO oxidation investigated by NAP-XPS. *Catalysis Today*, feb 2021.

[6] Persson, K., Ersson, A., Jansson, K., Iverlund, N., and Järås, S. Influence of co-metals on bimetallic palladium catalysts for methane combustion. *Journal of Catalysis*, 231(1):139–150, apr 2005.

[7] M. Skoglundh, L. O. Löwendahl, and J. E. Otterated. Combinations of platinum and palladium on alumina supports as oxidation catalysts. *Applied Catalysis*, 77(1):9–20, oct 1991.

[8] Rocha, T.C.R., Oestereich, A., Demidov, D.V, Hävecker, M., Zafeiratos, S., Weinberg, G., Bukhtiyarov, V.I., Knop-Gericke, A., and Schlögl, R. The silver-oxygen system in catalysis: new insights by near ambient pressure X-ray photoelectron spectroscopy. *Phys. Chem. Chem. Phys*, 14:4554–4564, 2012.

[9] Skogheim, S. *Catalytic Methane Abatement for Natural Gas Engines*, 2020.

[10] Sandvik, H. M. *Catalysis for Control of Methane Slip in Marine Machinery Using a Palladium based Catalyst*. Master's thesis, Norwegian University of Science, 2016.

[11] Storrvik, H.M. *Catalysis for control of methane slip in marine machinery Using platinum-based catalysts*. Master's thesis, Norwegian University of Science, 2016.

[12] Brokstad, R.L-J. *Nickel Cobalt Catalyst for Methane Abatement in Marine Machinery*. Master's thesis, Norwegian University of Science, 2017.

[13] Selnes, J.A. *$NiCo_2O_4$ Catalyst on commercial Low Surface Area and Synthesized High Surface Area CeO_2 For Catalytic Methane Abatement in Natural Gas Engines*. Master's thesis, Norwegian University of Science, 2020.

[14] Fernandes, V.R., Bossche, M. Van Den, Knudsen, J., Farstad, M.H., Gustafson, J., Venvik, H.J., Grönbeck, H., and Borg, A. Reversed Hysteresis during CO Oxidation over Pd75Ag25(100). *ACS Catalysis*, 6(7):4154–4161, jul 2016.

[15] Global Warming Potentials (IPCC Fourth Assessment Report) | UNFCCC. https://unfccc.int/process-and-meetings/transparency-and-reporting/greenhouse-gas-data/frequently-asked-questions/global-warming-potentials-ipcc-fourth-assessment-report. Accessed: 2021-02-22.

[16] Chen, J., Arandiyan, H., Gao, X., and Li, J. Recent Advances in Catalysts for Methane Combustion. *Catalysis Surveys from Asia*, 19(3):140–171, sep 2015.

[17] Monai, M., Montini, T., Gorte, R.J., and Fornasiero, P. Catalytic Oxidation of Methane: Pd and Beyond. *European Journal of Inorganic Chemistry*, 2018(25):2884–2893, jul 2018.

[18] Dey, S., Dhal, G.C., Mohan, D., and Prasad, R. Synthesis of highly active Cobalt catalysts for low temperature CO oxidation. *Chemical Data Collections*, 24, dec 2019.

[19] Mohammad, R., Soubaihi, A., and Saoud, K.M.and Dutta, J. Critical Review of Low-Temperature CO Oxidation and Hysteresis Phenomenon on Heterogeneous Catalysts. *Catalysts*, 8, 2018.

[20] Chorkendorff, I. and Niemantsverdriet, J. W. *Concepts of Modern Catalysis and Kinetics*. Wiley-VCH Verlag GmbH & Co. KGaA, Weinheim, third, com edition, 2013.

[21] Zhou, Y., Wang, Z., and Liu, C. Perspective on CO oxidation over Pd-based catalysts. *Catalysis science technology*, 5(1):69–81, 2015.

[22] Hayes, R.E. Kolaczkowski, S.T. Li, P.K.C. Awdry, S. The palladium catalysed oxidation of methane: Reaction kinetics and the effect of diffusion barriers. *Chemical Engineering Science*, 56(16):4815–4835, sep 2001.

[23] Oh, Se H. Mitchell, P. J. Siewert, R. M. Methane oxidation over alumina-supported noble metal catalysts with and without cerium additives. *Journal of Catalysis*, 132(2):287–301, dec 1991.

[24] Burch, R. and Loader, P. K. Investigation of Pt/Al2O3 and Pd/Al2O3 catalysts for the combustion of methane at low concentrations. *Applied Catalysis B, Environmental*, 5(1-2):149–164, dec 1994.

[25] Kikuchi, R., Maeda, S., Sasaki, K., Wennerström, S., and Eguchi, K. Low-temperature methane oxidation over oxide-supported Pd catalysts: Inhibitory effect of water vapor. *Applied Catalysis A: General*, 232(1-2):23–28, jun 2002.

[26] Velin, P., Ek, M., Skoglundh, M., Schaefer, A., Raj, A., Thompsett, D., Smedler, G., and Carlsson, P.A. Water Inhibition in Methane Oxidation over Alumina Supported Palladium Catalysts. *Journal of Physical Chemistry C*, 123(42):25724–25737, oct 2019.

[27] Van Giezen, J. C., Van Den Berg, F. R., Kleinen, J. L., Van Dillen, A. J., and Geus, J. W. The effect of water on the activity of supported palladium catalysts in the catalytic combustion of methane. *Catalysis Today*, 47(1-4):287–293, jan 1999.

[28] Yamamoto, H. and Uchida, H. Oxidation of methane over Pt and Pd supported on alumina in lean-burn natural-gas engine exhaust. *Catalysis Today*, 45(1-4):147–151, oct 1998.

[29] Narui, K., Yata, H., Furuta, K., Nishida, A., Kohtoku, Y., and Matsuzaki, T. Effects of addition of Pt to PdO/Al2O3 catalyst on catalytic activity for methane combustion and TEM observations of supported particles. *Applied Catalysis A: General*, 179(1-2):165–173, apr 1999.

[30] Ersson, A., Kušar, H.and Carroni, R.and Griffin, T., and Järås, S. Catalytic combustion of methane over bimetallic catalysts a comparison between a novel annular reactor and a high-pressure reactor. *Catalysis today*, 83(1-4):265–277, aug 2003.

[31] Zhang, Q., Li, J., Liu, X., and Zhu, Q. Synergetic effect of Pd and Ag dispersed on Al2O3 in the selective hydrogenation of acetylene. *Applied Catalysis A: General*, 197(2):221–228, may 2000.

[32] Sheth, P. A., Neurock, M., and Smith, C. M. First-principles analysis of the effects of alloying Pd with Ag for the catalytic hydrogenation of acetylene-ethylene mixtures. *Journal of Physical Chemistry B*, 109(25):12449–12466, jun 2005.

[33] Vicinanza, N., Svenum, I.H., Næss, L. N., Peters, T. A., Bredesen, R., Borg, A., and Venvik, H. J. Thickness dependent effects of solubility and surface phenomena on the hydrogen transport properties of sputtered Pd77%Ag23% thin film membranes. *Journal of Membrane Science*, 476:602–608, feb 2015.

[34] Li, Y., Liu, F., Fan, Y, Cheng, G., Song, W., and Zhou, J. Silver palladium bimetallic core-shell structure catalyst supported on TiO2 for toluene oxidation. *Applied Surface Science*, 462:207–212, dec 2018.

[35] Salomonsson, P., Johansson, S., and Kasemo, B. Methane oxidation over PdOx: on the mechanism for the hysteresis in activity and oxygen content. *Catalysis Letters*, 33(1-2):1–13, mar 1995.

[36] Mihai, O., Smedler, G. and Nylén, U., Olofsson, M., and Olsson, L. The effect of water on methane oxidation over Pd/Al2O3 under lean, stoichiometric and rich conditions. *Catalysis Science and Technology*, 7(14):3084–3096, jul 2017.

[37] Sadokhina, N., Smedler, G., Nylén, U., Olofsson, M., and Olsson, L. The influence of gas composition on Pd-based catalyst activity in methane oxidation inhibition and promotion by NO. *Applied Catalysis B: Environmental*, 200:351–360, jan 2017.

[38] Richardson, J.T. *Principles of Catalyst Development*. Plenum Press, New York, 1989.

[39] Ertl, G., Knözinger, H., and Weitkamp, J. *Handbook of Heterogeneous Catalysis*. Wiley, jul 1997.

[40] Marceau, E., Carrier, X., and Che, M. Impregnation and Drying. In *Synthesis of Solid Catalysts*, pages 59–82. Wiley-VCH Verlag GmbH & Co. KGaA, Weinheim, oct 2009.

[41] Liao, F., Lo, T.W.B., and Tsang, S.C.E. Recent Developments in Palladium-Based Bimetallic Catalysts. *ChemCatChem*, 7(14):1998–2014, jul 2015.

[42] Marguí, E. and Grieken, René Van. *X-Ray Fluorescence Spectrometry and Related Techniques : An Introduction*. Momentum Press, New York NY, 2013.

[43] What is XRF (X-ray fluorescence) and How Does it Work? https://www.thermofisher.com/blog/ask-a-scientist/what-is-xrf-x-ray-fluorescence-and-how-does-it-work/. Accessed: 2021-02-05.

[44] Richard, D.R. and Rousseau, M. Detection limit and estimate of uncertainty of analytical XRF results. *The Rigaku Journal*, 18(2):33, 2001.

[45] Schlögl, R. Chapter 5 X-ray Diffraction. A Basic Tool for Characterization of Solid Catalysts in the Working State. In *Advances in Catalysis*, volume 52, pages 273–338. Academic Press, jan 2009.

[46] Bartholomew, C.H. and Farrauto, R.J. *Fundamentals of industrial catalytic processes*. Wiley-Interscience, Hoboken, N.J, 2nd ed. edition, 2006.

[47] Niemantsverdriet, J. W. *Spectroscopy in Catalysis: An Introduction*. Weinheim: John Wiley & Sons, Incorporated, third edition, jun 2007.

[48] Wachs, I. *Characterization of Catalytic Materials:*. Momentum Press, New York, 1993.

[49] Anderson, J.A. *Supported Metals In Catalysis*. World Scientific Publishing Company, Singapore, 2nd edition, 2011.

[50] Canton, P., Fagherazzi, G., Battagliarin, M., Menegazzo, F.and Pinna, F., and Pernicone, N. Pd/CO average chemisorption stoichiometry in highly dispersed supported Pd/γ-Al2O3 catalysts. *Langmuir*, 18(17):6530–6535, aug 2002.

[51] Mekki-Berrada, A. and Auroux, A. Thermal Methods. In *Characterization of Solid Materials and Heterogeneous Catalysts*, volume 2, pages 747–852. Wiley-VCH Verlag GmbH & Co. KGaA, Weinheim, Germany, apr 2012.

[52] Makrides, A. C. Absorption of hydrogen by silver-palladium alloys. *Journal of Physical Chemistry*, 68(8):2160–2169, 1964.

[53] Lewis, F. A. Hydrogen in palladium and palladium alloys. *International Journal of Hydrogen Energy*, 21(6):461–464, 1996.

[54] Fazle Kibria, A. K.M. and Sakamoto, Y. Effect of alloying of palladium with silver and rhodium on the hydrogen solubility, miscibility gap and hysteresis. *International Journal of Hydrogen Energy*, 25(9):853–859, sep 2000.

[55] Blumberg, L. M. Theory of Gas Chromatography. In *Gas Chromatography*, pages 19–78. Elsevier Inc., Oxford, jan 2012.

[56] kromatografi – Store norske leksikon. https://snl.no/kromatografi. Accessed: 2021-04-21.

[57] John M.Miller. *Chromatography: concepts and contrasts*. Wiley, Hoboken, N.J., 2nd ed. edition, 2005.

[58] Vannice, A.M. *Kinetics of Catalytic Reactions*. Springer, 2005.

[59] Salomons, S., Hayes, R. E., Votsmeier, M., Drochner, A., Vogel, H., Malmberg, S., and Gieshoff, J. On the use of mechanistic CO oxidation models with a platinum monolith catalyst. *Applied Catalysis B: Environmental*, 70(1-4):305–313, jan 2007.

[60] Ma, L., Trimm, D. L., and Jiang, C. The design and testing of an autothermal reactor for the conversion of light hydrocarbons to hydrogen I. The kinetics of the catalytic oxidation of light hydrocarbons. *Applied Catalysis A: General*, 138(2):275–283, may 1996.

[61] aktiveringsenergi – Store norske leksikon. `https://snl.no/aktiveringsenergi`. Accessed: 2021-04-13.

[62] Fogler, H.S. *Elements of Chemical Reaction Engineering*. Prentice Hall, Boston, fifth edition, 2016.

[63] Svenum, I. H., Herron, J. A., Mavrikakis, M., and Venvik, H. J. Adsorbate-induced segregation in a PdAg membrane model system: Pd 3Ag(1 1 1). *Catalysis Today*, 193(1):111–119, oct 2012.

[64] Bouwman, R., Lippits, G. J.M., and Sachtler, W. M.H. Photoelectric investigation of the surface composition of equilibrated AgPd alloys in ultrahigh vacuum and in the presence of CO. *Journal of Catalysis*, 25(3):350–361, jun 1972.

[65] Karski, S., Witońska, I., Rogowski, J., and Gołuchowska, J. Interaction between Pd and Ag on the surface of silica. *Journal of Molecular Catalysis A: Chemical*, 240(1-2):155–163, oct 2005.

[66] Vitos, L., Ruban, A. V., Skriver, H. L., and Kollár, J. The surface energy of metals. *Surface Science*, 411(1-2):186–202, aug 1998.

[67] Wouda, P. T., Schmid, M., Nieuwenhuys, B. E., and Varga, P. Adsorbate migration on PdAg(111). *Surface Science*, 423(1):L229–L235, mar 1999.

[68] Løvvik, O. M. and Opalka, S. M. Reversed surface segregation in palladium-silver alloys due to hydrogen adsorption. *Surface Science*, 602(17):2840–2844, sep 2008.

[69] Chandra Shekar, S., Krishna Murthy, J., Kanta Rao, P., and Rama Rao, K. S. Selective hydrogenolysis of dichlorodifluoromethane on carbon covered alumina supported palladium catalyst. *Journal of Molecular Catalysis A: Chemical*, 191(1):45–59, jan 2003.

[70] Aznárez, A., Gil, A., and Korili, S.A. Performance of palladium and platinum supported on alumina pillared clays in the catalytic combustion of propene †. *RSC advances*, 5(100):82296–82309, 2015.

[71] Lee, G., Zheng, W., Goulas, K.A., Lee, I.C., and Vlachos, D.G. 110th Anniversary: Kinetics and X-ray Absorption Spectroscopy in Methane Total Oxidation over Alumina-Supported Pt, Pd, and Ag-Pd Catalysts. *Industrial and Engineering Chemistry Research*, 58(38):17718–17726, sep 2019.

[72] Su, S.C., Carstens, J.N., and Bell, A.T. A study of the dynamics of Pd oxidation and PdO reduction by H2 and CH4. *Journal of Catalysis*, 176(1):125–135, may 1998.

[73] Ribeiro, F. H., Chow, M., and Dalla Betta, R. A. Kinetics of the complete oxidation of methane over supported palladium catalysts. *Journal of Catalysis*, 146(2):537–544, apr 1994.

[74] Cullis, C. F. and Willatt, B. M. Oxidation of methane over supported precious metal catalysts. *Journal of Catalysis*, 83(2):267–285, oct 1983.

[75] Cullis, C. F., Nevell, T. G., and Trimm, D. L. Role of the catalyst support in the oxidation of methane over palladium. *Journal of the Chemical Society, Faraday Transactions 1: Physical Chemistry in Condensed Phases*, 68(0):1406–1412, jan 1972.

[76] Burch, R., Urbano, F. J., and Loader, P. K. Methane combustion over palladium catalysts: The effect of carbon dioxide and water on activity. *Applied Catalysis A, General*, 123(1):173–184, mar 1995.

[77] Baldwin, T. R. and Burch, R. Catalytic combustion of methane over supported palladium catalysts. I. Alumina supported catalysts. *Applied Catalysis*, 66(1):337–358, 1990.

[78] Briot, P. and Primet, M. Catalytic oxidation of methane over palladium supported on alumina. Effect of aging under reactants. *Applied Catalysis*, 68(1):301–314, jan 1991.

[79] Roth, D. , Gélin, P., Primet, M., and Tena, E. Catalytic behaviour of Cl-free and Cl-containing Pd/Al2O3 catalysts in the total oxidation of methane at low temperature. *Applied Catalysis A: General*, 203(1):37–45, sep 2000.

[80] Matsushima, T., Almy, D. B., Foyt, D. C., Close, J. S., and White, J. M. On the mechanism and kinetics of the CO-oxidation reaction on polycrystalline palladium. II. The kinetics. *Journal of Catalysis*, 39(2):277–285, aug 1975.

Appendix A

Calculations

A.1 Catalyst synthesis - Incipient Wetness Impregnation

A.1.1 Monometallic Catalyst

Equation (A.1) gives the relation between mass, amount of substance and molar mass.

$$m = n \cdot Mm \quad [g] \tag{A.1}$$

The amount of $Pd(NO_3)_2 \cdot 2H_2O$ needed for the synthesis of 2.0wt% Pd/Al_2O_3 was calculated according to Equation (A.2) - (A.4), where *wt%Pd* is the desired weight percent of Pd and $m_{Al_2O_3}$ is the amount of support.

$$\begin{aligned} m_{Pd} &= \frac{wt\%Pd \cdot m_{Al_2O_3}}{100\%} \\ &= \frac{2\% \cdot 10g}{100\%} \\ &= 0.20g \end{aligned} \tag{A.2}$$

By inserting the relation given in Equation (A.1) into Equation (A.3), the amount of precursor needed to synthesize 2wt% Pd/Al_2O_3 can be calculated according to Equation (A.4).

$$n_{Pd(NO_3)_2 \cdot 2H_2O} = n_{Pd} \tag{A.3}$$

$$m_{\text{Pd(NO}_3)_2\cdot 2\text{H}_2\text{O}} = \frac{m_{\text{Pd}}}{Mm_{\text{Pd}}} \cdot Mm_{\text{Pd(NO}_3)_2\cdot 2\text{H}_2\text{O}}$$

$$= \frac{0.20g}{106.42\frac{g}{mol}} \cdot 266.46\frac{g}{mol} \qquad \text{(A.4)}$$

$$= 0.5008g$$

A.1.2   Bimetallic Catalyst

Amount of precursors needed to synthesize the bimetallic catalyst of 1.5 wt% Pd and 0.5wt% Ag was calculated according to Equation (A.5). Knowing that $m_{act.material} = m_{\text{Pd}} + m_{\text{Ag}}$, total mass = $m_{\text{Pd}} + m_{\text{Ag}} + m_{\text{Al}_2\text{O}_3}$ and by stoichiometry that $m_{\text{Pd}} = 3m_{\text{Ag}}$, Equation (A.6) can be used to find m_{Pd} and m_{Ag}.

$$wt\% = \frac{m_{act.material}}{m_{total}} \cdot 100\% \qquad \text{(A.5)}$$

$$m_{Ag} = \frac{wt\% \cdot m_{\text{Al}_2\text{O}_3}}{4 \cdot 100\%} \cdot \frac{1}{1 - \frac{wt\%}{100\%}} \qquad \text{(A.6)}$$

Thus, the relation $n_{metal,precursor} = n_{metal}$ gives the amount of precursors needed. The calculation for amount of $AgNO_3$ given in Equation (A.7)-(A.8).

$$m_{Ag} = \frac{2 \cdot 10}{4 \cdot 100} \cdot \frac{1}{1 - \frac{2\%}{100\%}} = 0.05102g \qquad \text{(A.7)}$$

$$m_{AgNO3} = \frac{0.05102}{107.868} \cdot 169.87 = 0.0803g \qquad \text{(A.8)}$$

A.2   Nominal Mass Percentage

The nominal mass percentage of Pd and Ag can be calculated according to Equation A.5. For an element i this corresponds to Equation A.9. The mass, m can be found using Equation A.2.

$$mass\%_{metal,i} = \frac{m_{metal,i}}{m_{total}} \qquad \text{(A.9)}$$

An example calculation is given for Pd/Al_2O_3 in Equation (A.10) and (A.11), using the experimental values of $Pd(NO_3)_2 \cdot 2H_2O$ and γ-Al_2O_3 listed in Table 3.1.

$$m_{\text{Pd}} = \frac{m_{\text{Pd(NO}_3)_2\cdot 2\text{H}_2\text{O}}}{Mm_{\text{Pd(NO}_3)_2\cdot 2\text{H}_2\text{O}}} \cdot Mm_{Pd} \quad [g]$$

$$= 0.2026g \qquad \text{(A.10)}$$

$$mass\%_{Pd} = \frac{0.2062}{0.2062 + 10.003} \cdot 100\%$$
$$= 1.99\%$$

Appendix B

Catalyst Characterization

B.1 X-ray Fluorescence

B.1.1 Deviation

The nominal mass percentages was compared with the XRF results which are summarized in Table 4.1. Equation (B.1) was used to calculate the deviation between the nominal and measured mass percentage. $m\%_{XRF}$ is the mass percentage obtained from the XRF-analysis and $m\%_N$ is the nominal mass percentage, listed in Table 4.1. An example calculation of the deviation of measured mass percentage of Pd in Pd/Al_2O_3 is shown in Equation (B.2).

$$d = \pm \frac{m\%_{XRF} - m\%_N}{m\%_N} \cdot 100\% \tag{B.1}$$

$$d = \pm \frac{1.16 - 1.99}{1.99} \cdot 100\% = -42\% \tag{B.2}$$

Table B.1: Extended table of the results from X-ray Fluorescence analysis.

Catalyst	Pd [mass%]	d [%]	Ag [mass%]	d [%]	K [mass%]	Total$_{act.mat}$ [mass%]	Molar ratio (Ag/Pd)
$Pd/Al_2O_3{}^1$	1.16	-41.7	-	-	0.64	1.16	-
$Pd/Al_2O_3{}^2$	1.15	-42.1	-	-	0.50	1.15	-
$Pd/Al_2O_3{}^a$	1.16	-41.7	-	-	0.64	1.16	-
$Pd/Al_2O_3{}^b$	1.04	-47.7	-	-	0.49	1.04	-
$Pd\text{-}Ag/Al_2O_3{}^1$	0.80	-46.9	0.28	-44.1	0.62	1.08	0.35
$Pd\text{-}Ag/Al_2O_3{}^2$	0.82	-45.3	0.26	-48.2	0.67	1.08	0.32

[1] first analysis.
[2] second analysis.
[a] first pellet.
[b] second pellet.

B.1.2 Standard Deviation

The standard deviation for the XRF analyses are presented in Table B.2-B.4. For Table B.4 and Table B.4, the standard deviation based on several analyses over the same pellet. Also, an additional pellet was made with Pd/Al_2O_3 to investigate the precision of the preparation method. All standard deviations was calculated according to Equation (B.3).

$$\sigma = \sqrt{\frac{\sum_{i=1}^{n}(x_i - \bar{x})^2}{n}} \tag{B.3}$$

Table B.2: Standard deviation of the average of two analyses of the same Pd/Al_2O_3-pellet.

Run	Pd [mass%]	K [mass%]
1	1.159	0.642
2	1.153	0.499
Average Value	1.156 ± 0.003	0.571 ± 0.072

Table B.3: Standard deviation of the average of two different pellets of Pd/Al_2O_3.

Pellet	Pd [mass%]	K [mass%]
1	1.159	0.642
2	1.042	0.488
Average Value	1.100 ± 0.059	0.565 ± 0.077

Table B.4: Standard deviation of the average of two analyses of the same $Pd-Ag/Al_2O_3$-pellet.

Run	Pd [mass%]	Ag [mass%]	K [mass%]
1	0.7957	0.2794	0.6160
2	0.8196	0.2589	0.6676
Average Value	0.8077 ± 0.0120	0.2692 ± 0.0102	0.6418 ± 0.0258

B.2 X-ray Diffraction

The XRD spectra of two analyses over $Pd-Ag/Al_2O_3$ are presented in Figure B.1. Similar features of the analyses are observed and indicate good reproducibility. Figure B.2 show the XRD spectrum of spent $PdAl_2O_3$ and $Pd-AgAl_2O_3$, and SiC which was used as dilutant for catalyst testing. The results demonstrate that only the phases of SiC is detected.
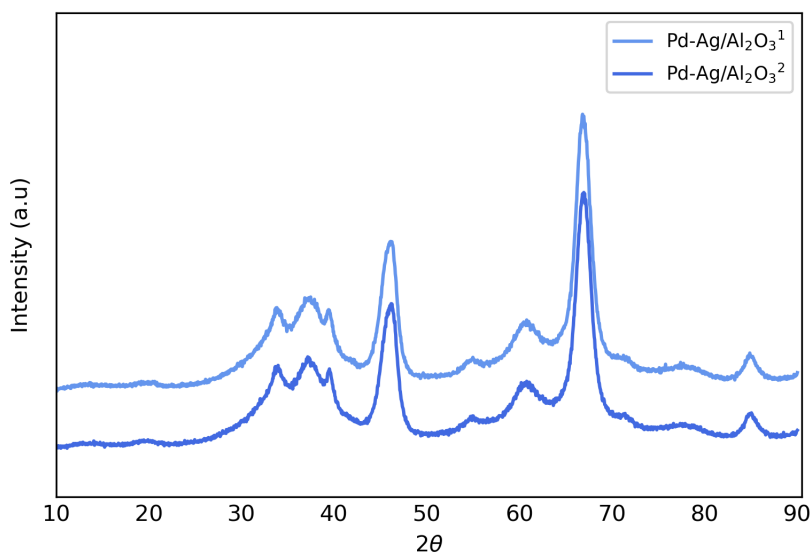
Figure B.1: X-ray diffractogram for two analyses of Pd-Ag/Al$_2$O$_3$.
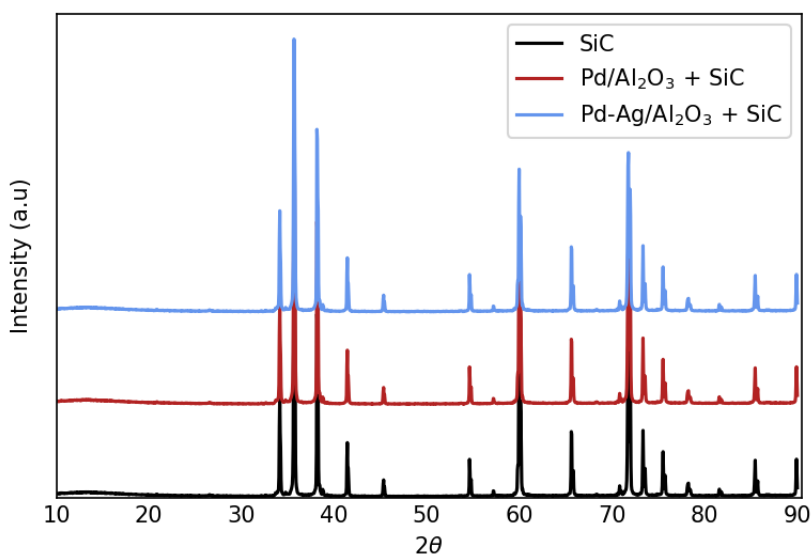
Figure B.2: The X-ray diffractogram of spent catalyst with dilutant, SiC.

B.3   N$_2$ Physisorption

Figure B.3-B.5 shows the N$_2$ adsorption-desorption isotherms and the pore size distribution of γ-Al$_2$O$_3$, Pd/Al$_2$O$_3$ and Pd-Ag/Al$_2$O$_3$ obtained by N$_2$ physisorption analyses.
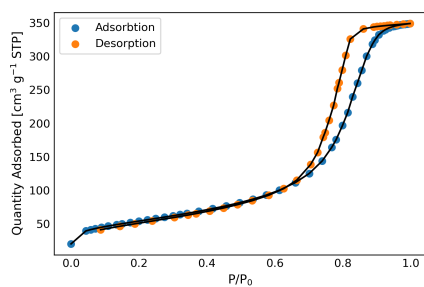
(a) N_2 adsorption-desorption.
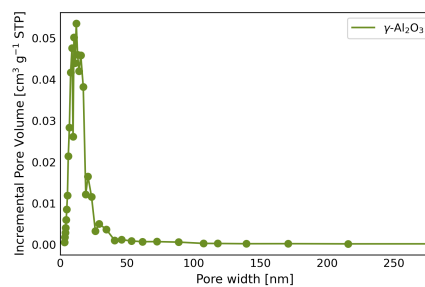
(b) Pore size distribution.

Figure B.3: N_2 adsorption-desorption isotherm **(a)** and pore size distribution **(b)** of γ-Al_2O_3.
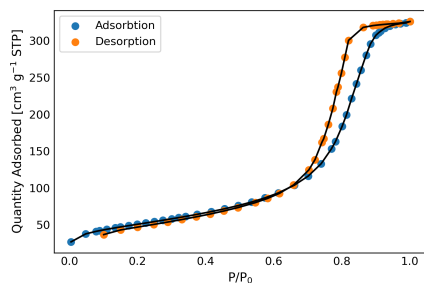
(a) N_2 adsorption-desorption.
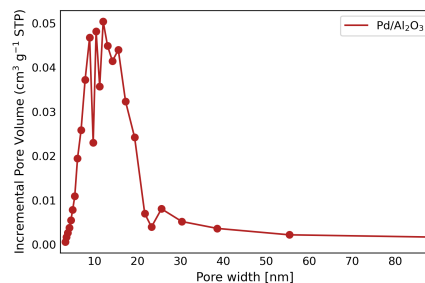
(b) Pore size distribution.

Figure B.4: N_2 adsorption-desorption isotherm **(a)** and pore size distribution **(b)** of Pd/Al_2O_3.
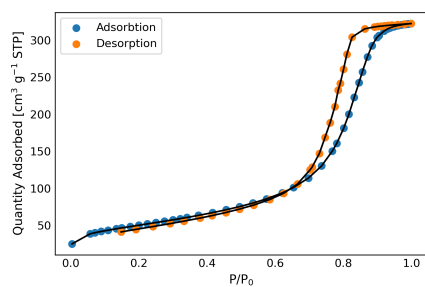
(a) N_2 adsorption-desorption.
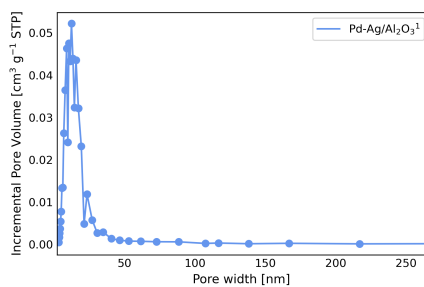
(b) Pore size distribution.
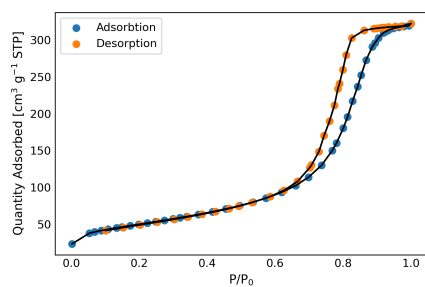
(c) N_2 adsorption-desorption.
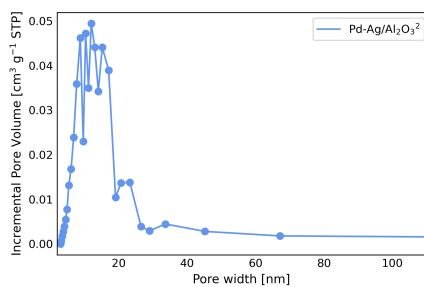
(d) Pore size distribution.

Figure B.5: N_2 adsorption-desorption isotherm **(a)** and pore size distribution **(b)** of Pd-Ag/Al_2O_3.

B.4 Transmission Electron Microscopy

Figure B.6 shows the reference EDS spectrum of palladium and silver.
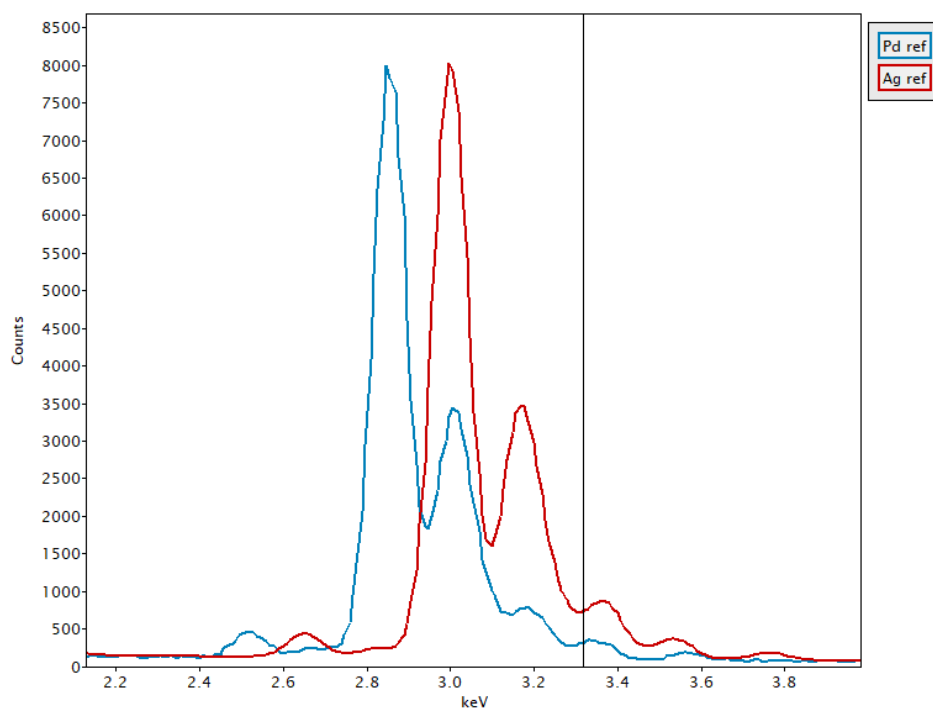
Figure B.6: Reference EDS spectrum of palladium and silver.

B.5 Chemisorption

The instrumental values obtained from CO chemisorption analysis of the catalysts are presented in Table B.5.

Table B.5: The dispersion, crystallite size, metal surface area and quantity adsorbed CO measured by CO chemisorption. The analysis conditions are listed in Table 3.6.

Catalyst	Dispersion [%]	Crystallite Size [nm]	Metal Surface Area m^2/g_{sample}	Quantity adsorbed [cm^3/g STP]
Pd/Al$_2$O$_3$	36.9192	3.2895	3.03493	0.7777
Pd-Ag/Al$_2$O$_3$	16.1452	1.4706	7.00792	0.5434

B.5.1 Calculation of Dispersion and Crystallite Size

The dispersion, specific metal surface area and crystallite size of palladium was calculated according to Equation (9)-(12). The calculations for Pd-Ag/Al$_2$O$_3$ are shown in (B.4)- (B.7). Note that V_M from the analysis is the quantity adsorbed *per gram sample*, i.e. m is excluded from the expressions.

$$
\begin{aligned}
D &= \frac{V_m \cdot F \cdot M_m}{wt\%_{metal} \cdot V_{molar}} \cdot 100 \quad [\%] \\
&= \frac{0.5434 \cdot 2 \cdot 106.4}{0.015 \cdot 22414} \cdot 100\% \\
&= 34.39\%
\end{aligned}
\tag{B.4}
$$

$$
\begin{aligned}
A &= \frac{V_m}{22414} N_A n a_m \frac{100}{wt} \quad [m^2 g^{-1} metal] \\
A &= \frac{0.5434}{22414} 6.022 \cdot 10^{23} \cdot 2 \cdot 0.0787 \cdot 10^{-18} \cdot \frac{100}{1.5} \ m^2 g^{-1} metal \\
&= 153.199 \ m^2 g^{-1} metal
\end{aligned}
\tag{B.5}
$$

$$
\begin{aligned}
v_m &= \frac{M_m}{\rho N_A} \quad [cm^3] \\
&= \frac{106.4}{12.02 \cdot 6.022 \cdot 10^{23}} \ cm^3 \\
&= 1.4702 \cdot 10^{-23} \ cm^3 \\
&= 0.0147 \ nm^3
\end{aligned}
\tag{B.6}
$$

$$
\begin{aligned}
d_{va} &= \frac{6(v_m/a_m)}{D} \quad [nm] \\
&= \frac{6(0.0147/0.0787)}{0.3439} \ nm \\
&= 3.26 \ nm
\end{aligned}
\tag{B.7}
$$

B.6   Temperature Programmed Reduction

The TPR-profiles of Pd/Al_2O_3 and $Pd\text{-}Ag/Al_2O_3$ are presented in Figure B.7. The area of the negative peaks was found using trapezoidal numerical integration in Python and the variation of this area is illustrated in Figure B.8.
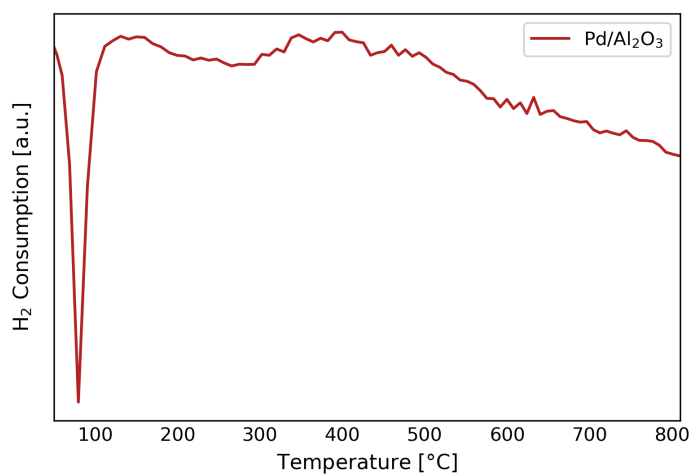
(a) The H_2-TPR profile of Pd/Al$_2$O$_3$.
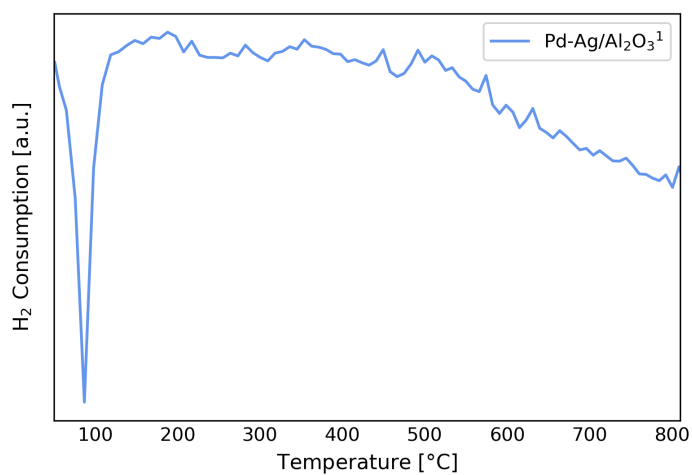
(b) The H_2-TPR profile of Pd-Ag/Al$_2$O$_3$.
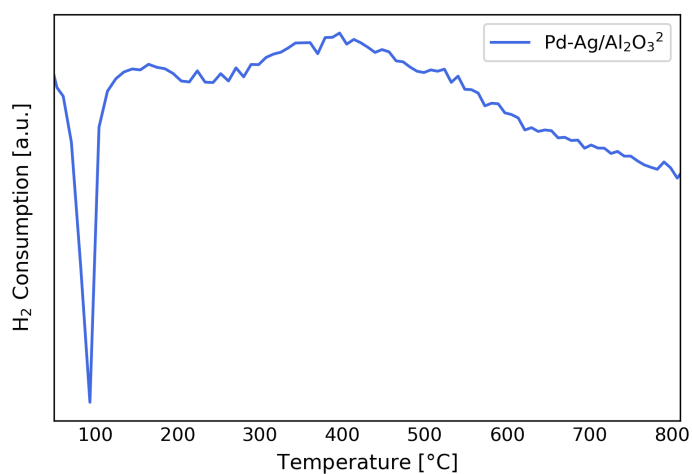
(c) The second H_2-TPR profile of Pd-Ag/Al$_2$O$_3$.

Figure B.7: The result from one TPR analysis of Pd/Al$_2$O$_3$ and two TPR analysis of Pd-Ag/Al$_2$O$_3$. All analysis was performed under identical conditions. The analysis conditions can be reviewed in Section 3.3.6
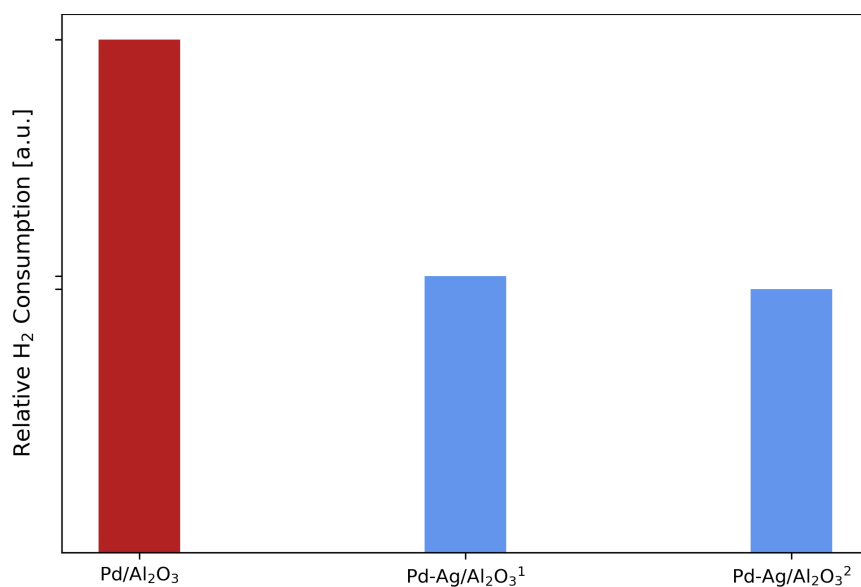
Figure B.8: The calculated area of the negative peak in TPR analyses of Pd/Al$_2$O$_3$(red) and Pd-Ag/Al$_2$O$_3$(blue). [1,2] indicates first and second analysis, respectively.

B.6.1   Deviation

The TPR patterns of two analysis of Pd-Ag/Al$_2$O$_3$ are presented in Figure B.9. Equation (B.8) was used to calculate the deviation, *d*, of the area of the negative peak, from the first and second TPR analysis of Pd-Ag/Al$_2$O$_3$.
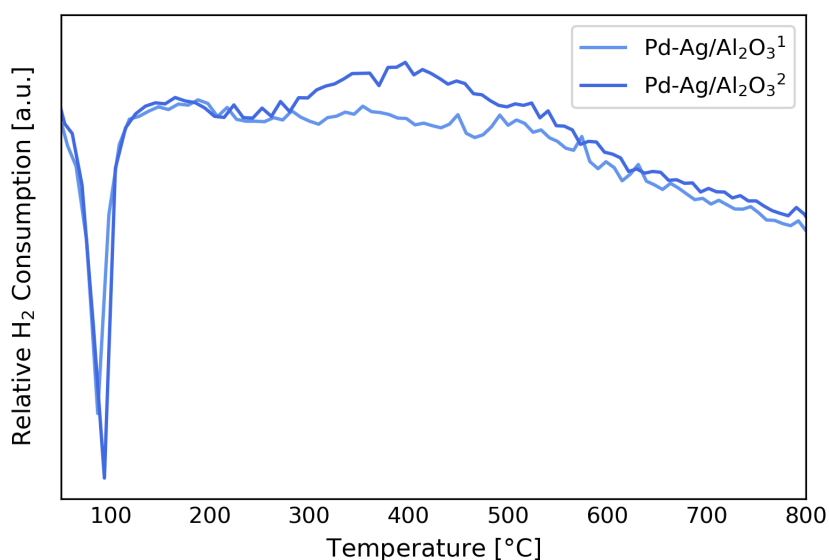
Figure B.9: The H$_2$-TPR profile of two analyses of Pd-Ag/Al$_2$O$_3$.

$$d = \pm\frac{(S_{1,TPR} - S_{2,TPR})}{S_{1,TPR}} \cdot 100\%$$
$$= \pm\frac{(775 - 739)}{775} \cdot 100\%$$
$$= 5\%$$

(B.8)

Appendix C

Catalyst Activity

C.1 Calculation of Reaction Rate

The reaction rate was calculated according to Equation (29). The reaction rates were calculated at a temperature of 300 °C and 150 °C for methane and CO oxidation, respectively. An example calculation for the first reaction cycle over Pd/Al_2O_3 is shown in Equation (C.1).

$$
\begin{aligned}
r &= \frac{GHSV \cdot X \cdot C_{A0}}{V_{molar}} \quad [\frac{mol}{h \cdot g_{cat}}] \\
&= \frac{59821 \cdot 0.6747 \cdot 0.02}{22414} \frac{mol}{h \cdot g_{cat}} \\
&= 0.036 \frac{mol}{h \cdot g_{cat}}
\end{aligned}
\tag{C.1}
$$

C.2 Methane Oxidation

Table C.1 presents the temperatures required for different levels of conversion for all reaction cycles in methane oxidation. The temperatures were estimated using polynomial regression in Python.

Table C.1: Temperatures at different levels of conversion for all reaction cycles in methane oxidation. The reaction conditions for all runs were 4 ml min^{-1} CH$_4$, 95.25 ml min^{-1} O$_2$ and 100.75 ml min^{-1} N$_2$, except for those denoted $_{10\%H_2O}$ with 10% H$_2$O included in the feed. Then the flow of N$_2$ was balanced total flow was 200 ml min^{-1} for all runs. All temperatures were estimated using a polynomial fit function in Python.

Catalyst	Reaction Cycle		$T_{10\%}$ [°C]	$T_{20\%}$ [°C]	$T_{30\%}$ [°C]	$T_{40\%}$ [°C]	$T_{50\%}$ [°C]	$T_{90\%}$ [°C]	$T_{100\%}$ [°C]
Pd/Al$_2$O$_3$	1	Heating	254	264	272	279	287	317	368
		Cooling	310	333	349	362	374	406	421
	2	Heating	311	337	350	362	374	417	443
		Cooling	327	354	373	385	397	435	464
	3	Heating	331	357	375	388	400	442	462
		Cooling	338	364	381	397	407	448	465
Pd/Al$_2$O$_3$	1	Heating	250	269	277	284	291	321	370
		Cooling	317	339	353	362	371	397	418
	$2_{10\%H_2O}$	Heating	373	393	407	421	428	464	495
		Cooling	417	434	448	455	462	489	513
	3	Heating	337	363	376	386	396	430	465
		Cooling	348	370	384	396	408	445	465
Pd-Ag/Al$_2$O$_3$	1	Heating	264	276	288	301	313	342	404
		Cooling	311	335	352	368	379	423	450
	2	Heating	271	291	312	332	350	411	455
		Cooling	338	363	379	394	405	457	475
	3	Heating	276	305	328	348	365	434	472
		Cooling	341	369	390	403	416	465	496
Pd-Ag/Al$_2$O$_3$	1	Heating	260	269	279	288	297	334	361
		Cooling	315	335	347	359	370	403	414
	$2_{10\%H_2O}$	Heating	380	397	410	419	426	468	504
		Cooling	416	435	445	455	464	490	507
	3	Heating	337	362	374	386	395	432	456
		Cooling	352	374	389	401	413	449	480

C.2.1 Arrhenius Plot

Arrhenius plots found for all reaction cycles over Pd/Al$_2$O$_3$ and Figure Pd-Ag/Al$_2$O$_3$ in methane oxidation are presented in Figure C.1 and C.2. The Arrhenius plot was obtained by plotting ln(-ln(1-X$_A$)) against 1000/T for conversion levels 10-50%. The temperatures necessary for these levels of conversion were obtained by a polynomial fit function of the data set obtained from the μ-GC and the temperature log. The apparent activation energy was found by multiplying the slope of the line, (-E_A/R) with the negative gas constant, -R. The principle and method of the Arrhenius plot are presented in Section 2.5.4.

(a) Cycle 1, Pd/Al$_2$O$_3$

(b) Cycle 2, Pd/Al$_2$O$_3$

(c) Cycle 3, Pd/Al$_2$O$_3$

(d) Dry experiment, 1, Pd/Al$_2$O$_3$

(e) Wet experiment, Pd/Al$_2$O$_3$

(f) Dry experiment, 2, Pd/Al$_2$O$_3$
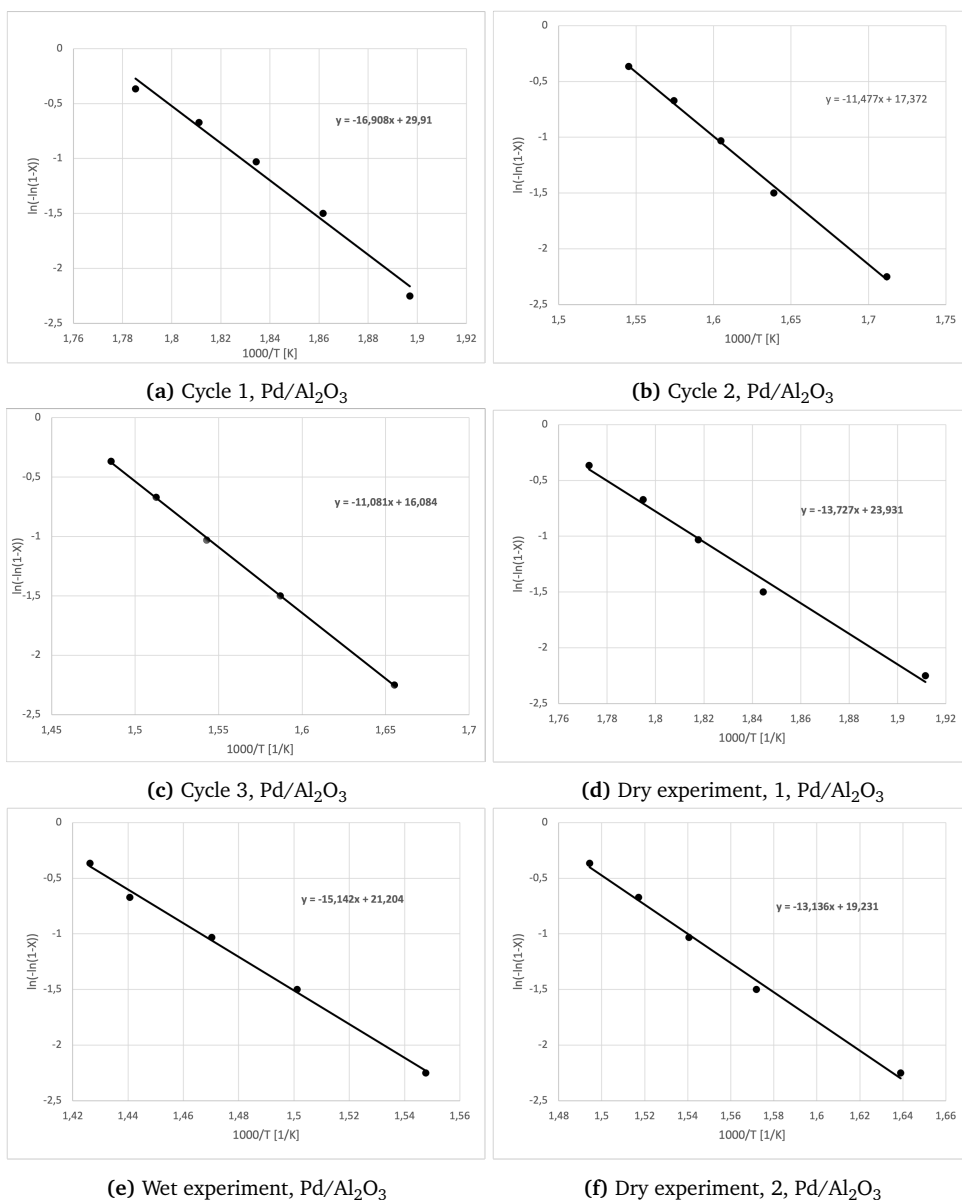
Figure C.1: Arrhenius plots for methane oxidation over Pd/Al$_2$O$_3$. The equation of the line is on the form $ln(-ln(1-X)) = ln(A) + -E_A/R \cdot 1/T$. The activation energy, E_A, is then found by multiplying the slope of the line, $-E_A/R$ with the negative gas constant, -R.

(a) Cycle 1, Pd-Ag/Al$_2$O$_3$

(b) Cycle 2, Pd-Ag/Al$_2$O$_3$

(c) Cycle 3, Pd-Ag/Al$_2$O$_3$

(d) Dry experiment, 1, Pd-Ag/Al$_2$O$_3$

(e) Wet experiment, Pd-Ag/Al$_2$O$_3$

(f) Dry experiment, 2, Pd-Ag/Al$_2$O$_3$
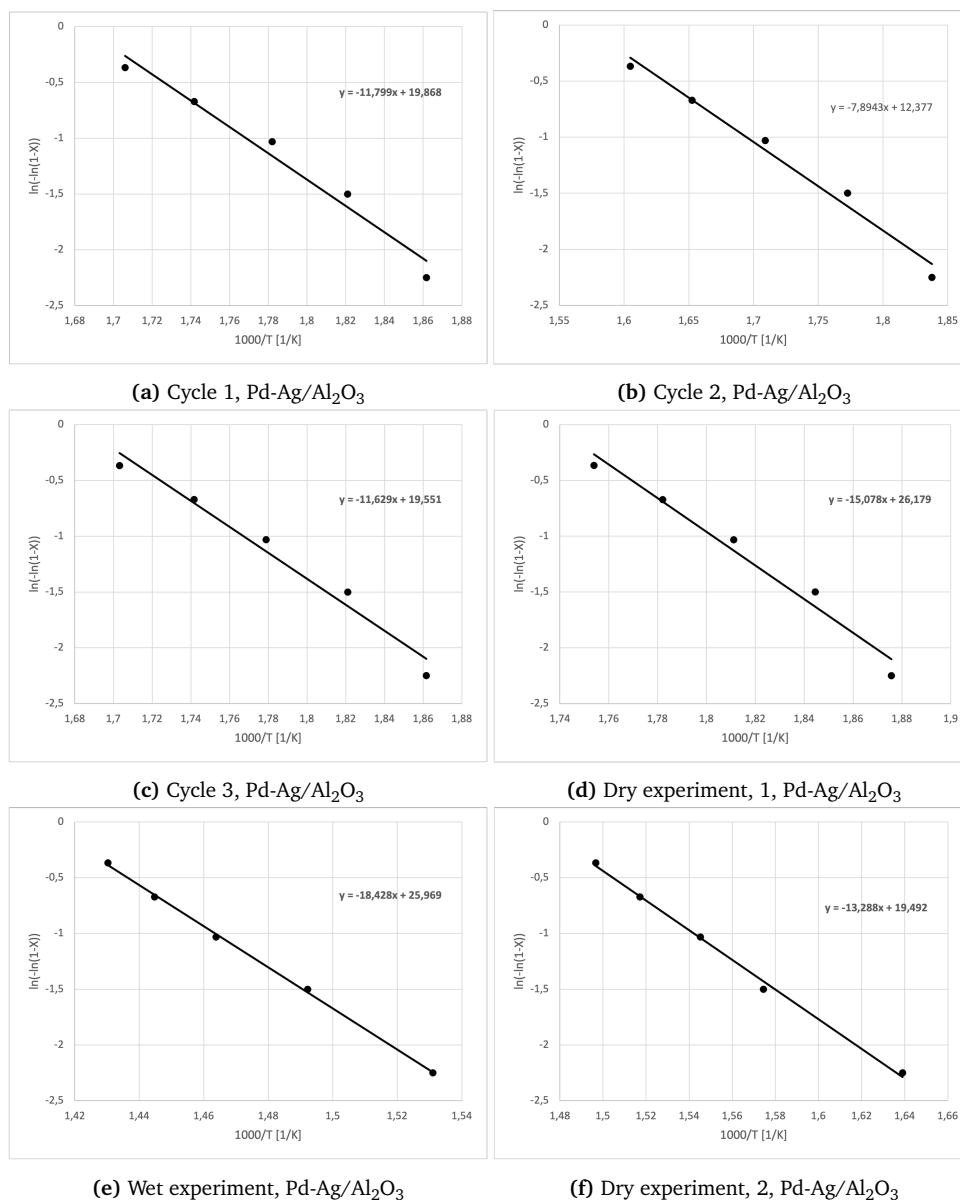
Figure C.2: Arrhenius plots for methane oxidation over Pd-Ag/Al$_2$O$_3$. The equation of the line is on the form $ln(-ln(1 - X)) = ln(A) + -E_A/R \cdot 1/T$. The activation energy, E_A, is then found by multiplying the slope of the line, $-E_A/R$ with the negative gas constant, -R.

C.2.2   Carbon Balance

The carbon balance deviation for all reaction runs in methane oxidation over Pd/Al$_2$O$_3$ and Pd-Ag/Al$_2$O$_3$ is presented in Figure C.3 and C.4. The carbon balance was calculated according to Equation (26) presented in Section 2.5.2. The standard deviation of the carbon balance for all reaction cycles in methane oxidation is presented in Table C.2 and was calculated according to Equation (B.3).

(a) Cycle 1, Pd/Al$_2$O$_3$

(b) Cycle 2, Pd/Al$_2$O$_3$

(c) Cycle 3, Pd/Al$_2$O$_3$

(d) Dry experiment, 1, Pd/Al$_2$O$_3$

(e) Wet experiment, Pd/Al$_2$O$_3$

(f) Dry experiment, 2, Pd/Al$_2$O$_3$
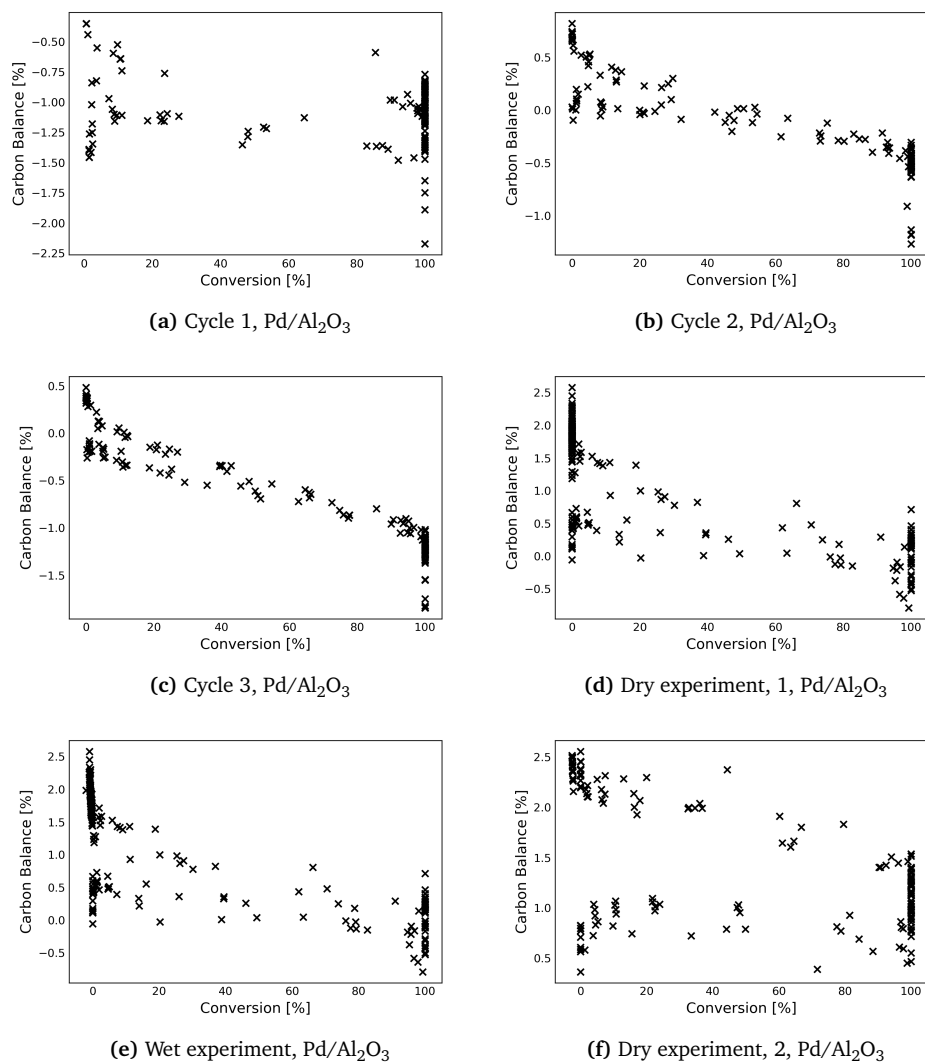
Figure C.3: The carbon balance deviation plotted against the conversion of methane over Pd/Al$_2$O$_3$. Equation (23) and (26) was used to calculate the methane conversion and carbon error balance, respectively.

(a) Cycle 1, Pd-Ag/Al$_2$O$_3$

(b) Cycle 2, Pd-Ag/Al$_2$O$_3$

(c) Cycle 3, Pd-Ag/Al$_2$O$_3$

(d) Dry experiment, 1, Pd-Ag/Al$_2$O$_3$

(e) Wet experiment, Pd-Ag/Al$_2$O$_3$

(f) Dry experiment, 2, Pd-Ag/Al$_2$O$_3$
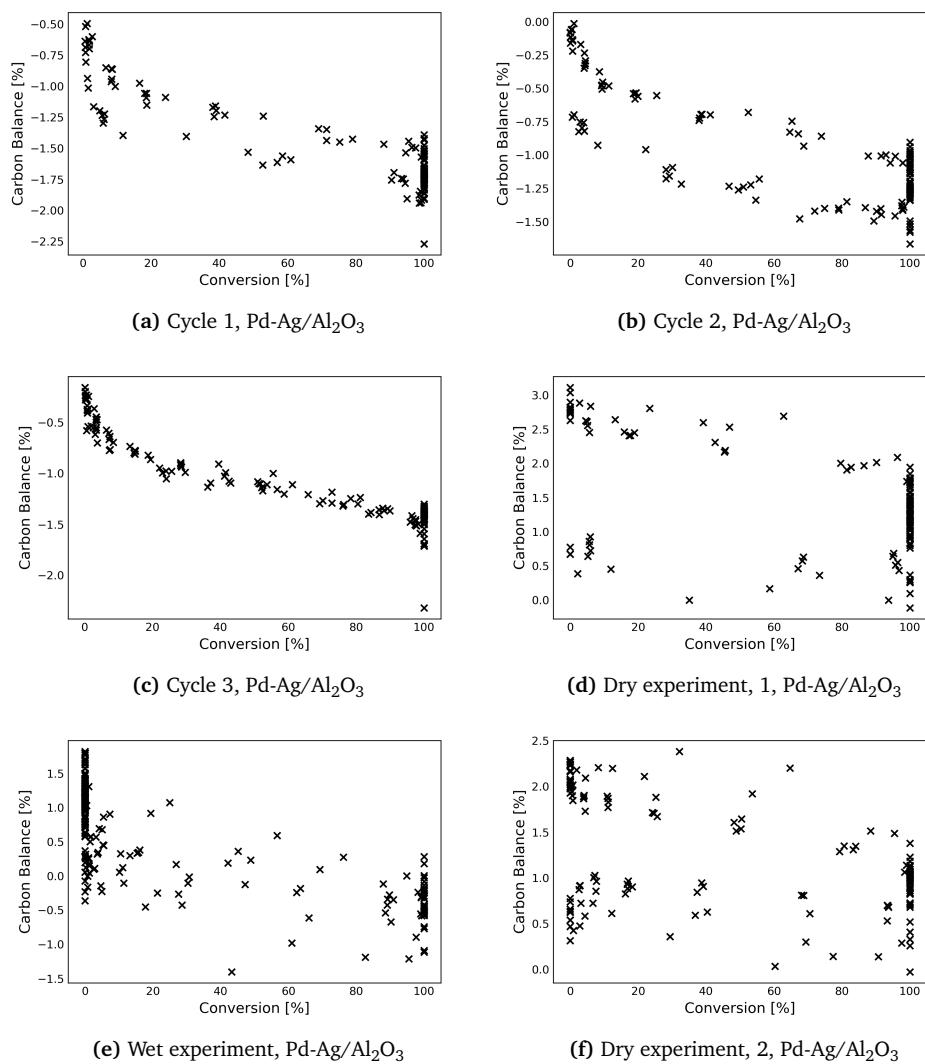
Figure C.4: The carbon balance deviation plotted against the conversion of methane over Pd-Ag/Al$_2$O$_3$. Equation (23) and (26) was used to calculate the methane conversion and carbon error balance, respectively.

Table C.2: Standard deviation of the average of the carbon balance.

Catalyst	Run	Average [%]	Standard Deviation [%]
Pd/Al_2O_3	1	-1.08	0.28
	2	-0.18	0.42
	3	-0.65	0.57
Pd/Al_2O_3	1	0.16	0.86
	$2_{10\%H_2O}$	1.09	0.86
	3	1.32	0.58
$Pd\text{-}Ag/Al_2O_3$	1	-1.49	0.37
	2	-0.97	0.41
	3	-1.11	0.42
$Pd\text{-}Ag/Al_2O_3$	1	1.44	0.76
	$2_{10\%H_2O}$	1.15	0.58
	3	0.63	0.73

C.3 CO Oxidation

Table C.3: Temperatures at different levels of conversion for all reaction cycles of CO oxidation. All temperatures were estimated using a polynomial regression in Python, presented in Appendix D.

Catalyst	Feed mol% CO	Reaction Cycle		$T_{10\%}$ [°C]	$T_{20\%}$ [°C]	$T_{30\%}$ [°C]	$T_{40\%}$ [°C]	$T_{50\%}$ [°C]	$T_{90\%}$ [°C]	$T_{100\%}$ [°C]
Pd/Al_2O_3	2%	1	Heating	111	116	122	128	134	156	162
			Cooling	109	115	121	127	133	157	163
Pd/Al_2O_3	5%	2	Heating	160	174	178	181	184	197	200
			Cooling	50	52	55	58	61	72	75
Pd/Al_2O_3	5%	3	Heating	171	189	192	194	196	206	208
			Cooling	51	52	56	61	65	84	107
$Pd\text{-}Ag/Al_2O_3$	2%	1	Heating	133	163	170	176	183	209	216
			Cooling	110	117	123	129	136	161	167
$Pd\text{-}Ag/Al_2O_3^{set}$	5%	2	Heating	163	176	179	182	185	197	200
			Cooling	55	60	65	70	72	74.5	75
$Pd\text{-}Ag/Al_2O_3^{bed}$	5%	2	Heating	176	194	197	200	203	214	217
			Cooling	54	60	65	70	77	106	112
$Pd\text{-}Ag/Al_2O_3$	5%	3	Heating	179	193	196	199	202	215	218
			Cooling	61	68	74	79	85	107	112

C.3.1 Arrhenius Plots

Arrhenius plots found for all reaction cycles over Pd/Al_2O_3 and $Pd\text{-}Ag/Al_2O_3$ in CO oxidation, calculated for 20-50% levels of conversion.

(a) 2% CO,1, Pd/Al$_2$O$_3$

(b) 5% CO, 2, Pd/Al$_2$O$_3$

(c) 5% CO, 3, Pd/Al$_2$O$_3$
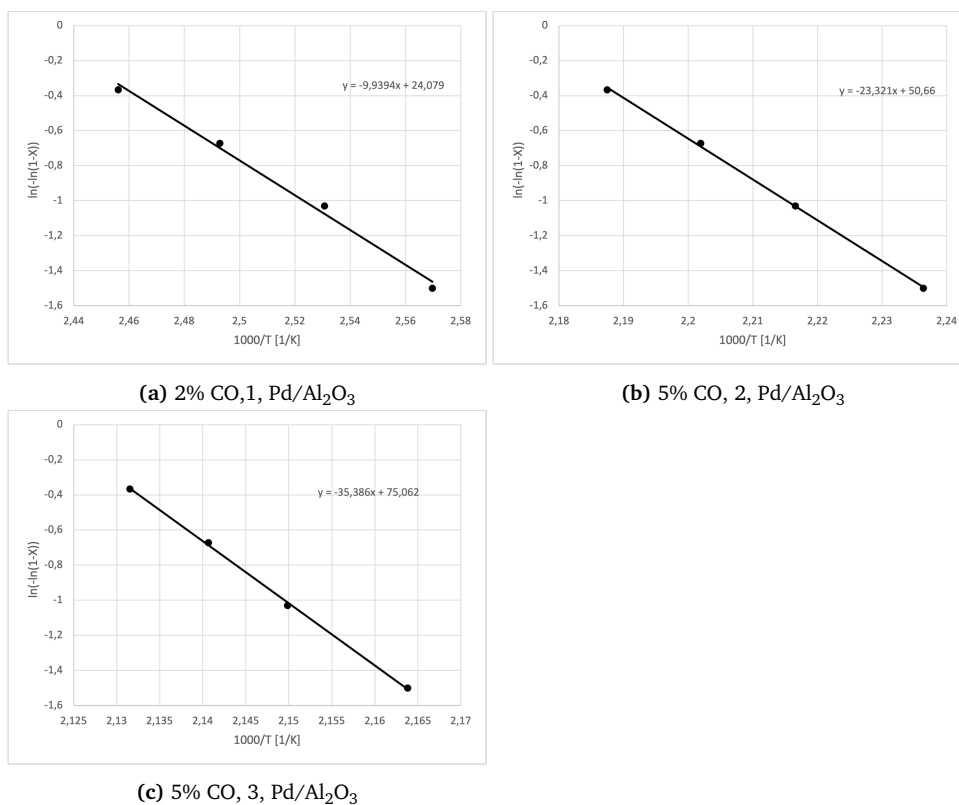
Figure C.5: Arrhenius plots for CO oxidation over Pd/Al$_2$O$_3$. The equation of the line is on the form $ln(-ln(1-X)) = ln(A) + -E_A/R \cdot 1/T$. The activation energy, E_A, is then found by multiplying the slope of the line, $-E_A/R$ with the negative gas constant, $-R$.

(a) 2% CO,1, Pd-Ag/Al$_2$O$_3$

(b) 5% CO, 2, Pd-Ag/Al$_2$O$_3$ (Set-point T)

(c) 5% CO, 2, Pd-Ag/Al$_2$O$_3$(Catalyst bed T)

(d) 5% CO, 3, Pd-Ag/Al$_2$O$_3$
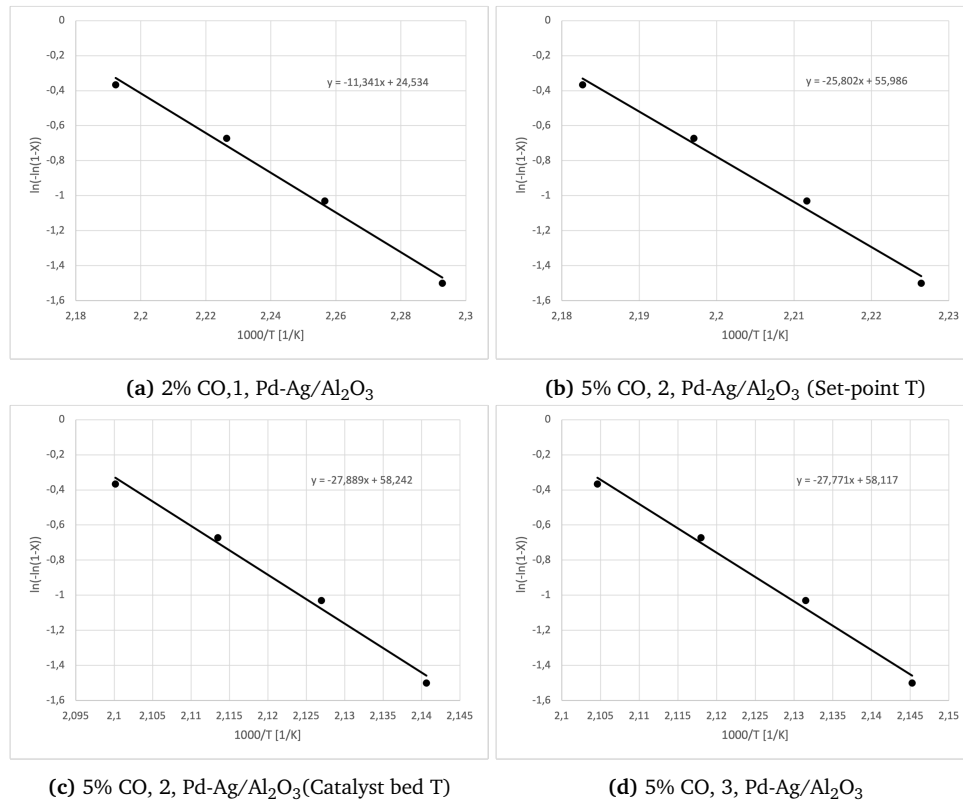
Figure C.6: Arrhenius plots for CO oxidation over Pd-Ag/Al$_2$O$_3$. The equation of the line is on the form $ln(-ln(1 - X)) = ln(A) + -E_A/R \cdot 1/T$. The activation energy, E_A, is then found by multiplying the slope of the line, $-E_A/R$ with the negative gas constant, -R.

C.3.2 Carbon Balance

The carbon balance error for all reaction runs in CO oxidation over Pd/Al$_2$O$_3$ and Pd-Ag/Al$_2$O$_3$ is presented in Figure C.3 and C.4. The carbon error was calculated according to Equation (26) presented in Section 2.5.2. The standard deviation of the carbon balance is presented in Table C.4 and were calculated according to Equation (B.3).

(a) 2% CO, Pd/Al$_2$O$_3$

(b) 5% CO, 1, Pd-Al$_2$O$_3$

(c) 5% CO, 3, Pd-Al$_2$O$_3$

(d) 2% CO, Pd-Ag/Al$_2$O$_3$

(e) 5% CO, 1, Pd-Ag/Al$_2$O$_3$

(f) 5% CO, 3, Pd-Ag/Al$_2$O$_3$
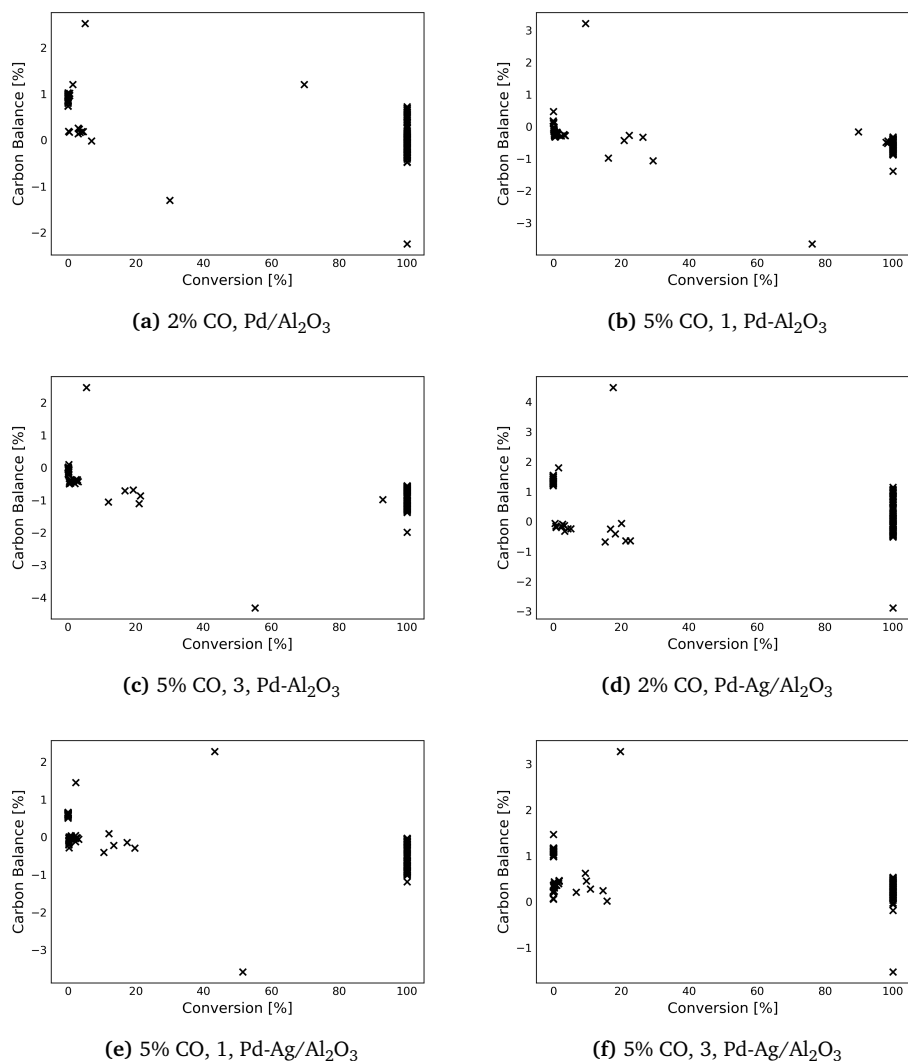
Figure C.7: The carbon error plotted against the conversion of CO over Pd/Al$_2$O$_3$ and Pd-Ag/Al$_2$O$_3$. Equation (23) and (26) was used to calculate the CO conversion and carbon error balance, respectively.

Table C.4: Standard deviation of the average of the carbon balance.

Catalyst	Feed [mol%]	Average [%]	Standard Deviation [%]
Pd/Al$_2$O$_3$	2%	0.16	0.52
	5%	-0.50	0.49
	5%	-0.81	0.54
Pd-Ag/Al$_2$O$_3$	2%	0.28	0.77
	5%	-0.42	0.55
	5%	-0.29	0.37

C.4 Blank Test

Table C.5: Result from blank test performed in Rig 2.9. Reaction conditions: F_{CH_4} = 4 ml min^{-1}, F_{N_2} = 100.75 ml min^{-1}, F_{Air} = 95.25 ml min^{-1} and amount of SiC = 1.5 g.

Temperature [$^\circ$ C]	Conversion [%]
200	0.03
250	0.00
300	0.00
325	0.00
350	0.00
375	0.00
400	0.11
425	0.42
450	0.87
475	1.42
500	2.03
525	2.43
550	2.49
525	1.60
500	0.84
475	0.45
450	0.00
425	0.00
400	0.00
375	0.00
350	0.00
325	0.00
300	0.00
250	0.00
200	0.00
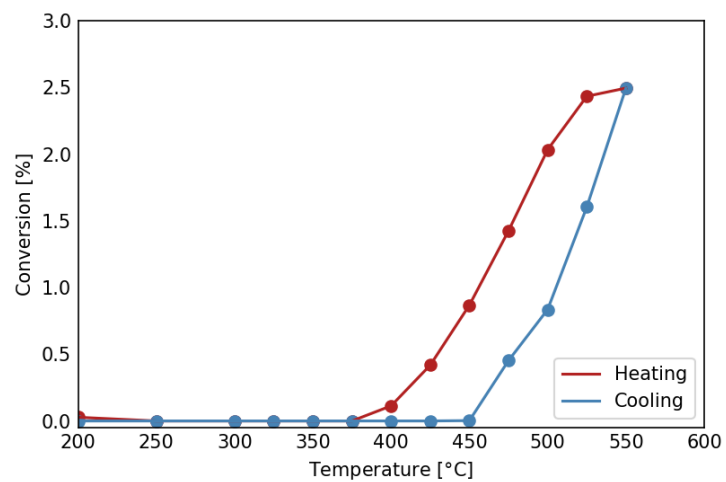
Figure C.8: Conversion as function of temperature over 1.5 g SiC (inert). Reaction conditions: F_{CH_4} = 4 ml min^{-1}, F_{N_2} = 100.75 ml min^{-1}, F_{Air} = 95.25 ml min^{-1} and amount of SiC = 1.5 g.

Appendix D

Python Script

```python
import pandas as pd
import matplotlib.pyplot as plt
import math
import numpy as np
from sklearn.metrics import r2_score

xls = pd.read_excel('/Users/sunnivaskogheim/Documents/Masteroppgave/
    Rig/samlet-resultat.xlsx',header = None, sheet_name = "Heating",
    indexcol = 0)


temp = xls[1]
conversion = xls[2]



model = np.poly1d(np.polyfit(temp, conversion, deg=5))
myline = np.linspace(50,560)



#Find temperature at given conversion, C = 10,20,30,40,50,90,100%
conv = [0.1,0.2,0.3,0.4,0.5,0.9,0.9999999]



for x in conv:
    x_value = np.interp(x, conversion, temp)
    print(x_value)

#Conversion at 300 degrees for reaction rate calculations
t = [300]
for y in t:
    y_value = np.interp(y, temp, conversion)
    print(y_value)
```

Appendix E

Risk Assessment

The risk assessment with safety measures and risks associated with this research is presented in the following chapter. It should be noted that the risk assessment also contain the safety measures and risks of the specialization project during the autumn of 2021 [9]. The risk assessment can be reviewed in the portal of risk assessment with ID-number 40054.

E.1 Risk Assessment

Detailed Risk Report

ID	40054	Status	Date
Risk Area	Risikovurdering: Helse, miljø og sikkerhet (HMS)	Created	07.09.2020
Created by	Sunniva Skogheim	Assessment started	07.09.2020
Responsible	Sunniva Skogheim	Measures decided	
		Closed	

Risk Assessment:
CAT, Master student, 2021, Sunniva Skogheim

Valid from-to date:
9/7/2020 - 9/7/2023

Location:
Kjemiblokk 5

Goal / purpose
The objective is to test the catalysts Pd/Al2O3 and Pd-Ag/Al2O3. They will be synthetized , characterized and tested in methane and CO oxidation.

Background
Risk assessment of materials and the work that is going to be completed.

Description and limitations

Pd/Al2O3 and Pd-Ag/Al2O3 catalyst:
- The support will be prepared for synthesis by heating of the material in a high temperature furnace at 600 degress for 6 hours and with a heating rate of 5 degrees/min. Further it will be sieved to obtain a particle size of 75-150 um.
- Incipient wetness impregnation will be used for both catalysts. Pd(II)nitrate dihydrate will be used to source Pd. The salt will be dissolved in deionized water before it is dripped over the support using a pipette. For Pd-Ag/Al2O3, Ag(NO3) will be used to source Ag. The two salts will be dissolved in deionized water before they are dripped over the alumina support.
- The catalysts will be dried in an oven at 120 degrees for 3 hours before they are calcinated at 500 degrees for two hours. The heating rate of the calcination will be 5 degrees/min.

The catalysts will be characterized using the characterization techniques: X-ray fluorescence, X-ray Diffraction, N2-Physisorption, TEM, TPR and Chemisorption.

Rooms that will be used for characterization:
XRF: K5-425
XRD: K2-113
Raman spectroscopy: K5-427
N2-physisorption: K5-425
TPX: Chemistry hall D
- Temperature range 25-800 degrees
- H2/Ar: 7% H2 in Ar
- Chemistry Hall D 1
Chemisorption: K5-420
-TEM

Catalyst activity in rig 2.9 chemistry hall D 2:
- N2, inert
- CH4
- Air
- H2 for leakage test
- He for GC
- CO
- Temperature: 200-550 degrees
- Temperature program: 550 degrees, 5 degrees/min

Measures against COVID 19:
1) Routines
- Keep at least 1m distance to each other
- Wash hands regularly
- Disinfect contact surfaces before and after acitivity

Safety measures related to work in rig 2.9/Hall D:
- In the case of gas/fire alarm as a result of work in another rig or project, leave the room and the person responsible must notified.

Prerequesites, assumptions and simplifications

I assume that the equipment is approved and risk assessed separately.

COVID-19 measures:
1)   Switch off procedure for MY SET-UP (Rig 2.9, Hall D) –
-Close all gas valves
-Turn of the heater
-Evacuate out through the nearest emergency exit

2)   Safety measures related to spread of covid19 infection:
Avoid touching the face
Disinfection before and after with ethanol/solvent on all surfaces you are in contact with (door knob – card reader with code panel – if you use common equipment - keyboard – mouse – screen – desk)
Keep 1m distance from colleagues
Use nitrile gloves when touching shared lab set-ups and equipment
Wash hands as often as possible
Update the IKP Lab activity 2020 Teams excel sheet about weekly planning of experiments. A week in advance.
Taking the bus to campus should be noted.

3) Working alone
- When working alone, the working-alone alarm should be used. In addition, the after-hour agreement was signed and followed.

Attachments
nickelnitratehexahydrate.pdf
oxygen.pdf
helium.pdf
methane.pdf
coboltnitratehexahydrate.pdf
hydrogen.pdf
reconstruction PLAN 11_06_2020[2].pdf
How to run an experiment on Rig 29.docx
Methane oxidation during wet reaction conditions[2].docx
Rig - 2_9_information_Henrik_Schuster_Aug_2019[2].pdf
19156632_286_f737e87b8207d86945272007b4838feb.pdf
Laboratory work after normal working hours.jpg
18488644_286_33996aa798ec69b2e18587b8bb893a5d.pdf
SDS15950636.pdf
17875074_286_3451c54553f8c813c27f2cdfbb91c366.pdf
19156632_286_f737e87b8207d86945272007b4838feb.pdf
19458714_286_ebb8cb04519a35dc3974dcb15a3a9b62.pdf
17875074_286_3451c54553f8c813c27f2cdfbb91c366 (3).pdf

References
[Ingen registreringer]

Summary, result and final evaluation

The summary presents an overview of hazards and incidents, in addtition to risk result for each consequence area.

Hazard:	Catalyst synthesis

Incident:	Ni(NO3)2*6H20

Consequence area:	Helse	Risk before measures:	🟡 Risiko after measures:	⚪
	Ytre miljø	Risk before measures:	🟡 Risiko after measures:	⚪

Incident:	Co(NO3)2*6H2O

Consequence area:	Helse	Risk before measures:	🟡 Risiko after measures:	⚪
	Ytre miljø	Risk before measures:	🟡 Risiko after measures:	⚪

Incident:	Kaliumhydroxide

Consequence area:	Helse	Risk before measures:	🟡 Risiko after measures:	⚪
	Materielle verdier	Risk before measures:	🟡 Risiko after measures:	⚪

Incident:	Pd(NO3)2 2*H2O

Consequence area:	Helse	Risk before measures:	🟡 Risiko after measures:	⚪
	Materielle verdier	Risk before measures:	🟡 Risiko after measures:	⚪

Incident:	Ag(NO3)

Consequence area:	Helse	Risk before measures:	🟡 Risiko after measures:	⚪
	Ytre miljø	Risk before measures:	🟡 Risiko after measures:	⚪
	Materielle verdier	Risk before measures:	🟡 Risiko after measures:	⚪

Incident:	Al2O3

Consequence area:	Helse	Risk before measures:	🟢 Risiko after measures:	⚪

Detailed Risk Report

Hazard:	**Catalyst synthesis**			
Incident:	**Al2O3**			
	Materielle verdier	Risk before measures:	🟢 Risiko after measures:	⚪

Hazard:	**TPR**			
Incident:	**Gas Leakage**			
Consequence area:	Helse	Risk before measures:	🟡 Risiko after measures:	⚪
	Materielle verdier	Risk before measures:	🟡 Risiko after measures:	⚪
Incident:	**Spill of samples**			
Consequence area:	Helse	Risk before measures:	🟡 Risiko after measures:	⚪

Hazard:	**Raman spectroscopy**			
Incident:	**Eye damage**			
Consequence area:	Helse	Risk before measures:	🟢 Risiko after measures:	⚪
Incident:	**Chemical exposure during sample preparation**			
Consequence area:	Helse	Risk before measures:	🟡 Risiko after measures:	⚪

Hazard:	**X-ray Diffraction**			
Incident:	**Exposure of chemicals during sample preparation**			
Consequence area:	Helse	Risk before measures:	🟡 Risiko after measures:	⚪

Norges teknisk-naturvitenskapelige universitet (NTNU)   **Print date:**   **Printed by:**   **Page:**

Unntatt offentlighet jf. Offentlighetsloven § 14   13.06.2021   Sunniva Skogheim   5/30

Detailed Risk Report

Hazard:	**COVID-19**				
Incident:	**COVID-19 infection**				
Consequence area:	Helse	Risk before measures:		Risiko after measures:	

Hazard:	**X-ray fluorescence**				
Incident:	**Exposure of chemicals during sample preparation**				
Consequence area:	Helse	Risk before measures:		Risiko after measures:	

Hazard:	**N2-physisorption**				
Incident:	**Liquid N2-spill**				
Consequence area:	Helse	Risk before measures:		Risiko after measures:	

Hazard:	**Rig**				
Incident:	**Gas leakage**				
Consequence area:	Helse	Risk before measures:		Risiko after measures:	
	Ytre miljø	Risk before measures:		Risiko after measures:	
	Materielle verdier	Risk before measures:		Risiko after measures:	
Incident:	**Skin burn**				
Consequence area:	Helse	Risk before measures:		Risiko after measures:	

Hazard:	**TGA**				
Incident:	**Gas leakage**				
Consequence area:	Helse	Risk before measures:		Risiko after measures:	
	Materielle verdier	Risk before measures:		Risiko after measures:	

☐   **Detailed Risk Report**

Hazard:	**Chemisorption**					

Incident:	**Gas leakage**	

Consequence area:	Helse		Risk before measures:	🟡	Risiko after measures:	⚪
	Ytre miljø		Risk before measures:	🟡	Risiko after measures:	⚪
	Materielle verdier		Risk before measures:	🟡	Risiko after measures:	⚪

Final evaluation

Organizational units and people involved

A risk assessment may apply to one or more organizational units, and involve several people. These are lsited below.

Organizational units which this risk assessment applies to

- Institutt for kjemisk prosessteknologi

Participants

Estelle Marie M. Vanhaecke

Karin Wiggen Dragsten

Hilde Johnsen Venvik

Readers

[Ingen registreringer]

Others involved/stakeholders

[Ingen registreringer]

The following accept criteria have been decided for the risk area Risikovurdering: Helse, miljø og sikkerhet (HMS):

Helse   **Materielle verdier**   **Omdømme**   **Ytre miljø**

Overview of existing relevant measures which have been taken into account

The table below presents existing measures which have been take into account when assessing the likelihood and consequence of relevant incidents.

Hazard	Incident	Measures taken into account
Catalyst synthesis	Ni(NO3)2*6H20	Personal protective equipment
	Ni(NO3)2*6H20	Fume hood
	Ni(NO3)2*6H20	Protective gloves
	Ni(NO3)2*6H20	SDS
	Co(NO3)2*6H2O	Personal protective equipment
	Co(NO3)2*6H2O	Fume hood
	Co(NO3)2*6H2O	Protective gloves
	Co(NO3)2*6H2O	SDS
	Kaliumhydroxide	Personal protective equipment
	Kaliumhydroxide	Fume hood
	Kaliumhydroxide	SDS
	Pd(NO3)2 2*H2O	Personal protective equipment
	Pd(NO3)2 2*H2O	Fume hood
	Pd(NO3)2 2*H2O	Protective gloves
	Pd(NO3)2 2*H2O	SDS
	Ag(NO3)	Personal protective equipment
	Ag(NO3)	Fume hood
	Ag(NO3)	Protective gloves
	Ag(NO3)	SDS
	Ag(NO3)	Gas masks
	Ag(NO3)	Face shield
	Ag(NO3)	COVID-19 guidelines
	Al2O3	Personal protective equipment
	Al2O3	SDS
TPR	Gas Leakage	Personal protective equipment
	Gas Leakage	Training in procedure
	Gas Leakage	Leak detection spray
	Spill of samples	Personal protective equipment
	Spill of samples	Fume hood
	Spill of samples	Protective gloves
	Spill of samples	Training in procedure
	Spill of samples	SDS
Raman spectroscopy	Eye damage	Personal protective equipment

Detailed Risk Report

Raman spectroscopy	Eye damage	Guiding lines
	Eye damage	Training in procedure
	Chemical exposure during sample preparation	Personal protective equipment
	Chemical exposure during sample preparation	Fume hood
	Chemical exposure during sample preparation	Training in procedure
	Chemical exposure during sample preparation	SDS
X-ray Diffraction	Exposure of chemicals during sample preparation	Personal protective equipment
	Exposure of chemicals during sample preparation	Fume hood
	Exposure of chemicals during sample preparation	Protective gloves
	Exposure of chemicals during sample preparation	SDS
COVID-19	COVID-19 infection	Personal protective equipment
	COVID-19 infection	COVID-19 guidelines
X-ray fluorescence	Exposure of chemicals during sample preparation	Personal protective equipment
	Exposure of chemicals during sample preparation	Fume hood
	Exposure of chemicals during sample preparation	Protective gloves
	Exposure of chemicals during sample preparation	Training in procedure
	Exposure of chemicals during sample preparation	SDS
N2-physisorption	Liquid N2-spill	Personal protective equipment
	Liquid N2-spill	Training in procedure
	Liquid N2-spill	SDS
	Liquid N2-spill	Isolating gloves
	Liquid N2-spill	Isolating gloves
	Liquid N2-spill	Face shield
	Liquid N2-spill	Face shield
Rig	Gas leakage	Personal protective equipment
	Gas leakage	Guiding lines
	Gas leakage	Training in procedure
	Gas leakage	Gas detector
	Gas leakage	Leak detection spray
	Skin burn	Personal protective equipment
	Skin burn	Protective gloves
	Skin burn	Training in procedure
	Skin burn	Isolating gloves
TGA	Gas leakage	Personal protective equipment

Norges teknisk-naturvitenskapelige universitet (NTNU)   **Print date:**   **Printed by:**   **Page:**

Unntatt offentlighet jf. Offentlighetsloven § 14   13.06.2021   Sunniva Skogheim   10/30

Detailed Risk Report

TGA	Gas leakage	Training in procedure
	Gas leakage	Gas detector
Chemisorption	Gas leakage	Personal protective equipment
	Gas leakage	Protective gloves
	Gas leakage	Guiding lines
	Gas leakage	Training in procedure
	Gas leakage	SDS
	Gas leakage	Gas detector
	Gas leakage	COVID-19 guidelines

Existing relevant measures with descriptions:

Personal protective equipment
Lab coat
Goggles
Covering shoes

Fume hood
[Ingen registreringer]

Protective gloves
[Ingen registreringer]

Guiding lines
[Ingen registreringer]

Training in procedure
[Ingen registreringer]

SDS
Safety data sheet

Gas masks
[Ingen registreringer]

Gas detector
[Ingen registreringer]

Leak detection spray
[Ingen registreringer]

Isolating gloves
[Ingen registreringer]

Face shield
[Ingen registreringer]

COVID-19 guidelines
[Ingen registreringer]

Detailed Risk Report

Risk analysis with evaluation of likelihood and consequence

This part of the report presents detailed documentation of hazards, incidents and causes which have been evaluated. A summary of hazards and associated incidents is listed at the beginning.

The following hazards and incidents has been evaluated in this risk assessment:

- **Catalyst synthesis**
  - Ni(NO3)2*6H2O
  - Co(NO3)2*6H2O
  - Kaliumhydroxide
  - Pd(NO3)2 2*H2O
  - Ag(NO3)
  - Al2O3
- **TPR**
  - Gas Leakage
  - Spill of samples
- **Raman spectroscopy**
  - Eye damage
  - Chemical exposure during sample preparation
- **X-ray Diffraction**
  - Exposure of chemicals during sample preparation
- **COVID-19**
  - COVID-19 infection
- **X-ray fluorescence**
  - Exposure of chemicals during sample preparation
- **N2-physisorption**
  - Liquid N2-spill
- **Rig**
  - Gas leakage
  - Skin burn
- **TGA**
  - Gas leakage
- **Chemisorption**
  - Gas leakage

Detailed Risk Report

Detailed view of hazards and incidents:

Hazard: Catalyst synthesis

Incident: Ni(NO3)2*6H20

Cause: Spill of Ni(NO3)*6H2O

Likelihood of the incident (common to all consequence areas): **Less likely (2)**

Kommentar:

Provided measures will be used during the synthesis such as lab coat, gloves and safety goggles which will protect the eyes and the skin.

Consequence area: Helse   *Risk:*

Assessed consequence: **Very large (4)**

Comment: The substance can cause serious eye damage, irritates the skin and can trigger an allergic reaction.

Inhalation of Ni(NO3)2*6H2O is dangerous if inhaled and if swallowed and may cause cancer. If inhaled it can also trigger allergy or breathing issues.

Consequence area: Ytre miljø   *Risk:*

Assessed consequence: **Large (3)**

Comment: The substance is very toxic and with long-term effects on aquatic life.

Detailed Risk Report

Incident: Co(NO3)2*6H2O
- -

Cause: Spill

Cause: Inhalation

Likelihood of the incident (common to all consequence areas):   **Less likely (2)**

> *Kommentar:*
> With the provided measures such as lab coat, googles, gloves and fume hood the likelihood is sat to low.
> Lab coat, googles and gloves will protect eyes and skin from a potential spill.
> Work proceeded under a fume hood will protect against inhalation of vapour.

Consequence area: Helse   *Risk:*

    Assessed consequence: **Very large (4)**

> *Comment:* The substance is dangerous if swallowed
> Potential risk of cancer if inhaled
> Can cause an allergic reaction if in contact with skin

Consequence area: Ytre miljø   *Risk:*

    Assessed consequence: **Very large (4)**

> *Comment:* Very toxic, with long-term effect for aquatic life.

Incident: Kaliumhydroxide
- -

Likelihood of the incident (common to all consequence areas):   **Unlikely (1)**

> *Kommentar:*
> With the provided measures, the likelihood of spill is small.

Consequence area: Helse   *Risk:*

    Assessed consequence: **Very large (4)**

> *Comment:* It is dangerous if swallowed and may give serious damage on the skin and
> eyes.

Detailed Risk Report

Consequence area: Materielle verdier   *Risk:*

    Assessed consequence: **Large (3)**

        Comment: It is corrosive for metals and therefore it is a possibility for damage on the
               equipment.

Incident: Pd(NO3)2 2*H2O
- -

    Cause: Spill of chemical

Likelihood of the incident (common to all consequence areas):   **Less likely (2)**

    Kommentar:

    Provided measures will be used during the synthesis such as lab coat, gloves and safety goggles which will
    protect the eyes and the skin.

Consequence area: Helse   *Risk:*

    Assessed consequence: **Very large (4)**

        Comment:
               - Gives serious eye damage on skin and eyes
               - Can intensify fire; oxidizing

Consequence area: Materielle verdier   *Risk:*

    Assessed consequence: **Very large (4)**

        Comment:
               - Can intensify fire; oxidizing

Norges teknisk-naturvitenskapelige   **Print date:**   **Printed by:**   **Page:**
universitet (NTNU)

Unntatt offentlighet jf. Offentlighetsloven § 14   13.06.2021   Sunniva Skogheim   16/30

Detailed Risk Report

Incident: Ag(NO3)

- -

Likelihood of the incident (common to all consequence areas):   **Less likely (2)**

Kommentar:

Provided measures will be used during the synthesis such as lab coat, gloves and safety goggles which will protect the eyes and the skin.

Consequence area: Helse   *Risk:*

Assessed consequence: **Very large (4)**

Comment: - Gives serious eye damage on skin and eyes
            - Extremely poisonous, with long-term effect, for life in water

Consequence area: Ytre miljø   *Risk:*

Assessed consequence: **Very large (4)**

Comment: Extremely poisonous, with long-term effect, for life in water
            Can intensify fire; oxidizing

Consequence area: Materielle verdier   *Risk:*

Assessed consequence: **Large (3)**

Comment: May be corrosive for metals

Detailed Risk Report

Incident: Al2O3

Cause: Spill of chemical

Likelihood of the incident (common to all consequence areas): **Unlikely (1)**

Kommentar:
[Ingen registreringer]

Consequence area: Helse   *Risk:*

Assessed consequence: **Small (1)**

Comment: [Ingen registreringer]

Consequence area: Materielle verdier   *Risk:*

Assessed consequence: **Small (1)**

Comment: [Ingen registreringer]

Detailed Risk Report

Hazard: TPR

Temperature Programmed Reduction

Incident: Gas Leakage

- -

Likelihood of the incident (common to all consequence areas):   **Unlikely (1)**

    Kommentar:

    The rig will be tested for gas leakage before proceeding. If any leakage occures ventilation will make sure to dilute the gas.

Consequence area: Helse   *Risk:*

    Assessed consequence: **Very large (4)**

      Comment: Gas leakage in the rig may cause an explosion. I worst cast scenario, the explosion can be lethal.

Consequence area: Materielle verdier   *Risk:*

    Assessed consequence: **Large (3)**

      Comment: The rig or other respective equipment can be destroyed.

Incident: Spill of samples

- -

Likelihood of the incident (common to all consequence areas):   **Less likely (2)**

    Kommentar:

    Provided measures will be used. Working under a fume hood will reduce the risk of inhalation of the substances in the sample.

Consequence area: Helse   *Risk:*

    Assessed consequence: **Very large (4)**

      Comment: The substances in the sample are cancerogenic.

Norges teknisk-naturvitenskapelige universitet (NTNU)	**Print date:**	**Printed by:**	**Page:**
Unntatt offentlighet jf. Offentlighetsloven § 14	13.06.2021	Sunniva Skogheim	19/30

Detailed Risk Report

Hazard: Raman spectroscopy

Incident: Eye damage

- -

Likelihood of the incident (common to all consequence areas):   **Unlikely (1)**

Kommentar:

Can easily be avoided by using protective goggles or not looking directly in the laser beam.

Consequence area: Helse   *Risk:*

Assessed consequence: **Medium (2)**

Comment: This can easily be avoided, but can damage your eyes or cause blindness (in worst case scenario)

Incident: Chemical exposure during sample preparation

- -

Likelihood of the incident (common to all consequence areas):   **Less likely (2)**

Kommentar:

Provided measures will be used and the likelihood is therefore low. Risk of inhalation will be reduced when working in a fume hood.

Consequence area: Helse   *Risk:*

Assessed consequence: **Very large (4)**

Comment: The substances in the sample are cancerogenic.

Detailed Risk Report

Hazard: X-ray Diffraction

Incident: Exposure of chemicals during sample preparation

- -

Likelihood of the incident (common to all consequence areas):   **Unlikely (1)**

   Kommentar:
   Provided measures will be used and therefore the likelihood can be set to low.

Consequence area: Helse   *Risk:*

   Assessed consequence: **Very large (4)**

         Comment: The chemicals are cancerogenic.

Detailed Risk Report

Hazard: COVID-19

Incident: COVID-19 infection

- -

Likelihood of the incident (common to all consequence areas):   **Less likely (2)**

Kommentar:

The possibility of getting infected by COVID-19 in the laboratory is considered as low. Several measures have been put in to place to prevent this:
- At least 1 m distance from other persons working at NTNU
- Disinfecting all contact surfaces before and after activity
- Wash hands regularly
- Work planning in the lab

Consequence area: Helse   *Risk:*

Assessed consequence: **Very large (4)**

Comment: In the case of underlying diseases or old age, being infected of COVID 19 may be fatal. In worst case, lethal. For younger people with no underlying diseases the risk is considered not dangerous.

Norges teknisk-naturvitenskapelige universitet (NTNU)   **Print date:**   **Printed by:**   **Page:**

Unntatt offentlighet jf. Offentlighetsloven § 14   13.06.2021   Sunniva Skogheim   22/30

                                                                              Detailed Risk Report

---

Hazard: X-ray fluorescence

Incident: Exposure of chemicals during sample preparation

The sample is going to be distributed over a pellet consisting of boric acid.

Likelihood of the incident (common to all consequence areas):   **Less likely (2)**

        Kommentar:

        The likelihood is set to low because of the provided measures. Working under a fume hood will reduce the risk
        of inhalation of the chemicals.

Consequence area: Helse   *Risk:*

    Assessed consequence: **Very large (4)**

        Comment: The chemicals are cancerogenic.

Norges teknisk-naturvitenskapelige   **Print date:**   **Printed by:**   **Page:**
universitet (NTNU)
Unntatt offentlighet jf. Offentlighetsloven § 14   13.06.2021   Sunniva Skogheim   23/30

Detailed Risk Report

Hazard: N2-physisorption

Incident: Liquid N2-spill

- -

Likelihood of the incident (common to all consequence areas): **Unlikely (1)**

    Kommentar:

    This is very unlikely because of provided measures.

Consequence area: Helse   *Risk:*

    Assessed consequence: **Large (3)**

              Comment: Can give frostbite,

                                                    Detailed Risk Report

---

Hazard: Rig

Incident: Gas leakage
- -

Likelihood of the incident (common to all consequence areas):   **Unlikely (1)**

Kommentar:
Given the provided measures, the probability of this happening is very small. Gas detector and the leak detection spray will discover any leak. Further, the ventilation system will dilute the gas concentration if any leak is formed.

Consequence area: Helse   *Risk:*

Assessed consequence: **Catastrophical (5)**

Comment: An extremely flammable gas will be used in the rig (methane) and it can explode under the right conditions. May have lethal consequences in the worst case scenario.
CO gas is extremely poisionous and can give fetal and organ damage from prolonged or repeated exposure.

Consequence area: Ytre miljø   *Risk:*

Assessed consequence: **Catastrophical (5)**

Comment: The gases are
- extremely flammable
- can explode upon heating

Consequence area: Materielle verdier   *Risk:*

Assessed consequence: **Very large (4)**

Comment: The rig and the respective equipment can be destroyed if it occur and gas leakage in the rig.

 Detailed Risk Report

Incident: Skin burn
- -

Likelihood of the incident (common to all consequence areas):   **Unlikely (1)**

   Kommentar:
   Some of the equipment requires a high temperature, but when working with these the provided measures will
   be used and reduce the risk of getting burned from a possible hot surface.

Consequence area: Helse   *Risk:*

   Assessed consequence: **Large (3)**

      Comment: The extent of damage will be exposure- and time dependent.

Norges teknisk-naturvitenskapelige   **Print date:**   **Printed by:**   **Page:**
universitet (NTNU)

Unntatt offentlighet jf. Offentlighetsloven § 14   13.06.2021   Sunniva Skogheim   26/30

                                                Detailed Risk Report

---

Hazard: TGA

Thermogravimetric analysis

Incident: Gas leakage

- -

Likelihood of the incident (common to all consequence areas):   **Unlikely (1)**

Kommentar:

Given the provided measures: Gloves, safety googles, lab coat, gas detectors and gas alarms, the probability of this happening is very small. Gas detector and the leak detection spray will discover any leak. Further, the ventilation system will dilute the gas concentration if any leak is formed.

Consequence area: Helse   *Risk:*

Assessed consequence: **Very large (4)**

Comment: Gas leakage may cause an explosion. I worst cast scenario, the explosion can be lethal.

Consequence area: Materielle verdier   *Risk:*

Assessed consequence: **Very large (4)**

Comment: Equipment can be destroyed if an explosion occur.

Detailed Risk Report

Hazard: Chemisorption

For measuring dispersion and particle size of metals in catalytic samples. Adsorption that involves a chemical reaction between the surface and the adsorbate.

Incident: Gas leakage

CO gas will be used as adsorbate.

Likelihood of the incident (common to all consequence areas):   **Less likely (2)**

Kommentar:

Gas detectors will be used and there are also gas alarms in the room.

Consequence area: Helse   ***Risk:***

Assessed consequence: **Very large (4)**

Comment: CO gas is extremely poisonous and can give fetal and organ damage from prolonged or repeated exposure

Consequence area: Ytre miljø   ***Risk:***

Assessed consequence: **Very large (4)**

Comment: CO gas is
- Extremely flammable
- Can explode by heating

Consequence area: Materielle verdier   ***Risk:***

Assessed consequence: **Very large (4)**

Comment: CO gas can explode by heating.

Overview of risk mitiating measures which have been decided:

Below is an overview of risk mitigating measures, which are intended to contribute towards minimizing the likelihood and/or consequence of incidents:

Overview of risk mitigating measures which have been decided, with description:

Detailed Risk Report

Detailed view of assessed risk for each hazard/incident before and after mitigating measures

Sunniva Skogheim

Low-Temperature Oxidation of Methane (CH_4) and Carbon Monoxide (CO) over Pd/Al_2O_3 and Pd-Ag/Al_2O_3 Catalysts

NTNU
Norwegian University of
Science and Technology